The Impact of Swirl in Turbulent Pipe Flow

A Thesis

Presented to

The Academic Faculty

by

Akay A. Islek

In Partial Fulfillment
of the Requirements for the Degree
Master of Science in the
Woodruff School of Mechanical Engineering

Georgia Institute of Technology
2004

The Impact of Swirl in Turbulent Pipe Flow

Approved by:

Dr. Cyrus Aidun, Co-Advisor

Dr. Minami Yoda, Co-Advisor

Dr. Mostafa Ghiaassiaan

Date approved: November 2004

ACKNOWLEDGEMENTS

The work for this thesis was carried out at the School of Mechanical Engineering and the Institute of Paper Science and Technology (IPST) at the Georgia Institute of Technology. It was supported by the Department of Energy. First of all, I would like to thank my advisors, Drs. Cyrus Aidun and Minami Yoda for their enduring trust in me and for all the experience they shared with me. I would like to thank Dr. Mehran Parsheh for his contribution to this research.

I want to thank Dr. Venkata Bandhakavi for his help in designing parts of the experimental set-up and Paul McKay for his help in various parts of the research. My special thanks to Matthew Brown, my lab mate, for his great friendship and most helpful discussions.

I am grateful to Dr. Haluk Karadogan for his never lasting support to my studies. I also want to thank every student in the research groups I am a member of, both in IPST and in the School of Mechanical Engineering. Thank you Tim, Haifung, Charlotte, Sam, Ulf, Reza, Lyle and Yusuke. It was an exciting experience for me to be a part of such societies.

My very special thanks to my terrific friends, here and far, who make hard things easier and dull moments funnier: Thank you Görkem, Defne, Ergi, Cem, Chee, Faik, Göktan, Aysegül and Emre. I'm especially grateful to my grandmother, to my family and to İdil whose support is precious to me.

TABLE OF CONTENTS

LIST OF TABLES

LIST OF FIGURES

Page

Page

NOMENCLATURE

Roman

A	-	constant in Eq. I-5
a	-	constant in Eq. I-8
A_f	^{o}C	austenite finish temperature
A_s	^{o}C	austenite start temerature
B	-	constant in Eq. I-6
c	mm	plate chord length
C	-	constant in Eq. I-13
D	mm	pipe inner diameter, y-dimension of the fins
D_b	50 mm	beam spacing
d_e	mm	beam diameter at the focal waist
D_e	mm	beam diameter at the converging lens
d_{fr}	μm	fringe spacing
d_m	mm	y-dimension of the measurement volume
d_p	m	tracer particle diameter
f	350 mm	focal length
f_D	Hz	Doppler frequency
g	9.81 m^2/s	gravitational acceleration
h_m	mm	z-dimension of the measurement volume
L	m	plate length
ℓ	m	cross-stream length scale in wake flow
ℓ_1	mm	x-dimension of the straight section of a flat plate
ℓ_2	mm	x-dimension of the tapered section of a flat plate
ℓ_m	mm	x-dimension of the measurement volume
M_f	^{o}C	martensite finish temperature
M_s	^{o}C	martensite start temperature
n	-	index of refraction
N	-	number of samples

N_r	-	rotation rate
N_s	-	Stokes number, $N_s = \sqrt{\frac{\mu}{\rho \omega d_p^{\,2}}}$
R	mm	pipe inner radius, $R=D/2$
r	m	radial coordinate
Re	-	Reynolds number
R_o	14.22 mm	pipe outer radius
s	-	density ratio, $s = \frac{\rho_p}{\rho}$
S_0	-	initial swirl intensity
S_b	-	swirl number, $S_b(x) = \frac{2\pi\rho\int_0^R y^2 UV dy}{\pi\rho R^3 U_{ref}^2}$
S_f	-	swirl number, $S_f(x) = \frac{2\pi\rho\int_0^R y^2 UV dy}{2\pi\rho R\int_0^R yU^2 dy}$
t	mm	thickness
t_{N-1}	-	t value obtained from a table of t for N-1 degrees of freedom.
TI_x	-	turbulence intensity in the x-direction
T_m	m^2/s	maximum moment of the azimuthal velocity
U	m/s	axial mean velocity
u_τ	m/s	friction velocity
$\tilde{u}_i$	m/s	instantaneous velocity
u'	m/s	root-mean-squared velocity fluctuation in the x direction
u	m/s	velocity fluctuation in the x direction
U_e	m/s	average freestream velocity
U_{min}	m/s	minimum mean velocity
U_{ref}	m/s	reference velocity

U_s	m/s	maximum velocity defect, $U_s = U_e - U_{min}$
V	m/s	azimuthal mean velocity
v'	m/s	root-mean-squared velocity fluctuation in the y direction
v	m/s	velocity fluctuation in the y direction
V_D	mm^3	measurement volume
W	m/s	radial mean velocity
w'	m/s	root-mean-squared velocity fluctuation in the z direction
w	m/s	velocity fluctuation in the z direction
wc	m	contraction width
w_{le}	mm	trailing edge thickness
w_{te}	mm	leading edge thickness
x	mm	downstream distance from the Vortigen tube
x^+	-	$x^+ \equiv xu_\tau / \nu$
y	mm	distance from the pipe center normal to the fin leading edge
Y	mm	displacement of the laser beams in y-direction (in water)
Y'	mm	displacement of the laser beams in y-direction (in air)
Y''	mm	actual displacement of the laser beams in y-direction (in index matching fluid)
z	mm	distance from the pipe center along the fin leading edge

Greek

α	3.45^{o}	taper angle
β	-	decay rate of swirl intensity
δ	m	boundary layer thickness
θ	-	incident angle
κ	-	beam half angle
λ	nm	wavelength
μ	kg/m s	dynamic viscosity
ν_T	m^2/s	eddy viscosity

v	m^2/s	kinematic viscosity
ξ	-	$\xi = y / \ell$
ρ	kg/m^3	fluid density
ρ_p	kg/m^3	tracer particle density
σ	-	standard deviation
σ_a	GPa	modulus of elasticity in austenite phase
σ_m	GPa	modulus of elasticity in martensite phase
τ_t	s	convective time scale
ϕ	-	streamline angle, $\phi(x, y) = \tan^{-1}\left(\frac{V}{U}\right)$
ω	Hz	angular frequency of velocity fluctuations

Subscripts

a	air
g1	glass (index matching tank)
g2	glass (pipe)
i	index
m	index matching fluid
n	index
w	water

SUMMARY

The impact of swirl (*i.e.*, flow with axial and azimuthal velocity components) on the turbulent flow in a pipe is studied using two-component laser-Doppler velocimetry (LDV). There are practical motivations for the flow geometry. For example, previous studies demonstrate that introducing swirl in the tube bank of a paper machine headbox can significantly increase mixing, and hence increase fiber dispersion and orientation isotropy in the finished paper product. The flow characteristics in a pipe downstream of a single straight tapered fin, a single fin with 180° twist but otherwise identical geometry, and four twisted fins were therefore studied at a pipe-based Reynolds number of 80,000. Radial profiles of the mean and rms fluctuations of the streamwise and azimuthal velocity components are measured; results for the straight and twisted single fin are compared to determine the effects of fin geometry and swirl on the turbulent wake downstream of the fin. From a practical viewpoint, it is also desirable to have "adjustable" swirl, where swirl can either be turned "on" or "off" depending upon the type of paper product being produced. The next generation 'swirler' concept consists of fins fabricated from two-way shape memory alloys. Using the two-way memory effect, the fins will be in their straight configuration when "cold" and twisted configuration (hence acting as a swirler) when "hot". This study is the initial phase in developing new active control mechanisms, known as the Vortigen concept, for increasing productivity, and hence reducing wasted raw material and energy, in the pulp and paper industry.

CHAPTER I

INTRODUCTION

I.1. Motivation, Objectives, Significance and Scope

This study was a part of a project the aim of which is to retrofit a current headbox for generation and on-line control of axial vorticity for uniform dispersion and distribution of fibers on the moving wire in a paper making machine to optimize turbulent scale and intensity, and consequently, fiber network structure properties in the sheet.

The study involves implementing a new technology, *Vortigen technology*, in a headbox to produce an isotropic sheet with significant reductions in the ratio of machine direction to cross machine direction stiffness and improved sheet uniformity.

Essentially, headbox of a paper making machine converts a pipe flow into a thin rectangular jet, which then impinges on a moving screen to be pressed and dried. The flow is a suspension of fibers and filers in water. A typical headbox consists of three sections: a tapered manifold, a rectangular array of tubes (*i.e.* the tube bank) connecting the manifold to the next section and the converging nozzle ending with a thin lip (*i.e.* the slice). In order to have a quality paper product, the suspension should be evenly distributed when it impinges on the moving screen (referred to as “wire”) at a certain

speed. Smook (2004) explains the importance of the headbox as: “No part of a modern high-speed paper machine has more impact on product uniformity than the headbox”.

Because of the hydrodynamic characteristics inherent in the production process, fibers tend to orient in the direction of the machine, rather than spreading and orienting uniformly. The result is a network of fibers with a preferential orientation that has been a problem for the paper industry since high-speed paper machines were introduced in 1960’s. Non-uniform fiber network structure causes paper to curl, prompts paper jams in photocopiers and laser printers. Also, paper remains weak in the cross-machine direction, which is why it's easy to tear an article from a broadsheet newspaper lengthwise, but not across the sheet. Strength is a crucial issue especially in the packaging industry, where cardboard and corrugated products must measure up to designated standards.

The difference in the speed of the moving wire and the average velocity of the jet coming out of the lip of the headbox can be used to alter the fiber orientation. An increase in this difference forces the fibers to orient in the direction of the machine. Ullmar and Norman (2004) argue that an increase in the contraction ratio of the headbox nozzle can also increase the alignment towards the machine direction. In a study by Aidun (1997) it has been shown that interaction of jets coming out of individual tubes in the headbox creates “secondary vortices” in the converging part of the headbox. These secondary flows cause non-uniformities in the finished paper product. Aidun argues that generation of swirl at certain strength in the individual tubes can eliminate these secondary flows as the mixing of the jets coming out of the tubes will be considerably enhanced.

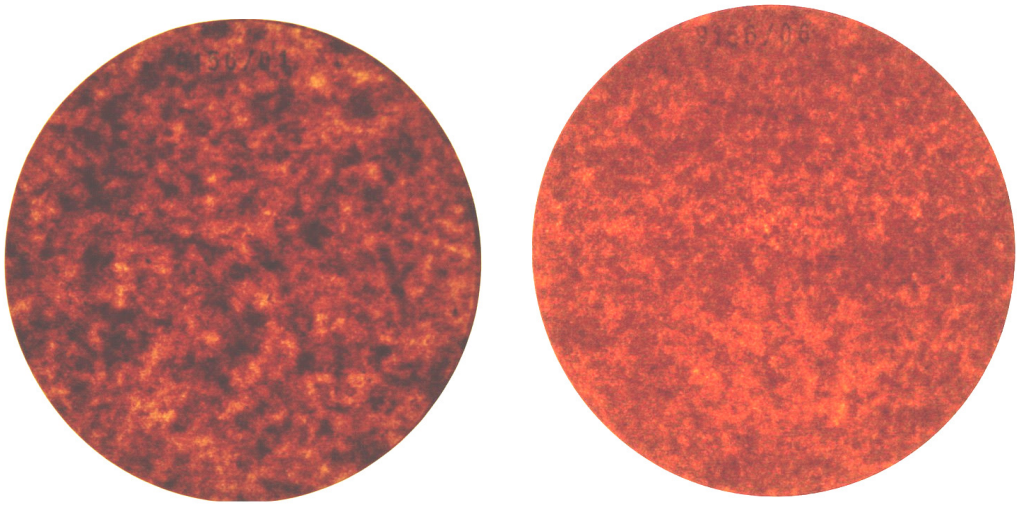

Figure I.1. Mass distribution in the finished paper product (a) without Vortigen (b) with Vortigen. Dark colors indicate higher density of fibers.

By increasing the uniformity of the fiber network structure, the Vortigen system generates two major benefits:

1. Paper products become stronger in the cross-machine direction and more uniform
2. For some products, significant savings are realized in raw materials

The mentioned savings extend not only to fiber, but water, energy and additives used in pulp and papermaking processes.

In addition to extensive pilot tests with a small-scale model of the mechanical device, the technology is also demonstrated on a commercial scale machine (Aidun 2001). Based on pilot trials, on average, this model yielded a 10 percent increase in strength and a 10 percent decrease in raw materials and energy for packaging products. Through extensive pilot and commercial trials, this technology has been demonstrated to be practical and effective in producing a sheet with isotropic fiber orientation and more uniform mass distribution, as shown in Fig. I.1.

With the average commercial machine using 250,000 tons of fiber each year, Vortigen Technology is expected to decrease fiber consumption by 25,000 tons — translating into annual savings of several million dollars per machine excluding savings in energy use and water consumption.

An enormous amount of water is used in pulp processing and the paper industry is the second largest industrial consumer of energy. Considering that there are more than 1,200 paper machines in US, the savings in energy consumption and the environmental impact would be significant. Paper industry is expected to implement the technology because it will pay for itself in a few months. This technology will result in significant improvements in the performance and capital effectiveness of the paper machine for a fraction of the cost to replace a headbox.

Designing the optimum turbulence and swirl generator for the flow in the headbox of the paper forming machine and controlling the properties of the flow in real time is the general aim of this study. The focus will be principally on understanding of swirl and turbulence characteristics of the flow downstream of the tapered fins with 0 and 180^{o} twist angles. In order to characterize the physics of swirl flow created by twisted fins and for calibration purposes, wakes of tapered plates in a pipe are investigated first. Then the effect of swirl on the velocity and turbulence profiles is studied. Lastly, the results with a prototype of a swirler with four fins are compared to the results with a twisted single fin. The final design will have fins made of shape memory alloys which can change shape

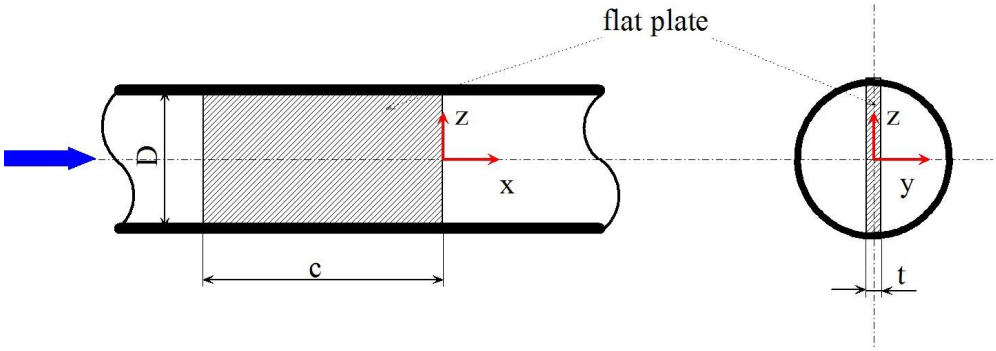

Figure I.2. Geometry of a flat plate in a pipe. The flow is in the positive *x* direction.

(*i.e.* between a swirl generating shape and a straight one) with a change in temperature supplied by a DC current passing through the fins.

The experiments are carried out at a single Reynolds number, which is taken as an input from the industrial application driving the study (*Re* = 80,000 based on the pipe diameter). It should be noted that a formal study of the boundary layers developing on the pipe walls and on the flat plates is not within the scope of this study.

I.2. Previous Work and Background

I.2.1. Wakes Behind Flat Plates

The swirler designs considered in this work are essentially twisted fins, or “tapes”. A ase flow for calibration purposes, (see Fig. I.2.) with blunt and rounded leading edge, and tapered trailing edge is studied. Direct comparison of the flow characteristics for the wakes downstream of the straight fin and the swirl generator created by twisting the same fin geometry gives insight into the effect of swirl on this confined flows.

Fig. I.2 shows the salient features of a vertical flat plate mounted inside a round pipe of inner diameter D. The plate has thickness (cross-stream dimension) t and chord (streamwise dimension) c; it is centered inside the pipe so that it completely spans the pipe diameter. A Cartesian coordinate system is used in this work, with the pipe axis along the x-axis in the axial direction and the plate cross-section aligned with the y-axis. The origin of the coordinate system is at the center of the plate trailing edge. The mean velocity components (U, V, W) and root-mean-squared velocity fluctuations (u', v', w') are along the (x, y, z) directions, respectively. The pipe walls impose the no-slip condition, *i.e.* $U = 0$, $V = 0$, $W = 0$ at a location (x, y, z), where $y^2 + z^2 = R^2$ and $R = D / 2$.

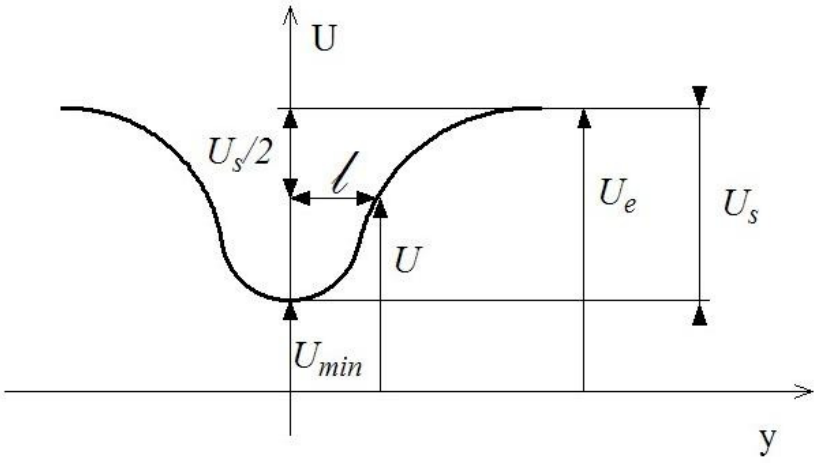

Figure I.3. Mean velocity profile of a plane wake.

A plane wake is formed when a uniform stream flows over a 2D body, which creates a "velocity defect" in the uniform flow. Fig. I.3. shows a typical velocity profile at a given downstream (x) location of the mean streamwise velocity component $U(y)$ for a fully-developed self-similar wake. There are two velocity scales in the wake flow:

average freestream velocity, U_e and the maximum velocity defect U_s, where $U_s << U_e$. Maximum velocity defect is defined as,

$$U_s \equiv U_e - U_{min} \tag{I-1}$$

Here U_{min} is the minimum mean velocity at that given x. The cross-stream length scale in wake flow, ℓ, is defined as the y distance from the centerline where the velocity defect is half the maximum velocity defect:

$$U(\ell) = U_e - \frac{1}{2}U_s \tag{I-2}$$

As x increases, the wake will spread in the streamwise and cross-stream directions due to entrainment and viscous dissipation, and ℓ and U_s will increase and decrease, respectively.

The self-similarity hypothesis, where the spatial evolution of the flow is controlled only by the local scales of length and velocity, has two assumptions: (Tennekes and Lumley 1972)

1. The velocity defect normalized by its maximum is a function only of $\xi \equiv y/\ell$:

$$\frac{U_e - U}{U_s} = f(\xi) \tag{I-3}$$

2. The Reynolds stress is proportional to the square of the velocity defect, because the turbulence intensity is of order U_s, and it is also a function of ξ:

$$-<uv> = U_s^2 g(\xi) \tag{I-4}$$

where the brackets denote ensemble averaging.

Assuming self-similarity, dimensional analysis can be used to show that the maximum velocity defect and wake half length for a two-dimensional wake must scale with x as follows (see Tennekes and Lumley 1972):

$$U_s = Ax^{-1/2} \tag{I-5}$$

$$\ell = Bx^{1/2} \tag{I-6}$$

where A and B are constants.

If the eddy viscosity hypothesis is used to express the Reynolds stress as:

$$-\langle uv \rangle = \nu_T \frac{\partial U}{\partial y} \tag{I-7}$$

where ν_T is the eddy viscosity, it can be shown that:

$$f(\xi) = \exp\left(-\frac{1}{2}\alpha\xi^2\right) \tag{I-8}$$

where α is a constant (Townsend, 1956; Tennekes and Lumley, 1974; Pope, 2000). Pope (2000) notes that self-similarity in the mean velocity profiles is experimentally observed for $U_s / U_c < 0.1$. Gumievskii (1994) points out that the axial distance at which the velocity profiles becomes self-similar depends on the shape of the body.

Wakes are of course one of the important subgroups of turbulent shear flows, and are usually classified into two groups: 1) attached wakes downstream of streamlined

shapes (the canonical example of which is a flat plate) and 2) separated wakes behind bluff bodies (e.g. cylinders) (Willimason, 1996). The literature on this subject is extensive, but the author is unaware of any other studies on the wake of a flat plate in a pipe. This section reviews previous work on (untwisted) flat-plate wakes. Reviews of Williamson (1996) and Oertel (1990) give more insight into previous studies on wakes.

The literature on flat-plate wakes is quite diverse, covering subjects such as the spatiotemporal evolution of wake turbulence, self similarity, laminar-turbulent transition, shear layer and boundary layer interactions, free-surface interactions, vortex shedding and effects of upstream or initial conditions such as plate geometry and freestream turbulence. Table I.1. reviews some experimental studies of flat-plate wakes, including brief descriptions of the plate geometry (thickness), the flow facility, the diagnostic method(s), and the focus of the study. These studies are further discussed in the remainder of this section. Numerical and analytical studies on flat plate wakes will be briefly reviewed at the end of the section.

Ramaprian and Patel (1982) studied the characteristics of the flow behind a flat plate with an elliptical leading edge and a tapered trailing edge. The experimental method was hot wire anemometry. This study was mainly focused on the asymptotic state (far-wake) of the flow which is determined by the universal distribution (*i.e.* independent of trailing edge conditions) of the mean and turbulent flow properties. They found that the asymptotic state (or "self-similarity) is reached for $x/\theta \geq 350$, where x is the axial distance from the trailing edge and θ is the momentum thickness. They define a region called the "developing wake" between the asymptotic region and the trailing edge.

Table I.1. Representative experimental studies on flat plate wakes.

Investigator	*Geometry*	*Flow*	*Method*	*Focus*
Chevray and Kovasznay (1969)	Flat plate Tapered TE (1.6 mm)	Low speed wind tunnel; Re_δ = 15,000 (δ = boundary layer thickness)	Constant-temperature hot-wire anemometry	Turbulence measurements
Andrepoulos and Bradshaw (1980)	Tapered plate, streamlined LE (28 mm)	Low speed wind tunnel; Re_θ = 13,600 (θ = momentum thickness)	Constant-temperature hot-wire anemometry	Shear layer interaction
Balachandar and Tachie (2001)	Flat plate (2 mm)	Shallow channel; Re_θ = 910 – 2040	Single-component. LDV	B.L. – wake interaction, self similarity
Haji-Haidari and Smith (1988)	Flat plate, tapered TE (100 mm)	Water channel; Re_L = 850,000 (L = plate length)	Hydrogen bubble, hot-film anemometry	Wake development, B.L., turbulent structures
Pal (1985)	Flat plate at 0°, 3° and 6° angles of attack (2.3 mm)	Subsonic wind tunnel; Re_L = 203,000 – 245,000	Hot-wire cross anemometry	Freestream turbulence effects
Sato and Kuriki (1961)	Flat plate (0.3–3 mm)	Wind tunnel; Re_L = 60,000–400,000	Hot-wire anemometry	Transition to turbulence
Swean and Keramidas (1984)	Flat plate, tapered TE (6 mm)	Shallow towing channel; Re_L = 581000	Constant-temperature hot-wire anemometry cross-fiber-film probe	Free-surface effects
Parsheh (2001)	Flat plate, tapered and blunt TE (3 -5.5 mm)	2D contraction; Re_{wc} = 50,000 – 100,000 (wc=width of the contraction)	Constant-temperature hot-wire anemometry	Self-similarity, plate geometry, shear layer interaction
Ramaprian and Patel (1982)	Flat plate, tapered TE, elliptical LE	Wind tunnel, Re_θ = 5220	Hot-wire anemometry	Wake development, B.L., self-similarity

This region is divided into two regions with distinct properties: the "near wake" and the "intermediate wake". In the intermediate wake ($25 < x/\theta < 350$), the development of the wake is similar to free turbulent flow while in the near wake, the effects of the trailing edge and the boundary layers on the plate are prominent.

In one of the most extensive studies on flat-plate wakes, Haji-Haidari and Smith (1988), who studied the wake of a tapered flat plate in a water tunnel, found that the growth of the mean centerline velocity is initially linear for $x^+ \equiv xu_\tau / \nu < 100$ (u_τ is the friction velocity, *i.e.* the square root of the ratio of the wall shear stress to the density of the fluid), but then eventually becomes logarithmic for $x^+ > 270$.

Sato and Kuriki (1961), who studied laminar to turbulent transition in the wake of a flat plate, divided the transition region into three subregions, namely the linear, nonlinear and three-dimensional regions. A sinusoidal pattern of velocity fluctuations that grow exponentially with x was observed in both the linear and non-linear regions. In a comparison of two geometrically similar plates with trailing edge thicknesses of 0.1 mm and 3 mm, they found that the thicker plate has a thicker wake and hence lower fluctuation frequencies. Mattingly and Criminale (1970) studied the stability of the "very near wake" region of a 2D body theoretically using a linearized stability theory. They indicated that, their study is complementary to the study of Sato and Kuriki where the focus was on the far downstream characteristics of the flow. Sato and Kuriki argued that the development of the vortex street is due to the transverse displacements of a single row of vortices are originally in the wake centre-plane. In contrast to this, Mattingly and Criminale suggested that the origins of the vortex street are in the near wake region.

In another experimental study, Chevray and Kovasznay (1969) studied the turbulence characteristics of a thin flat plate in a water channel and observed the evolution and merger of the turbulent boundary layers on the upper and lower surfaces of the flat plate. They point out that the y-locations where the rms fluctuations of the streamwise and azimuthal velocities (u' and v′ respectively) attain their maximum values, move away from the axis of symmetry (*i.e.* $y = 0$) as the wake develops downstream. They also showed that $u' \approx 2v'$ just downstream of the trailing edge, but $u' \rightarrow v'$ farther downstream.

Andrepoulos and Bradshaw (1980) studied the wake of a flat plate with a streamlined leading edge and a tapered trailing edge in a wind tunnel using a "temperature-conditioned sampling technique" where one of the boundary layers on the plate was heated and boundary-layer interactions are then characterized by measuring temperatures in the wake. Their results demonstrate that there is significant fine-scale mixing (indicated by "warm" regions between cold and hot regions) between the plate boundary layers.

Unlike the previous studies, which all studied flat-plate wakes in a uniform free stream, Parsheh (2001) studied wakes of flat plates mounted along the centerline of a two-dimensional contraction (modeling the converging part of a hydraulic headbox in a paper machine). Temperature was again used as a passive scalar to study the mixing of the plate boundary layers. Parsheh observed that greater azimuthal turbulence intensities enhance mixing, and that mixing depends on the plate length, with longer plates giving a more rapid decay in the maximum velocity defect. Freestream turbulence had a negligible

effect on wake development, but did affect the development of the boundary layer. Finally, profiles of the cross-stream or transverse mean velocity component were self-similar at axial locations, $x > 3$ mm where x is measured from the trailing edge. Self-similarity of the mean velocity profiles were observed for different plate lengths, leading edge thicknesses and shapes (tapered or straight).

Pal (1985) also observed self-similarity of mean cross-stream velocity component profiles, and reported that the wake centerline velocity recovered more rapidly with higher levels of freestream turbulence. More freestream turbulence also led to smaller U_s and larger ℓ.

Swean and Keramidas (1984) studied how a free-surface affected the wake of a vertical tapered plate submerged fully in a towing channel. Along with experiments, they also modeled the same flow numerically with a finite difference procedure using the k-ε model for the turbulence and concluded that the free surface causes a bigger velocity defect and larger values of both turbulent kinetic energy and Reynolds shear stress. The distance between the free surface and the plate centerline was 5 cm and 25 cm for two different cases.

Balachandar and Tachie (2001) studied the wake of a plate with a blunt trailing edge placed vertically and fully submerged in a water channel, and reported that the axial mean velocity profiles for $5 < x/t < 200$ are self-similar, where t is the plate thickness. A complete recovery of the boundary layer on the bottom of the channel (downstream of the fin) is not observed for $5 < x/t < 200$ due to distortions caused by the wake. The

streamwise turbulence intensity first increases for a short distance, then slowly decreases, with increasing x.

Alber (1979) studied the near wake region of the turbulent wake of a flat plate. Inner/Outer layer coordinate expansion technique was used. He showed that in the outer layer, which extended downstream about 10 boundary layer thicknesses, centerline velocity increases logarithmically as the flow develops downstream. The range of this region is defined as: $10^2 < xu_\tau/\nu < 10^4$.

Lasheras and Meiburg (1990) studied the three dimensional vorticity modes in the wake of a flat plate experimentally (flow visualization with induced particles) and numerically at moderate Reynolds numbers. They showed that, span-wise perturbations caused 3D vorticity modes in the wake of a plate.

I.2.2. Swirl Flow

Swirling flow in a pipe can be defined as a combination of vortex and axial motions (Baker and Sayre, 1974), with helical streamlines. To generate swirl, flow should be passed through two consecutive out-of-plane bends (Parchen and Steenbergen, 1998). Swirl flow, which contains a nonzero tangential (or azimuthal) velocity component, is always accompanied by an increase in velocity fluctuations. This section describes the characteristics of swirl flow and outlines the past work in this area.

Swirl generators (or swirlers) can be divided into five types, as depicted in Fig. I.4. Beyond the specific application considered in this thesis, swirlers are used in gas turbine engines, furnaces, burners and cyclones. Swirlers are used mainly in pipes to either enhance convective heat transfer between the fluid and the pipe walls or to increase

mixing. Main drawback of attaching swirl generators into heat exchangers and similar devices is the pressure drop accompanying the increase in the heat transfer. Therefore, there is a trade-off in terms of the energy economy. Gupte and Date (1989) reports that 10 to 20 fold increase in heat transfer can be achieved with twisted tape swirl generators accompanying an increase in the friction factor on the order of 2 to 2.5 fold. Young and Rao (1978) argue that swirl flow could be used to reduce the intensity of jet noise emerging from the engine of an aircraft. Swirling flows are also used to test turbulence models and CFD codes since capturing their characteristics is very challenging as explained in the next section.

Pitch to diameter ratio (or dimensionless pitch) is an important parameter defining the character of the twisted tape swirl generators. Pitch is defined as the axial length of the tape when it twists 360 degrees.

Although there is no standard for quantifying the strength of the swirl inside a pipe, the swirl number, defined as the ratio of the azimuthal momentum flux to the axial momentum flux, given by

$$S_f(x) = \frac{2\pi\rho\int_0^R y^2 UV dy}{2\pi\rho R\int_0^R yU^2 dy}, \qquad \text{(I-9)}$$

is commonly used (Rocklage-Marliani *et al.,* 2003). Here ρ is the fluid density. A slight modification of this formulation uses a reference velocity U_{ref} (*i.e.*, the average of the

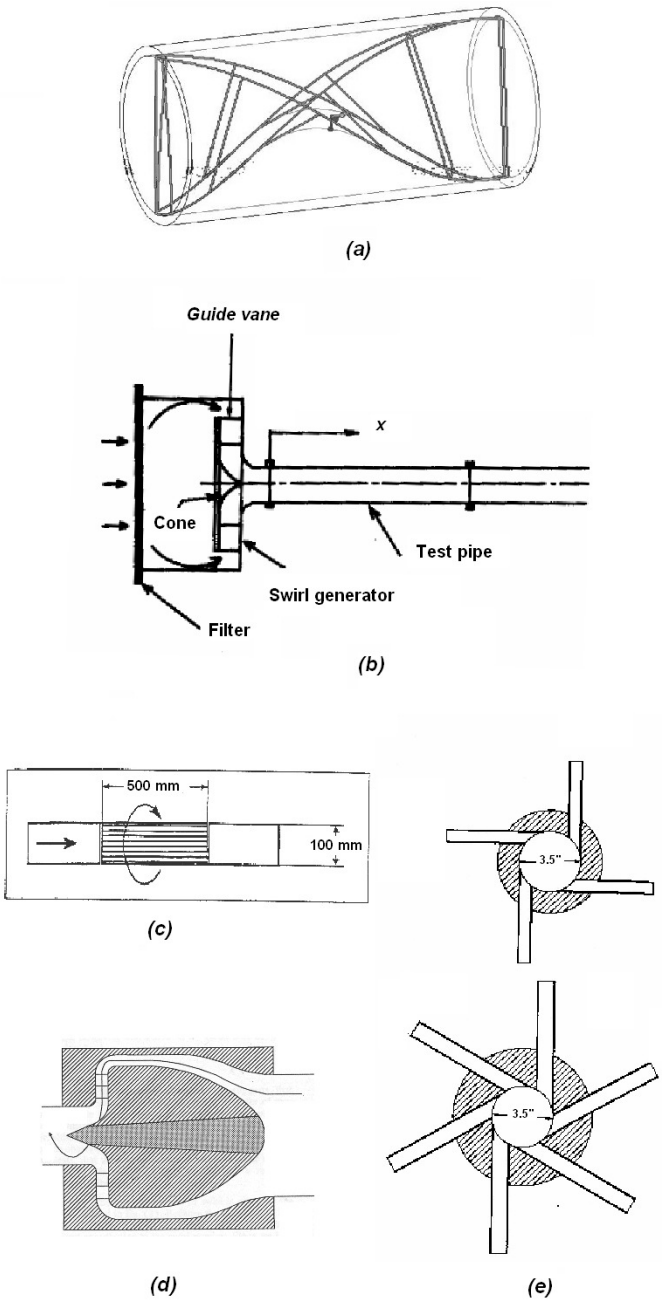

Figure I.4. Examples of swirl generators: (a) Twisted tape, current study (b) Fixed vanes, Kitoh (1991); (c) Rotating pipe, Kocherscheidt *et al.* (2002); (d) Propeller type, Parchen and Steenbergen (1998); (e) Tangential injection, Chang and Dhir (1994)

axial mean velocity over the radial span of the pipe) instead of the axial momentum flux (Rocklage-Marliani et al. 2003; Parchen and Steenbergen 1998) to define the swirl number by

$$S_b(x) = \frac{2\pi\rho\int_0^R y^2 UV dy}{\pi\rho R^3 U_{ref}^2} \tag{I-10}$$

The swirl number as defined in I-10 and 11 vary with axial location. Another definition of swirl intensity is based on the streamline angle (Park 2001):

$$\phi(x, y) = \tan^{-1}\left(\frac{V}{U}\right) \tag{I-11}$$

It has been shown by several researchers (for example, Parchen and Steenbergen, 1998) that swirl intensity, defined by Eq. I-9, decays exponentially, given by

$$S(x) = S_0 e^{-\beta x / D} \tag{I-12}$$

where β is the decay rate and S_0 is the initial swirl intensity. Parchen and Steenbergen (1998) report $\beta \approx 0.02 - 0.03$. Kreith and Sonju (1965) indicate that β varied with Reynolds number but is independent of the pitch, or swirl intensity, in their experiments with twisted-tape swirlers. Baker and Sayre (1974) argue that decay rate always increases as Reynolds number decreases.

Table I.2 summarizes previous experimental studies on the decaying swirl flow in a pipe, classified according to the type of swirler (twisted tape, tangential injection, propeller, fixed vanes and rotating tube bundle). Fig. I.5. shows a typical example of a radial profile for the mean azimuthal velocity component. This profile can be used to classify the cross-section of the pipe into three distinct flow regimes:

Table I.2. Representative experimental studies on swirl flow.

Swirler type	*Investigator*	*Method*	*Re*
Twisted tape	Kreith and Sonju (1965)	Pitch = 9 and 15, Swirl vortex meter	10,000 – 100,000
	Backshall and Landis (1969)	Pitch/Dia. = 6.16, Hot wire, micromanometer	30,000 – 110, 000
	Young and Rao (1978)	Hot wire anemometry	*not reported*
Tangential injection	King, Rothfus and Kermode (1969)	Pressure probes	10,000 – 25,000
	Chang and Dhir (1994)	Constant temperature anemometers, hot wire	12,500
	Young and Rao (1978)	Hot wire anemometry	*not reported*
Propeller	Parchen and Steenbergen (1998)	LDV	50,000
	Algifri, Bhardwaj and Rao (1988)	Hot wire anemometry	43,000 – 170,000
Fixed vanes	Baker and Sayre (1974)	Pitot static probe, swirl meter,	12,500 - 200,000
	Kitoh (1991)	Hot wire anemometry	40,000 – 80,000
	Young and Rao (1978)	Hot wire anemometry	*not reported*
	Nejad et al. (1989)	LDV	125,000
Rotating tube bundle	Rocklage-Marliani, Schmidts and Ram (2003)	LDV	280,000
	Weske and Sturov (1974)	Hot wire anemometry	30,000
	Imao, Itoh and Harada (1996)	LDV	20,000
	Kocherscheidt, Schmidts and Ram (2002)	LDV	218,000
	Young and Rao (1978)	Hot wire anemometry	*not reported*

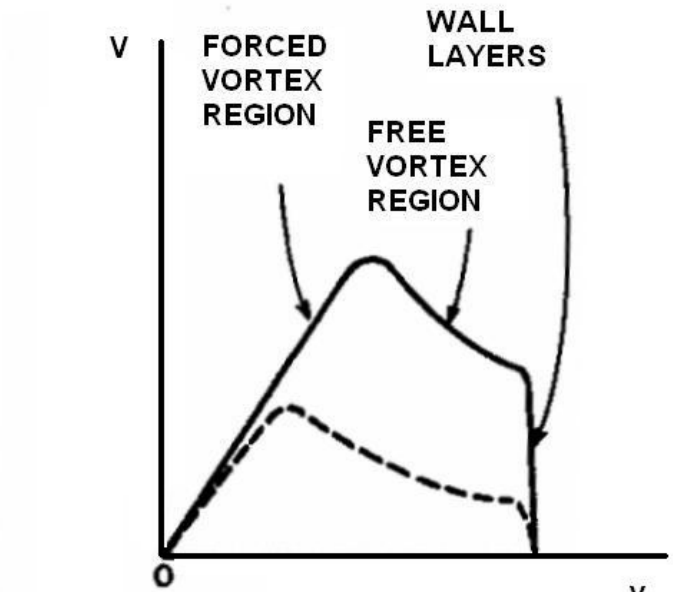

1) Near the center in the "core region," the flow is in rigid-body rotation, corresponding to a forced vortex.
2) Near the wall in the "wall layers," there are very high velocity gradients.
3) Between the core region and the wall layers in the "annular region," the flow is essentially a free vortex, with $Ur \approx$ constant .

Kitoh (1991) reports that the the annular and core regions are difficult to distinguish at low swirl numbers $S_f < 0.2$. Indeed, Imao *et al.* (1996) found that the azimuthal velocity profiles in the core region are concave, instead of the linear profile typical of a forced vortex. They suggested that this behavior is due to the early effect of the wall boundary layer. In the same study, periodic large scale fluctuations are observed at certain locations in tangential velocity profiles in a swirl flow induced by a rotating tube bundle. The range

of the "rotation rate", N_r, defined as the ratio of the tangential speed of the rotating pipe and the mean axial velocity was $0 \leq N_r \leq 1$. Kitoh (1991) also reports that

the upstream conditions such as swirler type have a much greater impact upon the core region than on the annular region.

Azimuthal velocity profiles behind a propeller-type swirler are approximated as a Rankine vortex in a study by Algifri et al. (1988):

$$V = \frac{T_m}{(r/R)}(1 - e^{-C(r/R)^2}) \tag{I-13}$$

Here, T_m is the maximum moment of the azimuthal velocity, *i.e.* $T_m = (V \times r)_{max}$, at a given downstream position and C is a constant. The experimental results showing that the radial location of the maximum azimuthal velocity moves towards the pipe centerline as x increases, are in good agreement with predictions of the Rankine vortex-based model. Algifri et al. (1988) observed that the axial velocity and turbulence intensities scaled by the maximum and mean axial velocities, respectively, are both *Re*-independent but do depend upon swirl intensity. They therefore suggested that swirling flows are "self-modeling" with respect to Reynolds number. The radial velocity component, *W,* was typically an order of magnitude less than the axial and azimuthal velocity components.

Parchen and Steenbergen (1998) reported the development of axial asymmetry in the mean streamwise and tangential velocity profiles for $x/D > 50$. Baker and Sayre (1974) reported that radial profiles of axial and tangential mean velocity components in swirl flow are not perfectly axisymmetric for all the axial locations in the experiments ($9 \leq x/D \leq 44$).

Centrifugal forces can create reverse flow (corresponding to negative values of the axial velocity) just downstream of a swirler. Parchen and Steenbergen (1988) reported flow reversal near the centerline just downstream of the swirler, and Kitoh (1991) also described flow reversal for strong swirling flows with $S_f > 0.4$. Kitoh found that both the magnitude of the negative axial velocity and the axial extent of the flow reversal increased with swirl intensity. King *et al.* (1969) focused on the flow reversal phenomenon in their study with a tangential injection swirler. They theorized that, in their pipe flow, the strong swirl near the end of the tube leads to a large pressure gradient. Consequently wall static pressure becomes greater than the centerline static pressure. Farther downstream there is not much pressure difference between the centerline and the wall. Thus, axial pressure gradient at the centerline could be positive while it is negative at the wall. They concluded that, the positive pressure gradient at the centerline might eventually force the flow to reverse. They also attempted an order of magnitude analysis to simplify the Navier-Stokes equations for swirl flow in the same study. Nejad *et al.* (1989) in a study with LDV also reported flow reversal. Two different swirlers were used in this study, having swirl numbers, S_f, of 0.3 and 0.5. Flow reversal was observed for the case with the stronger swirl. Also, they indicated a rapid decay of the axial turbulence intensities, especially for $S_f = 0.5$.

Parchen and Steenbergen (1998) and Algifri *et al.* (1988), among others, report that Reynolds normal stresses reach their maximum values near the pipe centerline, and that $<v^2>$ and $<w^2>$ are significantly higher than $<u^2>$. Kitoh (1991) indicates that turbulence intensities gradually decrease and increase in the annular and core regions, respectively.

In a study by Backshall and Landis (1969), boundary-layer velocity measurements were carried out downstream of a twisted tape swirl generator. This study concluded that the universal logarithmic velocity profile is valid in the swirl flow studied.

Swirl flow has also been investigated numerically. Parchen and Steenbergen (1998) used k-ε and modified k-ε models (Algebraic Stress Model and Reynolds Stress Model) for turbulence modeling in predicting the swirling flow. Based on the predictions on the decay of swirl and comparisons to experimental data, they concluded that the standard k-ε model, although insensitive to initial velocity distribution, is predicting the decay more accurately compared to the modified versions. In contrast to this finding, Kobayashi and Yoda (1987) argued that neither k-ε model or its modifications with higher order terms in the Reynolds stress equation are capable of predicting the axial and tangential velocity profiles in swirl flow. They proposed a modified k-ε model with the "anisotropic representation of turbulence", which was much more successful in their simulations in predicting the velocity profiles. Nejad *et al.* (1989) also found that k-ε model is not successful in solving the velocity field in swirling flows.

Swirl flow has been investigated analytically as well. Representative studies include, Wang and Nishi (1997), Kreith and Sonju (1965) and Padmanabhan (1984). In the study of Padmanabhan (1984), inspired by the flow of blood as it enters the aorta, where the flow was assumed to be Newtonian, first the flow field was divided into two regions, a core and a boundary layer, and then equations of motion were solved separately to be matched at the edge of the boundary layer. Finally, they used these results to predict the shear stress distribution in the aorta. In another theoretical work, Wang and Nishi (1997) used a quasi-three dimensional model where velocity is

expressed by superimposing an axisymmetric base flow and helical vortex filaments. Their motivation was the flow in the draft tube of a Francis turbine. Kreith and Sonju (1965), presented an analytical work (experimental part of the same study was discussed before) on the decaying swirl behind a twisted tape in a pipe based on a linearized theory. Their analyses and experimental results agreed well for 10,000 < *Re* <100,000.

Stability analyses of swirl flows were carried out in various studies. For example, Loiseleux *et al.* (1997) studied the impact of swirl on jets and wakes using linear stability analysis. Basically they examined the inviscid sapatiotemporal instability of the Rankine vortex. The axial flow was modeled as a unifiorm flow; in the region of solid body rotation the uniform flow was *assumed to be shifted by* ΔU ("plug flow"). In another study in stability, Rusak et al. (1998) carried out a numerical study on the vortex instability and breakdown ("a significant and abrupt change in the vortex structure") in high Reynold number swirl flows.

CHAPTER II

EXPERIMENTAL DESCRIPTION

Given the difficulties in simulating swirl flows due to their inherently three-dimensional nature and computational difficulties in resolving the curvature of streamlines in such flows (Kitoh, 1991), an experimental approach is required to study these flows. In this study, instantaneous local fluid velocities were measured with a two-component laser-Doppler velocimeter. Laser-Doppler velocimetry (LDV) has a number of advantages over more conventional experimental methods such as hot-wire anemometry (HWA). One of the key advantages of LDV is that it is nonintrusive (except for the addition of flow tracers). Moreover, it does not require calibration since it measures absolute velocity. LDV has therefore been used over the last forty years to obtain temporally and spatially resolved velocity data in a wide variety of both liquid and gaseous flows (*e.g.*, Absil *et al.* 1990).

LDV has been used in a number of swirl flow studies (*cf.* Table I.2.), including those by Parchen and Steenbergen (1998), Nejad et al. (1989), Itoh and Harada (1996) and Rocklage-Marliani *et al.* (2003). As noted by Rocklage-Marliani *et al.* (2003), another difficulty in modeling swirl flows is that the "fluctuation motion in the presence of swirl is often strongly anisotropic, a feature that has made this class of flows not

amenable to turbulence models based on a 'scalar eddy-viscosity' concept". This study also notes that swirl flows are highly sensitive to the presence of small obstacles in the flow, suggesting that the validity of measurements obtained using intrusive techniques such as HWA is questionable. Nevertheless, the authors point out that the curved walls and the resultant refraction at the pipe wall introduce optical issues that can significantly complicate the use of LDV in studying swirling pipe flows.

II.1. Experimental Setup

II.1.1. Flow Loop

Experiments were carried out in a re-circulating flow loop using water as the working fluid. The flow loop is sketched in Figs. II.1 and II.2; a photograph of the test section is shown is Fig. II.3. and the main components of the flow loop are listed in Table II.1. The test section was made of inner diameter $D = 25.4 \pm 0.0127$ mm optical glass (manufactured by *PEG Precision Electronic Glass Inc.* from Pyrex) with a wall thickness of 1.524 ± 0.03175 mm to allow optical access. The rest of the piping in the flow loop was Schedule 80 PVC. The flowrate was monitored during the experiments by a mass flowmeter, *Micro Motion DT7*, for most of the experiments; for the last set of experiments, a different flowmeter (*Krohne IFC 080*) was used. Water was driven through the loop by a 0.37 kW magnetic drive centrifugal pump with a frequency-controlled motor that maintained the flowrate at a constant 181.8 L/min with an uncertainty of ±1%. To maintain the flowrate, the motor was operated at a frequency of 34.5 ± 0.5 Hz. During the course of the experiments, a parallel line (25.4 mm ID

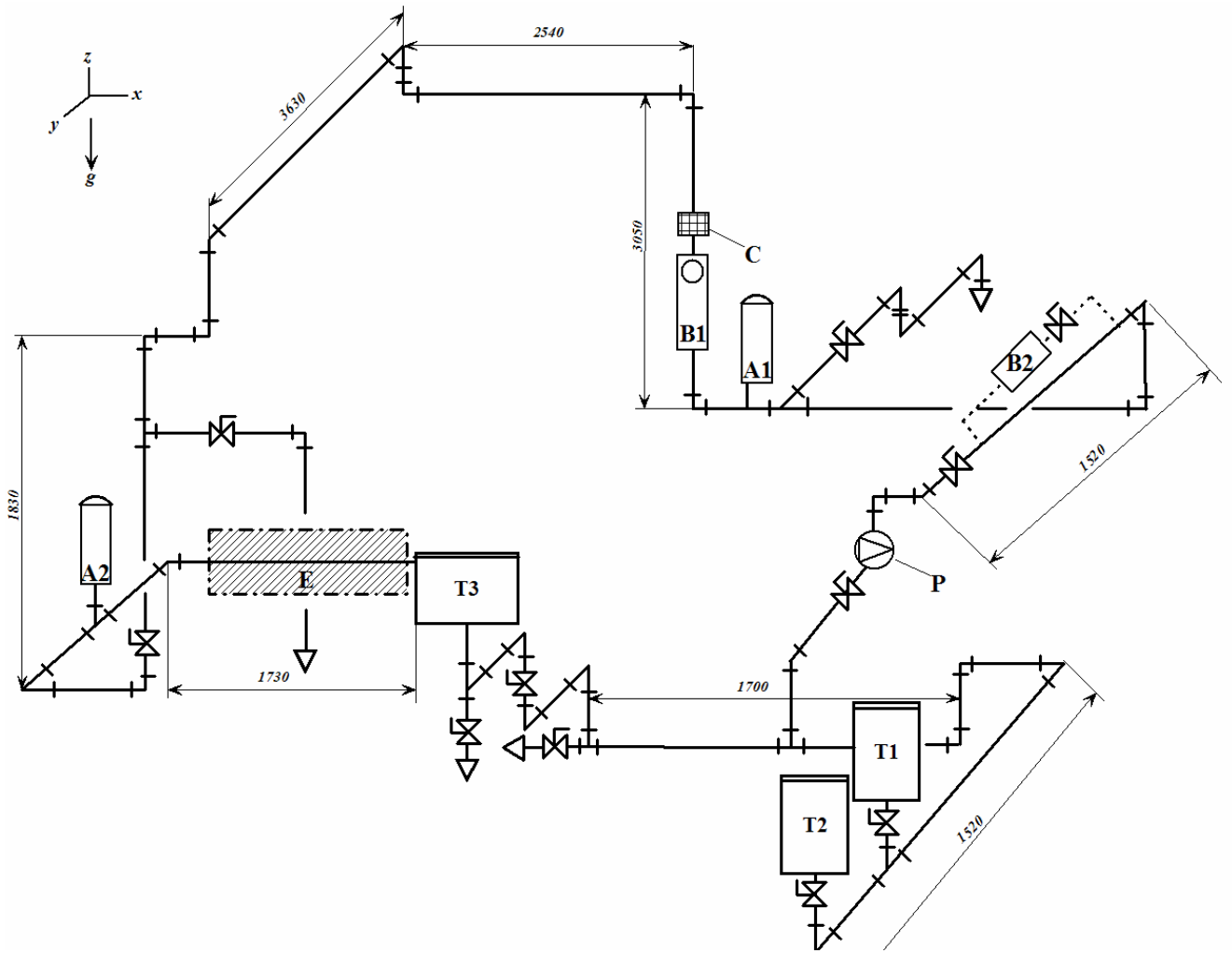

Figure II.1. Schematic of the flow loop (Dimensions in mm, not to scale). "△" indicates discharge. Dashed line shows the modification to the flow loop to install the flowmeter B2. *"g"* is the gravity.

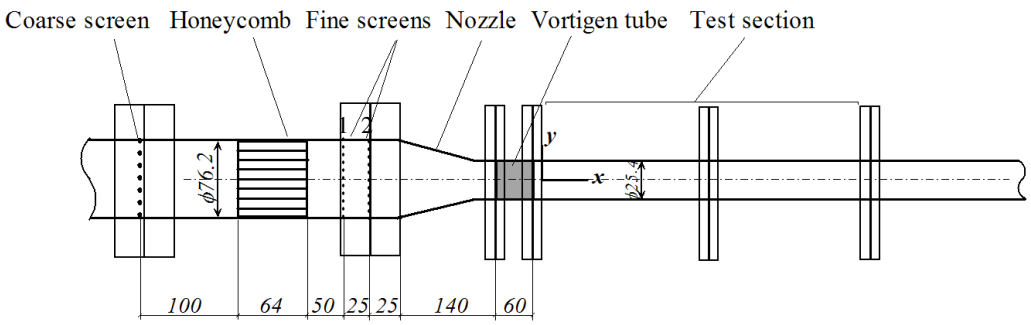

Figure II.2. Schematic of the calming section and the test section (Dimensions in mm, not to scale). Flow is in the positive *x* direction.

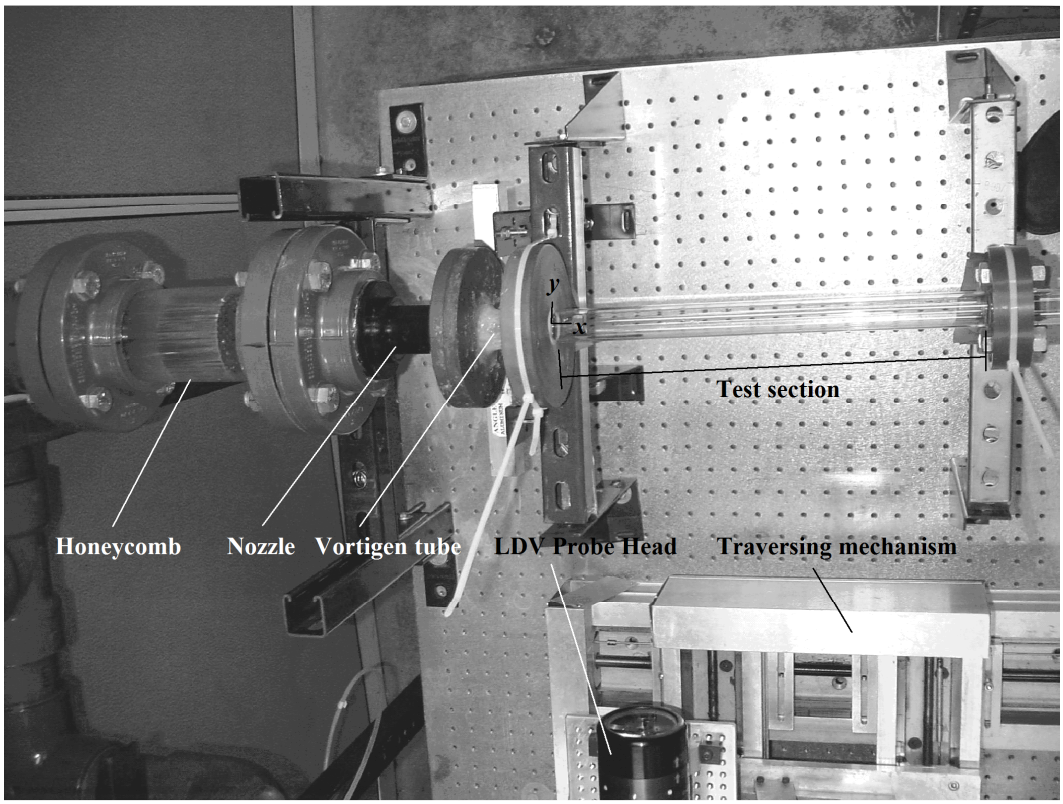

Figure II.3. Photograph of the calming section and the test section. Flow is in the positive *x* direction.

Table II.1. List of the main components in the closed flow loop shown in Fig. II.1.

Label	*Description*	*Manufacturer and Model*	*Properties*
A1	Surge tank	-	Capacity: 14.2 L
A2	Surge tank	-	Capacity: 9.7 L
B1	Flowmeter	Micro Motion DT7	-
B2	Flowmeter	Krohne IFC 080	Range: 0-25 GPM
C	Filter	-	Cell size: ~0.25 × 0.25 mm
E	Test section	-	*See Figs. II.2 and II.3.*
P	Recirculation Pump	ARO MAG Magnetic Drive	0.37 kW, 60 Hz, Head: 85 m, Capacity: 120 L/min
	Pump Motor	Ingersoll Rand	½ HP, 60 Hz, 3450 RPM
	Controller	Fuji Electric AF-300 C11 Model: 6KC1123F50X1	-
T1 and T2	Supply tanks	-	Capacity: 467 L each
T3	Supply tank	Nalge Nunc Rect. Tank XLPE 12300-0020	Capacity: 333 L

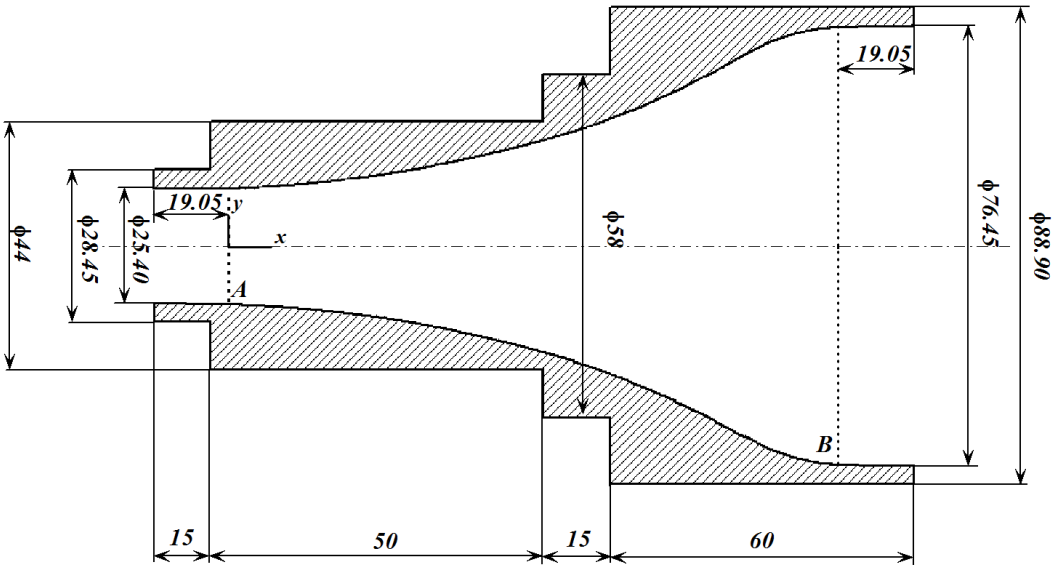

Figure II.4. Cutaway schematic of the axisymmetric nozzle geometry (Not to scale, dimensions in mm). Flow is in the negative *x* direction. Inner curvature of the nozzle is defined using a fifth order polynomial between sections A and B:

$$|y/R| = -3.9936(x/4)^5 + 4.9968(x/4)^4 + 0.5$$

Schedule 80 PVC) was added to the system to install the second flowmeter. Because of this parallel line, which has a smaller inner diameter (i.d. 25.4 mm) than the other PVC pipes in the system, the headloss of the flow loop increased. To maintain the specified flowrate, operating frequency of the motor was increased to 45.9 ± 0.5 Hz after the modification.

The water in the system is heated as the pump and the motor driving it operate. The heat is convected to the surrounding air via the PVC pipes and the tanks. In order to increase the convection, and consequently minimize the temperature fluctuations in the flow, two other tanks (T1 and T2) are added to the system. Other than this, no attempt

was made to control the temperature of the water in the system. The average temperature was measured by a sensor on the flowmeter (B1) to be 22°C with a variation of ±2°C between different LDV measurements. The fluctuation in the temperature can be as high as ±0.4°C during the measurement of a profile. The acidity of the water having seeding particles is measured as pH 7.4.

The calming section upstream of the test section (Fig II.2.) reduces free-stream turbulence levels and flow nonuniformities. This section consists of a coarse screen followed by a honeycomb, then two fine screens (1 and 2), a combination recommended by previous research for reducing turbulence levels (Farell and Youssef, 1996). The spacing between all the elements is shown in Figure II.2. The honeycomb (manufactured by *Indy Honeycomb* of Stainless steel 304) has hexagonal cells having a flat side to flat side dimension of 6.35 mm and wall thickness of 0.25 mm. The coarse screen and fine screens 1 and 2, all of stainless steel, have square cells with cell size of 9.6 mm, 2 mm and 1 mm, respectively. The freestream turbulence just downstream of the calming section, characterized by the rms fluctuations of the axial or streamwise velocity component u' was measured to be 0.9 percent upstream of an "empty" test section consisting of a straight piece of pipe.

A nozzle with a 9:1 area contraction ratio is installed 25 mm downstream of fine screen 2. The nozzle geometry is shown in Fig. II.4. The nozzle is manufactured from delrin by *G.M. Tooling*. The flow then exits the nozzle into the Vortigen tube, defined as the portion of the test section housing the swirl generator (or the straight fin) which is followed by the test section.

II.1.2. Wake and Swirl Generator Fins

All the measurements reported here were obtained in the glass pipe immediately downstream of the Vortigen tube. Two sets of studies on two different Vortigen concepts were carried out in this work. The first set of experiments on the single-vane Vortigen concept compared the flow downstream of a single straight vane, Fin IIIr, (Fig. II.5.) with that for a twisted vane with 180° twist about the pipe axis (Fig. II.6.) to determine how

Table II.2. Parameters in the straight fin geometries.

Fin	l_1*[mm]*	l_2*[mm]*	*d [mm]*	w_{le}*[mm]*	w_{te}*[mm]*	α [^{o}]	*Leading edge*
Fin-II	26.5	33.5	25.4	3.05	1.02	3.45	Straight
Fin-IIr	26.5	33.5	25.4	3.05	1.02	3.45	Rounded
Fin-III	34.5	25.4	25.4	3.05	1.52	3.45	Straight
Fin-IIIr	34.5	25.4	25.4	3.05	1.52	3.45	Rounded
Fin-IVr	54.7	5.3	25.4	1.34	1.02	3.45	Rounded

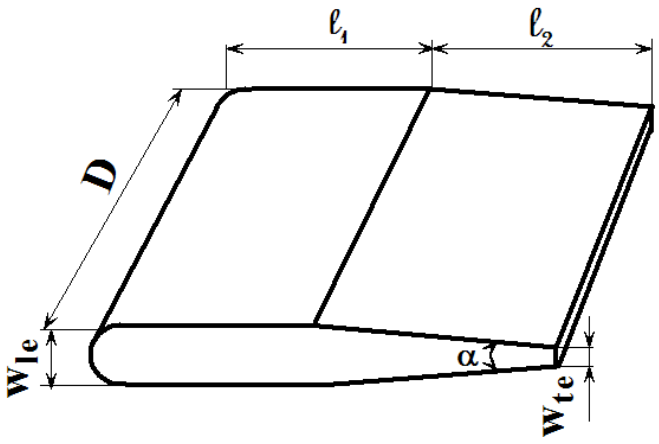

Figure II.5. Schematic of the straight fin (with a rounded leading edge).

the swirl generated by the twisted vane affected the flow characteristics. Both vanes had an overall streamwise length (x-dimension) of 59.9 mm and a width (y-dimension) of 25.4 mm; the length of the twisted fin measured along its (twisted) edge was 75 mm. The initial thickness of both vanes was 3 mm; the vanes then tapered linearly starting an axial distance 34.5 mm downstream of the rounded leading edge at a (half) angle of 1.73° to a trailing edge thickness of 1.52 mm. The twisted vane had a pitch to diameter ratio of 2.4. Both vanes were mounted with their leading and trailing edges along the vertical (z-direction). Four other straight fins with slight geometric variations from Fin IIIr were

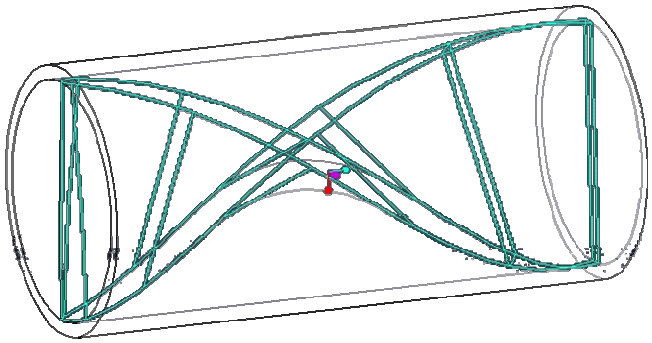

Figure II.6. CAD drawing (*Pro-E*) of the single twisted fin in the Vortigen tube. Leading edge of the fin is on the left.

also studied for calibration purposes and to ensure that variations in leading and trailing edge geometries had relatively little effect on these results. Parameters in the geometries of straight fins are compared in Table II.2. Note that Fins II and III have a straight (blunt) leading edge. Fins II, III and IIIr were made of aluminum; Fin IVr was made of phenolic and Fin IIr was made of delrin. The twisted fin was made by *Vistatek Inc.* using stereolithography rapid prototyping from *Somos Watershed 11120* resin.

Figure II.7. Photograph of SLA prototype of the swirler with four fins. Direction of the flow is out of the paper.

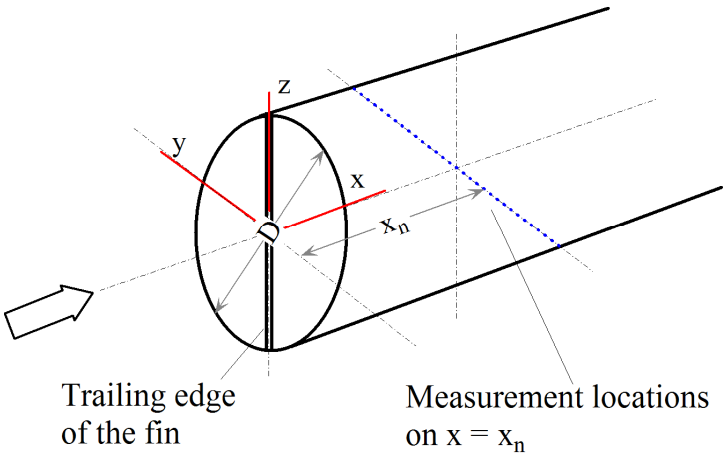

Figure II.8. Cartesian coordinate system and typical measurement locations on a profile at $x = x_n$. The flow is in the positive x direction.

The second set of experiments studied the flow downstream of a geometry modeling a more robust Vortigen concept consisting of four twisted vanes spaced evenly around the circumference of the Vortigen tube. Each of the vanes, when fabricated from a Ni-Ti SMA, will bend about 60° when heated above their austenite finish temperature, A_f, to the relatively stiff austentite phase and return to an untwisted, or straight, configuration at temperatures below martensite finish temperature, M_f, in their relatively soft martensite phase in the industrial application (See Appendix A). Fig. II.7 shows the geometry of the prototype of the four fins in the Vortigen tube (in their swirl generating shape). The prototype is again made by stereolithography rapid prototyping by *Vistatek* using the *Somos Watershed 11120* resin.

Fig. II.8 defines the coordinate system used in this work. Although a cylindrical polar coordinate system (r, θ, x) would be a natural choice for specifying a position in a pipe, a Cartesian coordinate system (x, y ,z) is used here for convenience since all the

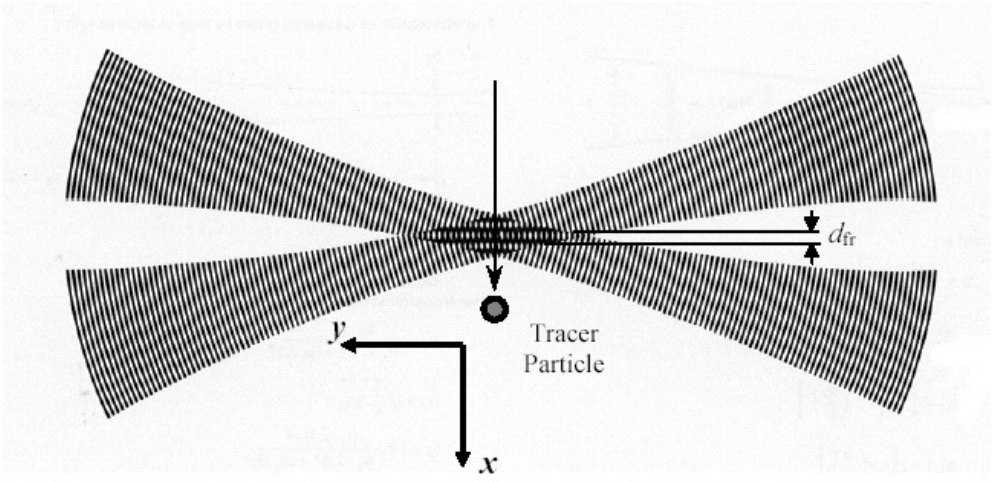

Figure II.9. Interference fringes (Adapted from Koehler 2004).

measurements are taken across the pipe diameter at $\theta = 0^{o}$. Radial profiles of the streamwise and azimuthal velocity components were obtained across the pipe diameter for $-R \leq y \leq R$ (See Fig. II.8) where $R = 0.5D$ at downstream positions measured from the trailing edge of the fin (or the tip of the trailing edge for the experiments with SMA vanes) ranging from $x/D = 0.8–10.8$. The opaque (gray) PVC supports just downstream of the trailing edge precluded optical access to the test section for $x/D < 0.8$.

II.2. Laser-Doppler Velocimetry (LDV)

II.2.1. Principles of LDV

Used extensively over the last four decades, laser-Doppler velocimetry (LDV) is an optical technique for obtaining instantaneous velocity data (Durst *et al*., 1981). When two coherent laser beams passing through the transmitting optics intersect at a certain angle, interference fringes are formed in a region called the probe volume (Fig II.9.). These dark and bright fringes correspond to regions where the amplitude of the laser beams cancel or reinforce each other based upon their relative phases, respectively. A tracer particle convected by the flow through the probe volume will then scatter light, and the intensity of this light will vary periodically as the particle passes through the alternating dark and bright fringes in this volume. The frequency of this scattered light will then depend upon the spacing of the fringes (d_{fr}), which is defined as the distance between the centerlines of two consecutive dark fringes, and the particle velocity ($\tilde{u}_i$). The fringe spacing is only a function of the half-angle between the laser beams (κ) and the wavelength of the laser illumination (λ):

$$d_{fr} = \frac{\lambda}{2\sin\kappa} \tag{II-1}$$

The velocity of the particle is equal to that of the fluid as long as the tracers follow the flow with perfect fidelity. The response of a tracer particle of diameter d_p and density ρ_p to velocity fluctuations in a flow with a density of ρ and kinematic viscosity μ is determined by the density ratio, s and the Stokes number, N_s (Durst et al. 1981):

$$s = \frac{\rho_p}{\rho} \tag{II-2}$$

$$N_s = \sqrt{\frac{\mu}{\rho\omega d_p^{\,2}}} \tag{II-3}$$

Here ω is the angular frequency of the fluctuations. For $s \leq 1$, the particle will follow the flow regardless of N_s. Otherwise, the diameter of the particle should be less than a maximum diameter to able to follow the flow.

The flow can be artificially seeded with tracer particles of an appropriate size range; tracers naturally found in the (usually water) flow can also be used in many cases. The velocity of the particle can then be calculated from the fringe spacing and the measured frequency of light scattered by the particle (f_D) detected, for example, by a photomultiplier tube (PMT):

$$\tilde{u}_i = f_D d_{fr} \tag{II-4}$$

This velocity is a nearly instantaneous velocity measurement, corresponding to that of the particle averaged over the time required for it to traverse the probe volume. Moreover,

the specific velocity component measured using this procedure is that normal to the fringes.

In most cases, a PMT is used to detect and amplify the light scattered by the tracer particle and to convert this signal into a measurable voltage. In the so-called backscatter mode, the receiving optics and detector (*e.g.*, PMT) are placed on the same side of the flow as the transmitting optics, and the detected light is scattered back towards the PMT. In the forward scatter mode, the receiving optics and detector are placed on the opposite side of the flow from the transmitting optics. Generally, higher signal levels and hence sampling rates are achieved in forward scatter, but the alignment of the receiving and transmitting optics is more complicated. In backscatter systems the transmitting and the receiving optics can be integrated into a single unit, greatly reducing alignment difficulties. The voltage from the PMT is input into a counter processor, a device that isolates the signal from the background noise and the frequency pedestal using a band pass filter and amplifies the signal.

LDV suffers from "directional ambiguity" in that two particles moving in opposite directions in the probe volume at the same speed will give the identical signals. To overcome this, the frequency of one of the laser beams can be shifted relative to the other—equivalent to adding a positive offset to all velocities so that the negative velocities corresponding to backflow will be positive but less than those corresponding to forward flow. A Bragg cell with a piezoelectric transducer is used in most cases to increase the frequency of one of the beams. Durst, et al. (1981) and Goldstein (1983), among others, extensively review the technique and its development.

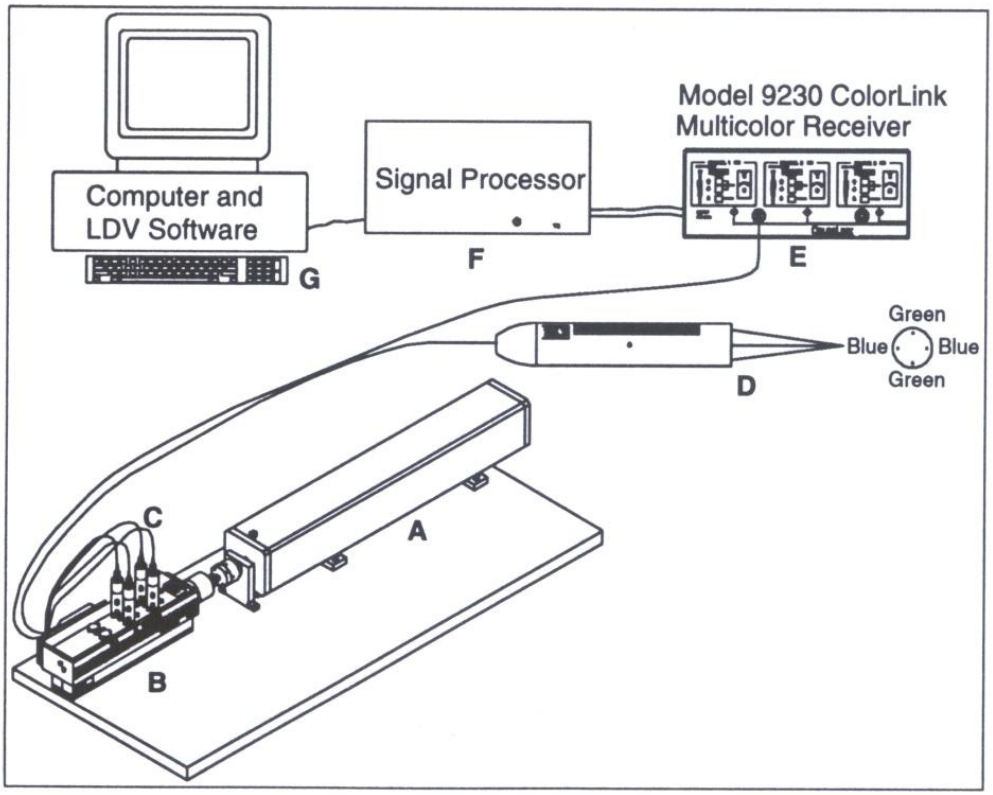

Figure II.10. LDV System and its main components (Adapted from *Find for Windows Instruction Manual*, *TSI Inc*, 1998).

II.2.2. LDV System and Procedures

Velocities were measured using a two-component laser-Doppler velocimetry system (TSI, Inc.) in backscatter mode with a water cooled argon-ion laser (*Coherent Innova 70*), with the two laser beams along the horizontal midplane of the pipe. The single-line laser (blue, at 488 nm wavelength) was operated at a laser power of 2 W which was the highest attainable power. The maximum sampling rate was about 1 kHz. The flow is artificially seeded using α-alumina particles, having a specific gravity of 3.8425 and a nominal diameter of 0.3 μm.

The main components of the LDV system are shown in Figure II.10 and listed in Table II.3. The major operating parameters of the LDV system are summarized in Table II.4.

In the measurement of both the axial and the azimuthal velocity components, the LDV signal is filtered with a band pass filter (0.3–3 MHz) to reduce the noise level in the signal and to eliminate the signal pedestal. The average axial velocity of the flow, 3.09 m/s (at a flowrate of 181.8 L/min) creates a Doppler signal with a frequency of about 0.91 MHz. To resolve negative velocities from positive velocities, a Bragg cell is used to obtain a frequency shift of 1 MHz for all measurements of azimuthal velocity.

The measurement volume created by the intersection of the laser beams is an ellipsoid whose dimensions can be calculated using Eqs. II-5, II-6 and II-7 (Goldstein, 1983). The axes of the ellipsoid in the x, y and z directions are ℓ_m, d_m and h_m respectively

$$d_m = \frac{d_e}{\cos \kappa} \tag{II-5}$$

$$\ell_m = \frac{d_e}{\sin \kappa} \tag{II-6}$$

$$h_m = d_e \tag{II-7}$$

Here d_e is the beam diameter at the focal waist (*i.e.*, at the intersection of the beams). It can be approximated using the beam diameter ahead of the converging lens of the laser probe (D_e), (Goldstein 1983):

Table II.3. List of the main components of the LDV system shown in Fig. II.10.

Label	*Type*	*Item*	*Model No.*
A	LASER	Laser	Coherent Innova 70
		Riser Base	TSI 91470
B	LDV	Beam Collimator	TSI 9108
		Input Beam Alignment Tube	TSI 10969
		Color Burst Multicolor Beam Separator	TSI 9201
		Natural Density Filter	TSI 10964
C		Fiberoptic Couplers	TSI 9271E
D		Probe Lens	TSI 9253-350
E	SIGNAL ANALYSES	Receiver	9230-2, Serial No: 358B
F		Processor	IFA 650-2, Serial No: 134
G	SOFTWARE	TSI Find for Windows	Ver. 1.4
H	TRAVERSING	Velmex Unislide	MB6033Q2J-S6(2)-PC
	MECHANISM	3 Stepping Motors, Superior Electric (2.5 V, 4.6 A, 200 Steps/rev.)	SLO S×N, MO92-FD-447
		Velmex Three Axis Motor Controller	VP9003

Table II.4. Operating parameters of the LDV system.

Parameter	***Symbol***	***Value***
Fringe Spacing (μm)	d_{fr}	3.602
Beam half angle in air (^{o})	κ	4.096
Beam spacing (mm)	D_b	50
Focal Length (mm)	f	350
Laser wave lengths (nm)	λ_1	514.5 (green)
	λ_2	488 (blue)
Beam diameter (mm)	D_e	4

$$d_e \cong \frac{4f\lambda}{\pi D_e} \tag{II-8}$$

Using Eqs. II-5, II-6, II-7, II-8, and the parameters of the LDA system given in Table II.4., the dimensions of the LDA probe volume are approximated to be 0.06 mm × 0.8 mm × 0.06 mm in the *x*, *y* and *z* directions respectively. The volume of the ellipsoid can then be calculated using (Goldstein, 1983):

$$V_D = \frac{\pi d_e^{\,3}}{6\cos\kappa\sin\kappa} \tag{II-9}$$

However, as described in the next section, the beam half-angle κ may change along the radial span of the pipe because of refraction of the laser beams as they pass through the glass pipe walls and index-matching and working fluids. The dimensions of the

measurement volume may therefore vary with the probe volume location. When the two beams intersect in air, $\kappa = 4.096°$, and the measurement volume is about 1.36×10^{-3} mm^3.

The length of the long axis of the ellipsoid, ℓ_m, is an order of magnitude larger than the other dimensions of the ellipsoid. It therefore determines the minimum spatial resolution of these LDV data. As $y/R \rightarrow 1$ in the pipe, the probe volume approaches the side of the pipe farthest away from the transmitting and receiving optics, $\ell_m \rightarrow 1.6$ mm (*vs.* 0.8 mm in air) in the measurement of the azimuthal velocity component, significantly degrading the spatial resolution of the measurement.

II.3. Experimental Procedures

The experimental procedures followed during the measurement of a typical radial velocity profile are described in the following paragraphs. The procedure used to align the LDV probe head will be discussed later in this section.

1. *Open the laser water cooling line. Turn on the laser. Turn on the pump driving the water in the system.*

2. *Stop the pump. Observe the backflow in the calming section to see if particles are visible in the water. If the water in the system contains visible particles, drain the system, remove the calming section, and clean the tanks, the filter and the calming section. Then realign the probe head and wait for the temperature of the water to equilibrate to room temperature.*

If no particles are visible in the water, wait about half an hour. During this period, the air trapped inside the flow loop leaves the system, and the air bubbles that

were initially visible in the flow disappear. The flowrate measured by the flowmeter stabilizes to ±1% of its mean value.

3. *Add (α-Alumina) tracer particles into tank T3.* Although the concentration of particles in the flow loop was not monitored, the tracers are added to the tank at a maximum concentration of 5 g/m^3.

4. *Run the LDV software ("FIND", TSI Inc.) on the microcomputer coupled to the LDV system (cf. Fig. II.10.).*

5. *Move the probe head in the positive y direction until an LDV signal is detected using the three-dimensional computer controlled traversing mechanism.*

6. *Adjust the pump frequency on the frequency controller until the flowrate reading of the flowmeter shows the desired flowrate (181.8 L/min=24 GPM).* The frequency controller has a resolution of 0.1 Hz.

7. *Start data collection.* The LDV probe head was traversed automatically along the positive *y*-direction, stopping at specified radial (*y*) locations. Data were collected at each *y*-location over 60 seconds, unless the number of samples exceeded a prespecified level before this.

The convective time scale based on the fin thickness is given by

$$\tau_t = \frac{t}{U_0} \approx 1\ \mu s \qquad \text{(II-10)}$$

where the fin thickness t = 3.05 mm and the average velocity U_0 = 3.09 m/s. For this turbulent flow, the data collection times should be at least 4 orders of magnitudes greater than τ_t at each measurement location, corresponding to a minimum data collection duration of 10 s. Data were therefore collected in all cases over an interval of at least 10 s, and the maximum number of samples was prespecified to be between 10,000 and 50,000 for the LDV profiles.

8. *Turn off the laser and the pump after the data collection for all the radial locations at each specified axial location are completed.*

9. Calculate the LDV statistics using the FIND software. Mean velocities and rms velocity fluctuations were calculated for the axial (U and u', respectively) and/or azimuthal (V and v', respectively) components of the velocity.

10. *Apply appropriate corrections to the azimuthal velocity and the radial location values.* These data need to be corrected to compensate for the refraction of the laser beams through the different media between air and the working fluid (*i.e.*, water).

Proper alignment of the probe head with respect to the test section is required for accurate LDV data. The LDV probe head, which consists of both the transmitting and receiving optics, is first mounted on a three-dimensional computer-controlled traverse (*cf.* Table II.3 and Fig. II.3.). The probe head is then aligned to the horizontal x-y plane using a bubble level fixed to the traverse.

In all the experiments, the two laser beams used to measure the axial velocity component (referred to as the "horizontal beams") enter the glass pipe along its

horizontal midplane. Thus, the horizontal beams do not "see" the curvature of the pipe wall, assuming the beam diameter is much smaller than the pipe radius. On the other hand, the other pair of laser beams measuring the azimuthal velocity component (the "perpendicular beams") enters the pipe on a line perpendicular to the pipe axis, and their path is affected by the curvature of the pipe wall. The laser beam alignment is carried out in two steps. First, the probe head is traversed along the z-axis using the three-dimensional traverse until the horizontal beams are along the horizontal midplane of the pipe. The probe head is then traversed along the x-axis until the perpendicular beams are at the first axial (x) location for the measurement of the radial velocity profiles, or 0.8 pipe diameters downstream of the trailing edge of the fin(s).

As shown in Fig. II.11, the following procedure is used to align the horizontal laser beams with the midplane of the pipe. First, the probe head is traversed upwards along the z-axis, until the horizontal beams are both above the pipe. The laser beams directly hit the wall of the room where the experimental facility is located, corresponding to location P_1 on Fig. II.11.

Second, the probe head is traversed downwards along the z-axis, towards the pipe, in 0.05 mm increments until horizontal beams cross the glass pipe. The z-location of the laser beams when they first hit the wall of the glass pipe at P_2 can be easily determined by observing the facing wall; when the beams first hit the glass wall, they are no longer visible on the wall because they are then reflected off the outer surface of the pipe wall. This z-location corresponds to the outer surface of the glass pipe:

$$z = \frac{D}{2} + t = 14.22 \text{ mm} \qquad \text{(II-11)}$$

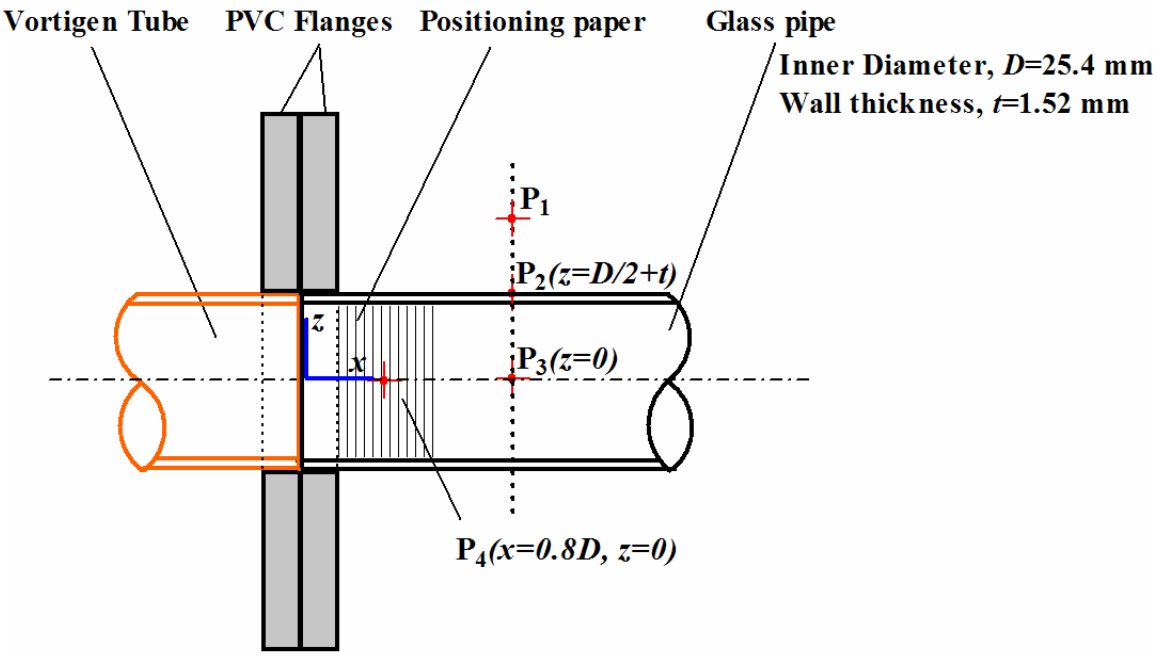

Figure II.11. Detail from the test section showing the Vortigen tube and part of the glass pipe (not to scale). P_1, P_2, P_3 and P_4 are locations of laser beams in the procedures for the positioning of the probe head. The flow is in the positive *x* direction.

where t is the thickness of the glass pipe.

The probe head is then traversed 14.22 mm downwards along the z-axis. At this location (P_3), the horizontal beams should cross the pipe at $z = 0$, *i.e.* the beams enter the pipe through its horizontal midplane. The uncertainty associated with this alignment on the z-axis, assessed by repeating the procedure at various axial locations, was found to be ± 0.3 mm.

After aligning the horizontal beams, the front face of the probe is aligned parallel to the x-axis, or centerline, of the pipe so that the LDV probe head remains a constant y-distance from the test section for all axial locations of interest. First the probe lens is taken off of the probe head, so that the laser beams are parallel (*i.e.* $\kappa = 0$). Then, the

reflections of the perpendicular beams (offset along the z-direction) off the outer glass pipe wall on the front face of the LDV probe are observed while the test section is rotated about the z-axis (*i.e.*, in the x-y plane). We assume that the probe and the test section are parallel when these reflections on the probe face and the laser beams are all on the same vertical line.

After aligning the test section with respect to the probe head, the perpendicular laser beams are moved to the initial axial location $x = 0.8D$ (point P_4), indicated by a piece of paper attached to the glass pipe wall (or the wall of the index matching tank) just downstream of the PVC flange. The probe head is moved from P_3 on the x axis in 0.25 mm increments upstream towards the Vortigen tube until the axial location of the perpendicular beams are fixed on P_4 as marked on the paper. The uncertainty associated with this alignment on the x-axis is therefore ± 0.25 mm. After this initial location is set on the traverse, the positioning paper is removed, and the probe head is traversed to the desired axial measurement locations.

II.4. Partial Refractive-Index Matching and Corrections to the LDV Measurements

A pair of laser beams that intersect a refractive-index interface between different optical media at a non-normal angle of incidence will be bent or refracted, changing their direction and, as a result, shifting their point of intersection and changing the angle between the beams. In LDV measurements, the location of the probe volume and the magnitude of the velocity must be corrected when the laser beams pass through different optical interfaces between the laser probe and the measurement location. If the refraction

occurs at a curved interface between media such as air and the outer wall of a pipe, this refraction is also known as “lensing”.

Snell’s law predicts the refraction of a laser beam passing from a medium with refractive index n_i into a medium with index n_t:

$$n_i \sin \theta_i = n_t \sin \theta_t \tag{II-12}$$

where θ_i is the angle of incidence and θ_t is the angle of transmission, both measured from the normal to the interface between the two media. Note that the wavelength of the laser beam in a medium of a given refractive index n_i will also be changed as it passes into another medium with index n_t:

$$\lambda_i n_i = \lambda_t n_t \tag{II-13}$$

The change in the wavelength, unlike the change in the path of the beam, is independent of the shape of the interface between the mediums.

According to Eq. II-4, the instantaneous velocity of a tracer particle is directly proportional to the fringe spacing and the Doppler frequency:

$$\tilde{u}_i = f_D d_{fr}$$

The fringe spacing is determined by two parameters, namely the laser wavelength λ and the half angle of the beams κ (Eq. II-1):

$$d_{fr} = \frac{\lambda}{2 \sin \kappa}$$

Although κ is altered by refraction and the wavelength depends on the medium of propagation, the LDV system software calculates the mean and rms velocities using the values of κ and λ in air. We must therefore correct these values *a posteriori* to compensate for changes in the wavelength and half angle.

Steenbergen (1996), Velidandla *et al.* (1994) and Lowe and Kutt (1992), among others, discuss and suggest solutions for the problem of refraction through curved walls. One of the most widely used techniques used to compensate for the lensing effect at curved pipe walls is refractive-index matching. In this method, the pipe is immersed in a tank having flat walls that allow optical access. When the tank is filled with an "index-matching fluid", *i.e.*, a fluid with a refractive index equal to that of the pipe walls, refraction due to the outer curvature of the pipe is eliminated. By then matching the refractive index of the working fluid in the pipe to that of the pipe walls, refraction due to the inner curvature of the pipe can also be eliminated.

Another method applied to overcome lensing effects is the use of corrective lenses (Steenbergen 1996, Velidandla *et al.* 1994) to alter the path of the laser beams so that the beams will follow the (original) desired path when refracted through the pipe wall. Reducing the pipe wall thickness and hence the amount of refraction can also be used to minimize lensing effects due to pipe wall curvature (Steenbergen 1996).

Lowe and Kutt (1992) describe an experimental method, as opposed to the analytical methods described in the previous paragraphs, for accurately determining the location and dimensions of the laser probe volume inside a pipe. They basically view their test section from two orthogonal directions to determine the path of the refracted

pair of laser beams. Durst et al. (1998), Kehoe (1984), Kehoe and Desai (1987), Timofeev (1983), Boadway and Karahan (1979) and Glover et al. (1985), among others, also give different methods to determine the measurement location for LDV studies of pipe flow.

This study used an analytical approach to determine the measurement location in the pipe and to correct the velocity components for the effects of refraction. When measuring the azimuthal velocity component, which is important in characterizing the swirl flow and accurately determining the swirl number at various downstream locations, refractive-index matching is required to reduce lensing effects due to the curved wall of the pipe and obtain accurate LDV data. A rectangular tank (340 × 40 × 50 mm) of optical glass (manufactured by *Abrisa*) with a wall thickness of 3 mm was filled with glycerin, a liquid whose refractive index (1.47) is virtually identical to that of the pipe wall, and attached to the test section so that it surrounds the pipe (Fig. II.12). A 340 mm long (axial dimension) portion of the test section is inside this index-matching tank.

In the LDV measurements, the laser beams travel through air, the glass wall of the index matching tank, glycerin, the glass wall of the pipe and water. The refractive indices of these media are given in Table II.5. The refraction of the beams as they pass through these five different media changes the direction of the beams, and hence the beam half-angle, in each medium. The LDV software supplied by TSI assumes that this angle is constant, however, when converting the LDV signal into velocities. To obtain accurate velocity values, the change in the half angle and the wavelength of the laser beams must be taken into account and the velocity "data" from the LDV software need to be corrected to account for these changes. In a similar fashion, the radial (y) location of the

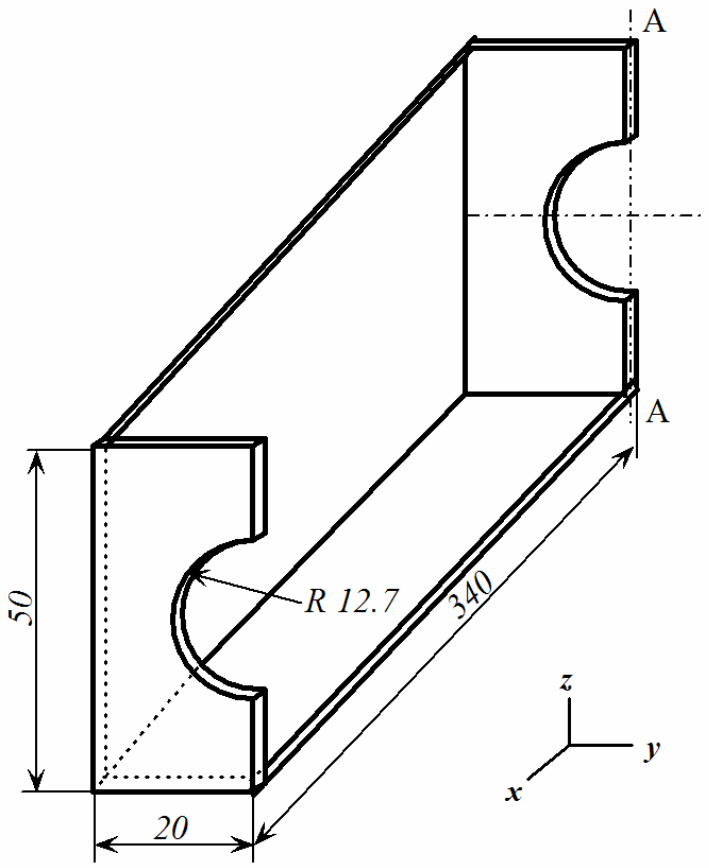

Figure II.22. Schematic of the index matching tank of optical glass. (Not to scale, dimensions in mm). One half of the tank is shown. The other half is symmetric along A-A. Parts of the tank are glued around the test section (*i.e.*, the glass pipe), and then the tank is filled with glycerin.

Table 2.5. Refractive indices of the mediums that the laser beams pass through in the LDV measurements.

Medium	***Symbol***	***Refractive Index***
Air	n_a	1.000
Glass (index matching tank)	n_{g1}	1.52
Glycerin	n_m	1.47
Glass (pipe)	n_{g2}	1.47
Water	n_w	1.33

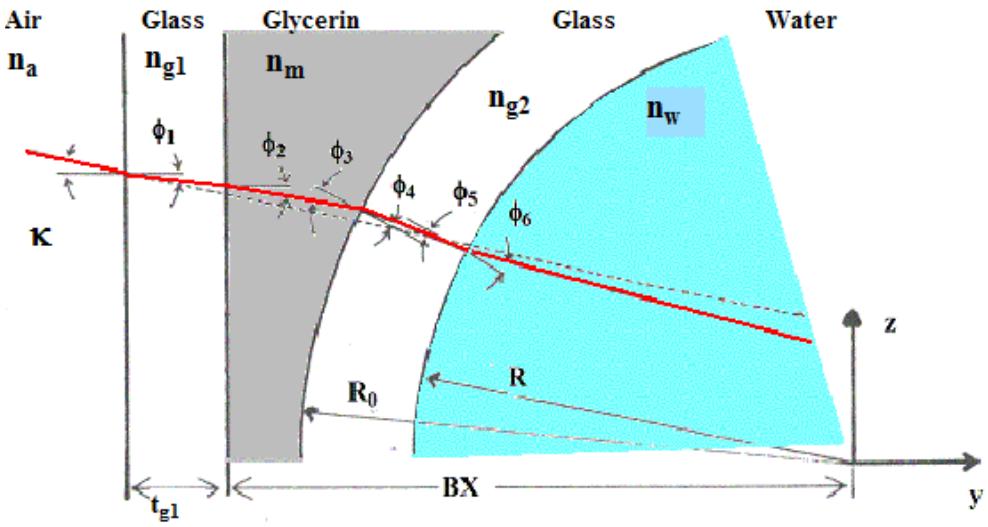

Figure II.13. Typical path of a laser beam in the measurement of the azimuthal velocity component. The beams travel through the glass wall of the index matching tank, index matching medium (glycerin), the glass wall of the pipe and water. Adapted from Glover *et al.* (1985).

measurement volume reported by the software must be corrected to account for the effects of refraction.

II.3.1. Azimuthal Velocity Measurements

In Fig. II.13., the optical path of a single horizontal laser beam used to measure the azimuthal velocity component is shown. The equations used to calculate the angles of incidence in the different optical media (*i.e.* θ_1, θ_2, θ_3, θ_4 and θ_5), which are shown in Fig. II.13. are given below (following Glover *et al.* 1985):

$$\sin\theta_1 = \frac{\sin\kappa}{n_{g1}} \qquad \text{(II-14)}$$

$$\sin\theta_2 = \frac{n_{g1}}{n_m}\sin\theta_1 \qquad \text{(II-15)}$$

$$\sin\theta_3 = \frac{\cos\theta_2}{R_0}\left[BX\left(\tan\kappa - \tan\theta_2\right) + t_{g1}\left(\tan\kappa - \tan\theta_1\right) + Y'\tan\kappa\right] \tag{II-16}$$

$$\sin\theta_4 = \frac{n_m}{n_{g2}}\sin\theta_3 \tag{II-17}$$

$$\sin\theta_5 = \frac{R_0}{R}\sin\theta_4 \tag{II-18}$$

$$\sin\theta_6 = \frac{n_{g2}}{n_w}\sin\theta_5 \tag{II-19}$$

where θ_6 is the actual half angle of the laser beams in water and Y' is the displacement of the laser probe. The actual displacement of the laser beams inside the pipe, Y, can be calculated using Eq. II-20:

$$Y = \frac{R_0\dfrac{m_m}{m_w}\sin\theta_3}{\sin(\theta_2 + \theta_3 - \theta_4 + \theta_5 - \theta_6)} \tag{II-20}$$

These relations can be derived by applying the Snell's law at the four interfaces between the five different media and using geometrical relations to simplify the resultant expressions. The velocity measurements are corrected by taking the change in the half angle (*i.e.* $\kappa = \theta_6$) and laser wavelength ($\lambda = \lambda_t$) into account in the calculation of the fringe spacing (Eq II-1). When $Y' = 0$, the actual displacement Y is found to be 3.14 mm. This result suggests that certain radial positions near the wall will not be optically accessible due to the refraction for the LDV measurements. This "blind spot" occurs for $-1 < y/R \leq -0.8$.

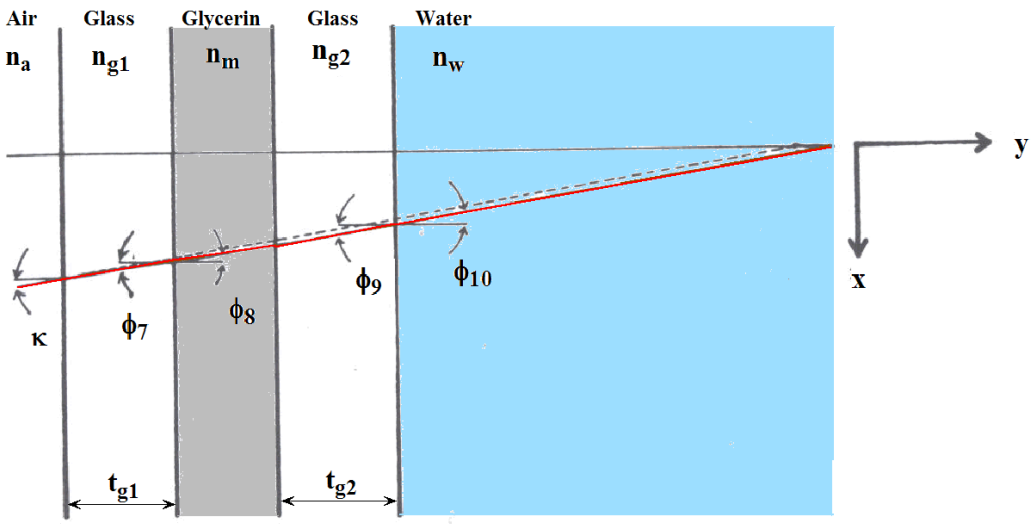

Figure II.14. Typical path of a laser beam in the measurement of the axial velocity component. The beams travel through the same mediums as in Fig. II.13. Adapted from Glover *et al.* (1985).

II.3.2. Axial Velocity Measurements

Fig. II.14 shows the optical path of one of the perpendicular laser beams used to measure the azimuthal velocity component. The angles of incidence in the different media are θ_7, θ_8, θ_9, and θ_{10}. The actual displacement of the laser beams are calculated in two steps using Eqs. II-21 and II-22 (following Durst *et el.* 1981). In the first step, the actual location of the beams Y'' in the index matching fluid (glycerin) is calculated, and then the actual displacement Y, in the working fluid (water) is calculated using Y'' (recall that Y' is the displacement of the laser probe).

$$Y'' = \left[Y' + t_{g1} \left(1 - \frac{\cos\kappa}{\sqrt{\left(\frac{n_{g1}}{n_a}\right)^2 - \sin^2\kappa}} \right) \right] \frac{1}{\cos\kappa} \sqrt{\left(\frac{n_m}{n_a}\right)^2 - \sin^2\kappa} \qquad \text{(II-21)}$$

$$Y = -R + \left[Y'' + t_{g2} \left(1 - \frac{\cos\theta_8}{\sqrt{\left(\frac{n_{g2}}{n_m}\right)^2 - \sin^2\theta_8}} \right) \right] \frac{1}{\cos\theta_8} \sqrt{\left(\frac{n_w}{n_m}\right)^2 - \sin^2\theta_8} \qquad \text{(II-22)}$$

Here $\theta_8 = \theta_2$. When Y'=0, the actual displacement Y = 1.34 mm; this result suggests that there is another "blind spot" where LDV measurements are infeasible over $-1 \leq y / R \leq -0.9$.

For the axial velocity measurements, the curved wall of the pipe is essentially planar for the horizontal beams. Snell's Law can therefore be applied at the air-water interface without worrying about any intermediate media (Eq. II-12). When expressions for the laser wavelength and the half-angle between the beams in water are substituted into the fringe spacing equation (Eq II-1), it can be seen that the spacing of the fringes, d_{fr}, does not change. Hence the axial velocity component results given by the LDV software do not need correction.

CHAPTER III

RESULTS and DISCUSSIONS

This chapter describes laser-Doppler velocimetry (LDV) measurements downstream of three different fin geometries, two of which model various Vortigen concepts: 1) a straight single fin (for calibration purposes); 2) a twisted single fin; and 3) four twisted fins. LDV results in terms of radial profiles of the mean values and rms fluctuations of the axial and azimuthal velocity components are presented for each geometry. The effects of variations in fin geometry are then discussed by comparing the results for three different straight fins with different leading and trailing edge geometries. Then the self-similarity of the wake downstream of the straight fin is discussed. The impact of swirl upon the flow is discussed by comparing the results for the straight and twisted single fins. Finally, the swirl characteristics of the four twisted fins are compared with those for the single twisted fin.

The standard errors on sets of velocity profiles presented in this chapter, as shown on one of the profiles in each figure, are as follows: ±1% for the mean velocity and ±3% for the rms fluctuation velocity unless annotated otherwise (*cf.* Appendix B).

III.1. LDV Measurements of Axial and Azimuthal Velocity

Two-component LDV measurements were performed in the flow loop at a Reynolds number of 80,000 based on average axial velocity and inner tube diameter. The streamwise and azimuthal (tangential) velocity profiles *u(y)* and *v(y),* respectively, were measured across the horizontal inner diameter of the tube at different x, or downstream, positions measured from the trailing edge of the fin(s). The opaque (gray) PVC supports just downstream of the trailing edge precluded optical access to the test section for $x/D <$ 0.8. LDV profiles were therefore obtained at x/D = 0.8, 2.8, 4.8, 6.8, 8.8 and 10.8. At each *x* position, velocity profiles were obtained over 30 to 90 radial (y) locations. The y-spacing between adjacent measurement points varied from about 0.85 to 0.28 mm. The regions adjacent to both the "far" and "near" pipe walls (with respect to the LDV probe head) were optically inaccessible for the following reasons:

- Refraction of the laser beams at the near wall ($y/R = -1$) precluded LDV measurements for $-1.00 < y/R < -0.9$ in the measurement of the axial velocity and for $-1.00 < y/R < -0.8$ in the measurement of the azimuthal veloctiy

- Attenuation of the laser beams and the Doppler-shifted signal due in part to scattering by seed particles as they propagate through the fluid led to unacceptably low sampling rates near the far wall ($y/R = 1$). It was therefore practically infeasible to obtain LDV measurements for $0.9 < y/R < 1$ in most of the measurements.

In addition, the sample *y*-spacing within a LDV profile could vary for *v(y)* measurements as the constant position increments of the probe head in air lead to different position

increments of the probe volume in the fluid due to refraction of the laser beams by the curved pipe walls (*cf.* Chapter II).

In the figures presented in this section, the mean values (denoted by uppercase variables) and rms fluctuations (denoted by primed variables) of the axial and azimuthal velocity components are normalized by the average flow speed U_0 = 3.09 m/s. The radial location y is normalized with the pipe radius R.

III.1.1. Straight Single Fins

Figs. III.1 and III.2 show the radial profiles of the axial mean velocity and its rms fluctuations for Fin III at x/D = 0.8, 2.8, 4.8, 6.8, 8.8 and 10.8. These profiles are essentially symmetric about the pipe centerline (y = 0). At farthest upstream location of x/D = 0.8, a small region of constant velocity unaffected by either the pipe wall boundary layers or fin wake can be observed; this region is gone by x/D = 2.8. As expected, the profiles become more uniform and the velocity defect due to the wake decreases as x/D increases.

The fluctuations are greatest in the boundary layers on the pipe walls and the wake (with a slight "dip" at y = 0), decreasing to a minimum value at the radial location corresponding to the maximum axial mean velocity. The profiles again become more uniform as x/D increases.

In order to look at the effect of the leading edge shape, LDV measurements are carried out for the wake of Fin IIIr which is identical to Fin III except that it has a rounded leading edge as shown in Fig. II.5. Axial mean velocity profiles are presented in Fig. III.3. and rms values of the fluctuations are presented in Fig. III.4. Downstream

locations are the same as in the profiles with Fin III. Looking at the mean velocities, it is clear that the general trend in the profiles is not different than the results with Fin III. However, the development of the minimum velocity at $y/R = 0$ is different than the results with Fin III. The rate of decrease follows such a pattern that, a slow region is followed by a faster region and then by another slower region. Looking at the rms fluctuations, it can be seen that, from $x/D = 2.8$ to $x/D = 4.8$ the defect turns into a sharp peak which completely disappears at the next downstream location, $x/D = 6.8$.

Figs. III.5. and III.6. show the azimuthal (or tangential) velocity profiles for Fin IIIr at four downstream locations between $x/D = 0.8$ and $x/D = 6.8$. As expected, the mean azimuthal velocity component is essentially zero in the bulk of the flow away from the walls (*i.e.* $-0.8 \leq y/R \leq 0.8$). Close to the walls it reaches to about 40% of the average axial velocity. Fig. III.6. shows the rms fluctuation velocity profiles. For a large portion of the radial span the rms fluctuation is at about 5% of the average velocity (*i.e.* $-0.6 \leq y/R \leq 0.6$) which is comparable to the axial rms fluctuations (Fig III.4.) at the same axial locations. Near the pipe wall, rms fluctuations climb to about 50 % of the average velocity.

Radial profiles of the axial mean velocity at $x/D = 0.8$, 2.8, 4.8 and 6.8 are shown for Fin II in Fig III.7. These profiles are essentially symmetric about the pipe centerline ($y = 0$). The profiles and their evolution with x/D are similar to those observed for Fin III.

Fig. III.8.depicts the rms fluctuations of the axial velocity component at the axial locations shown in Fig. III.7. These profiles show a marked asymmetry, and appear to be "skewed".

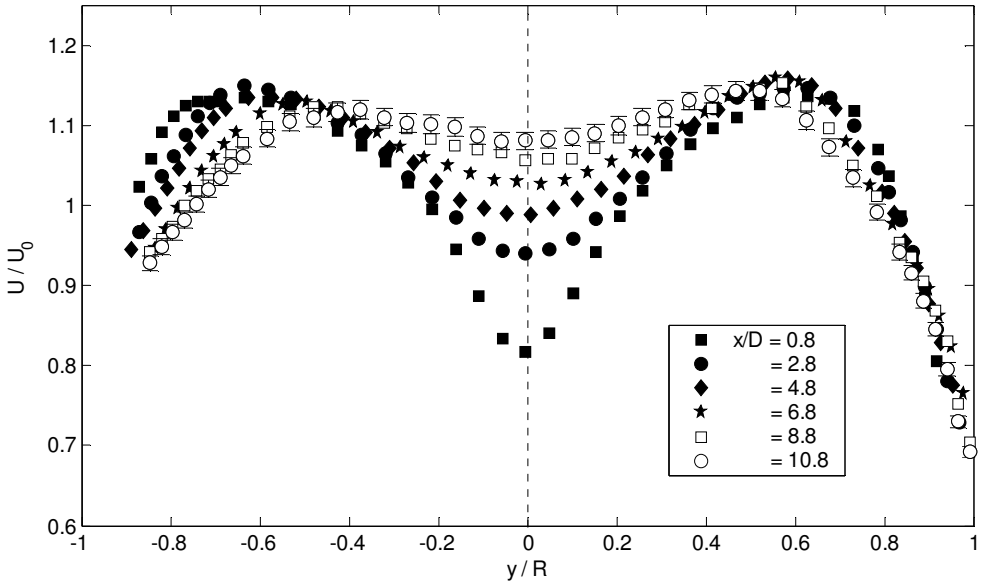

Figure III.1. Axial mean velocity profiles for Fin III.

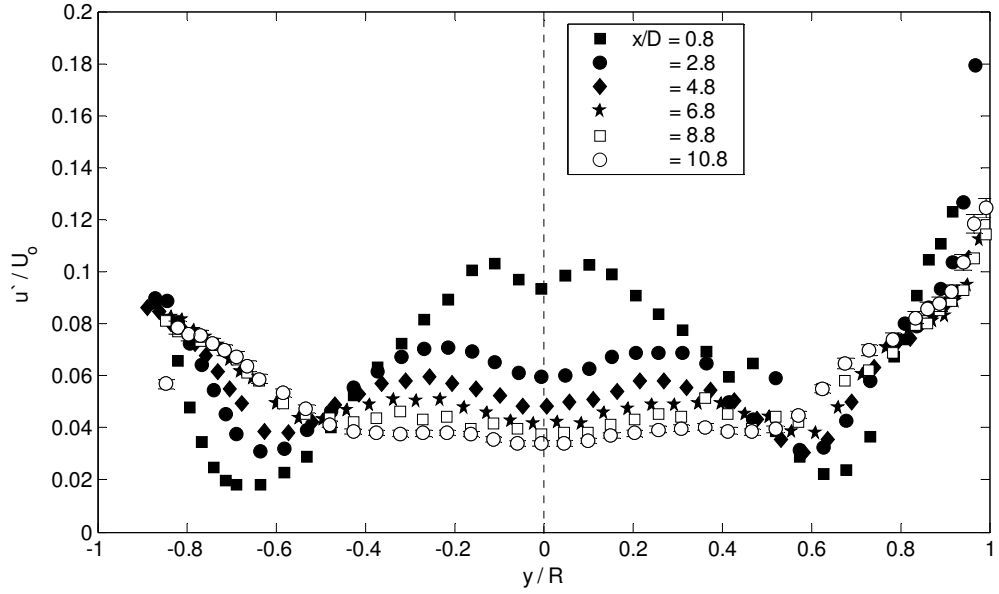

Figure III.2. Axial rms fluctuation velocity profiles for Fin III.

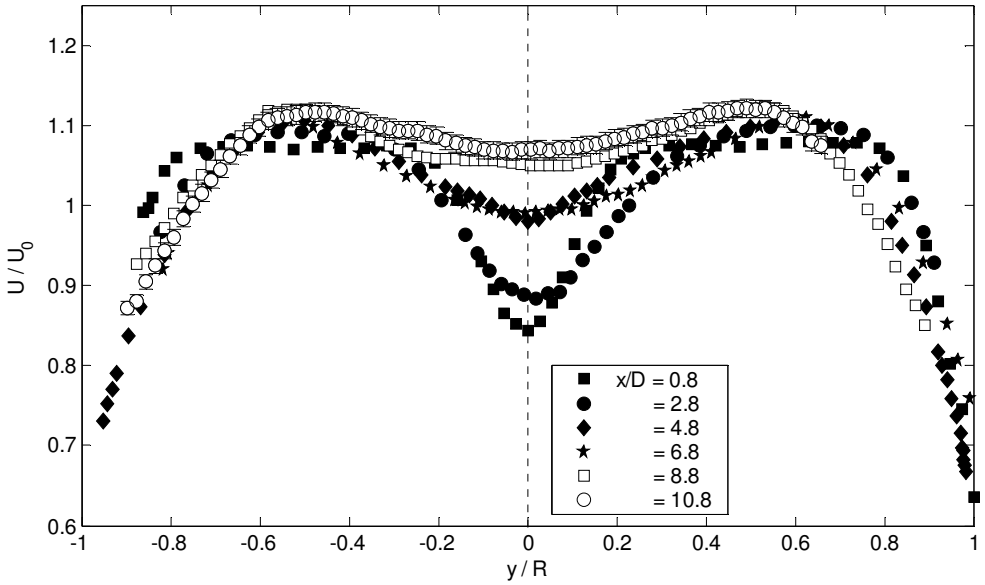

Figure III.3. Axial mean velocity profiles for Fin IIIr.

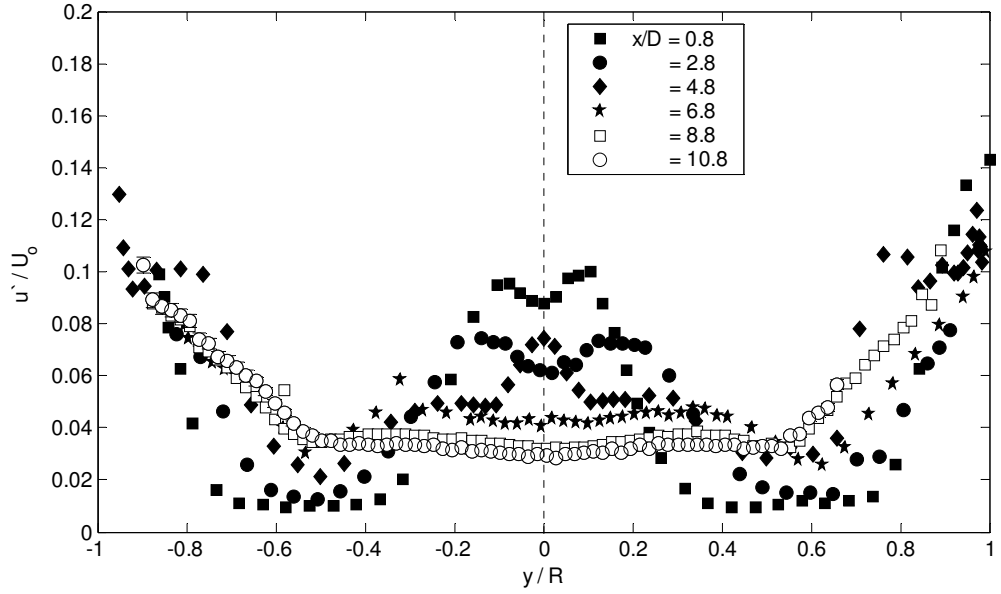

Figure III.4. Axial rms fluctuation velocity profiles for Fin IIIr.

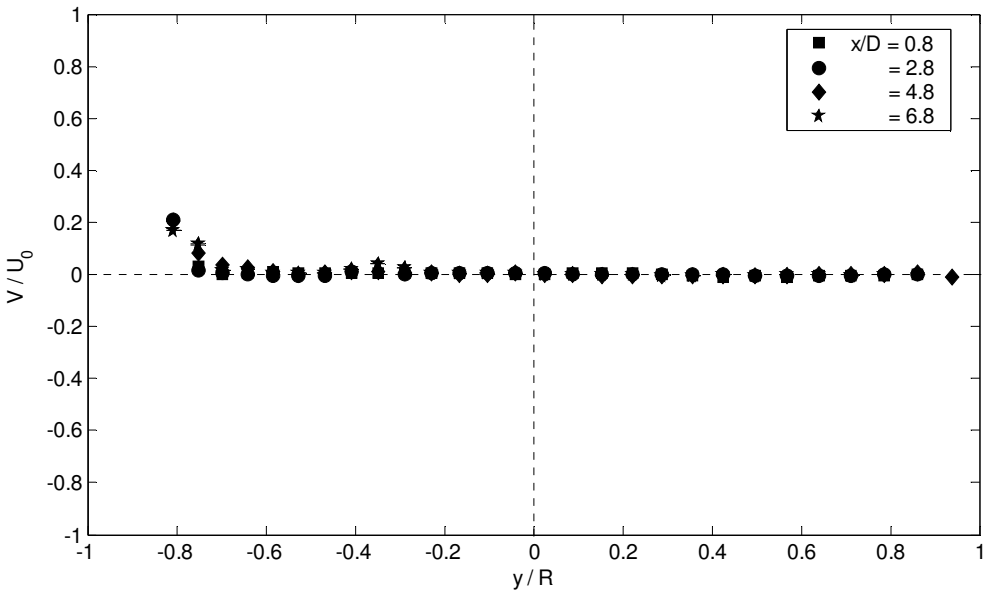

Figure III.5. Azimuthal mean velocity profiles for Fin IIIr.

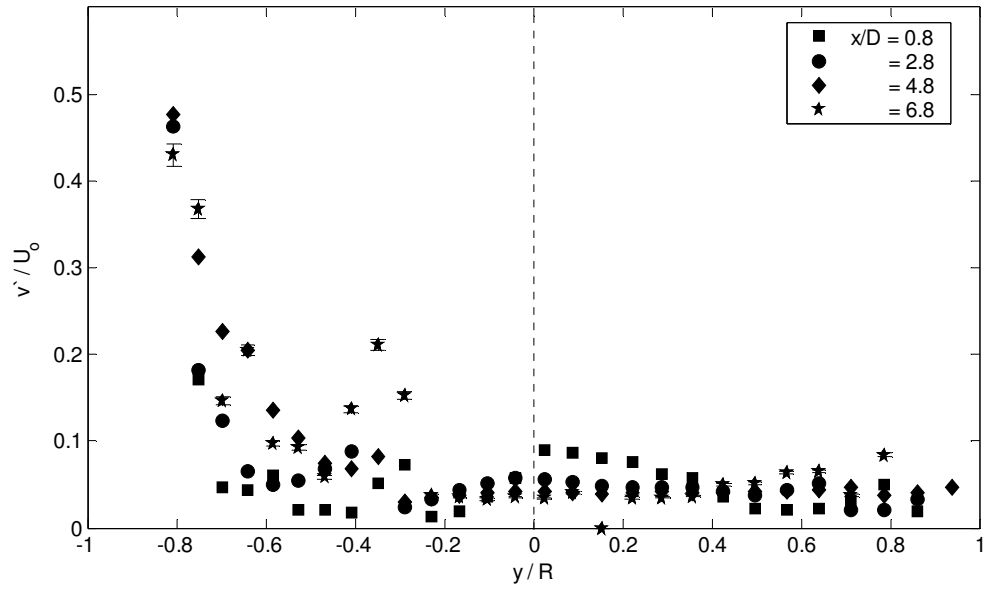

Figure III.6. Azimuthal rms fluctuation velocity profiles for Fin IIIr.

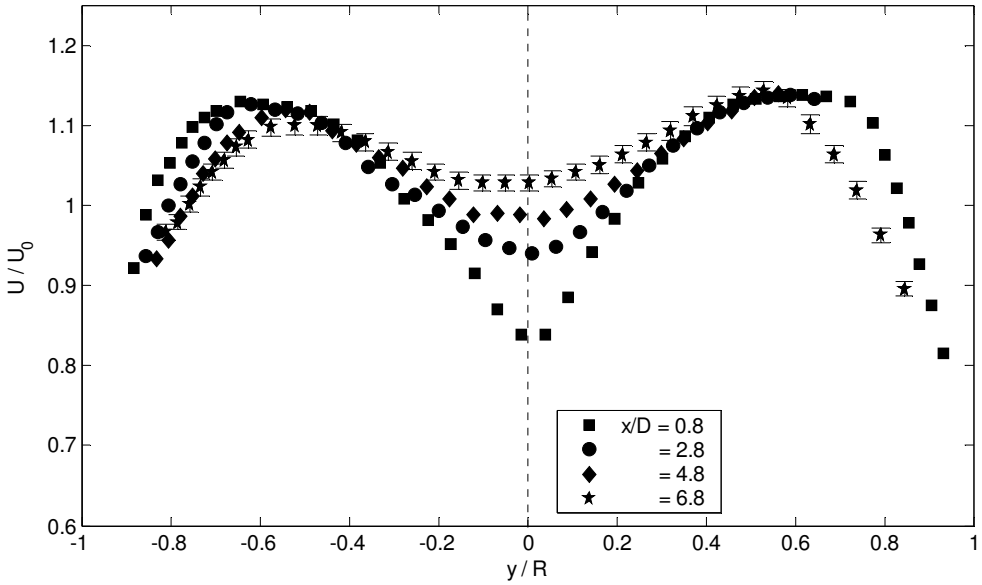

Figure III.7. Axial mean velocity profiles for Fin II.

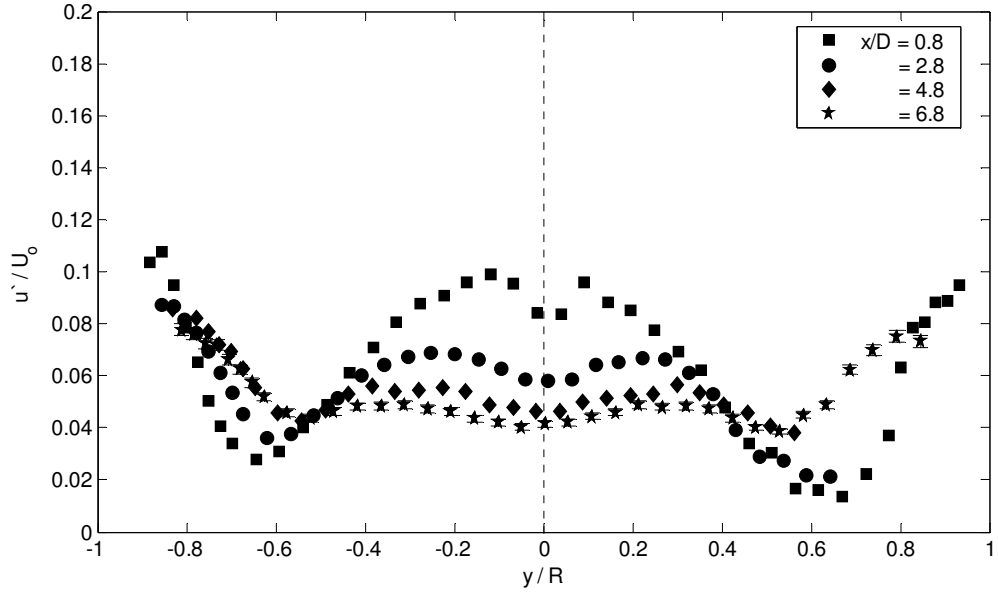

Figure III.8. Axial rms fluctuation velocity profiles for Fin II.

III.1.2 Twisted Single Fin

As explained earlier, swirl generator fin is based on the geometry of Fin IIIr. The wake downstream of this fin, which has a rounded leading edge, was much thinner (*i.e.*, had a smaller *y*-extent) at a given *x*-location than that downstream of a fin with a blunt leading edge but otherwise identical geometry (*i.e.* Fin III). A thinner wake meant that the interactions with the boundary layers on the pipe walls occurred farther downstream. This might suggest that, for a twisted fin with a similar base geometry, wake effects could be less significant. For this reason, Fin IIIr is selected to be the base geometry for the twisted fin. Both axial and azimuthal velocity measurements are carried out downstream of the single twisted fin. Fig. III.9. shows the axial mean velocity profiles at x/D = 0.8, 2.8, 4.8, 6.8, 8.8 and 10.8. At the first axial location, x/D = 0.8, a velocity defect, similar to the one with straight fins, exists. At the next measurement location, x/D = 2.8 this defect completely disappears due to the rapid mixing of the flow. There is little change in the mean velocity profiles, as the swirl is developing downstream, as seen at locations x/D = 2.8 through x/D = 10.8. Fig. III.9. shows the axial rms fluctuation profiles. Symmetry of the axial velocity fluctuation profiles are generally not retained except a central region, $-0.2 < y/R < 0.2$. It can be noted that, velocity fluctuations reach to a maximum of about 17 % of the bulk velocity. At the next axial location, x/D = 4.8, the fluctuations drop sharply; corresponding to the location where the velocity defect is essentially eliminated in the mean velocity profile. For $x/D \geq 4.8$, the rms fluctuations are essentially constant and range from 6–8%.

In Figs. III.11. and III.12, results of the LDV measurements of the azimuthal (tangential) velocity component downstream of the single twisted fin are shown. The

distinct characteristics of the swirl flow can be observed in these profiles. In Fig. III.11. azimuthal velocity profiles are depicted at 6 downstream locations, between x/D = 0.8 and x/D = 10.8. Mean velocities are normalized with the average velocity U_0. The magnitude of the azimuthal velocity is comparable to the axial mean velocities, as seen in the scale of Fig.III.11., which spans from V/U_0 = -1.0 to V/U_0 = 1.0. At x/D = 4.8, a counter rotating core is formed. In the other parts of the flow, the direction of the rotation is counter clockwise, while at this axial location, the core rotates clockwise. The counter rotating core, which spans $-0.4 \leq x/D \leq 0.4$, disappears in the next axial location (*i.e.* x/D = 6.8). A regular decay can not be observed in the axial distance covered in the experiments. The profiles show symmetry along the line $V/U_0 = y/R$. Fig.III.12 shows the rms values of the azimuthal velocity fluctuations (v') normalized by the average velocity. Results are given at the same downstream locations with Fig. III.1. At the first axial location fluctuations climb to 20% of the average velocity. Farther downstream, fluctuations decay to a level that is about 5% to 10 % of the average velocity ($8.8 \leq x/D \leq$ 10.8).

III.1.3. Four Twisted Fins

The 3D flowfield behind the assembly of four fixed fins is visualized using entrained air bubbles illuminated by a 60 W mercury-vapor arc light (wavelength: 340 - 380nm). Air trapped inside the pipes is the source of the air bubbles that essentially disappear in about five minutes after the pump is started. As seen in Figure III.15, four bubble pathlines come off the trailing edges of the fins; these spiraling pathlines intersect farther downstream, then dissipate near the pipe walls. As expected, the swirl generated by the

twisted fins greatly enhances mixing downstream of the fins (and presumably of fiber in the tube bank, improving fiber orientation isotropy).

Fig. III.14. shows the axial mean velocity profiles for the flow behind the four twisted fins for $0.8 \leq x/D \leq 10.8$. The flow is not obstructed while passing through the center of the Vortigen tube in between the fins (*cf.* Fig. II.7.). The consequence of this fact is evident in the mean velocity profiles just downstream of the Vortigen tube, at $x/D = 0.8$. Here, a significant velocity gradient is observed which stabilizes in the next axial location; the mean axial velocity increases to about 1.25 U_0 in the center of the Voritgen tube, *i.e.* $y/R = 0$. After $x/D = 4.8$, the mean axial velocity is almost constant over a region which spans from $y/R = -0.4$ to $y/R = 0.4$. Radial profiles of the axial rms fluctuations are depicted in Fig. III.15. The axial rms velocity fluctuations, which can be as high as 16% of the average velocity just downstream of the fin trailing edge, become nearly uniform at $x/D = 0.8$.

A number of interesting characteristics of the swirl flow can be observed in the azimuthal velocity profiles. In Fig. III.16., azimuthal velocity profiles are depicted at 6 downstream locations, between $x/D = 0.8$ and $x/D = 10.8$., which spans from $V/U_0 = -1.0$ to $V/U_0 = 1.0$. Unlike the results with the single twisted fin, the direction of the rotation does not change at any axial location (*i.e.*, the rotation is always clockwise). Like the case of the single twisted fin, the decay in V shows no clear trends with x, at least over the range of axial distances studied here. The profiles are symmetric about the line $V/U_0 = y/R$. The corresponding rms fluctuations in the azmuthal velocity are shown in Fig. III.17. The magnitude of the azimuthal fluctuations are comparable to the axial fluctuations (*cf.* Fig. III.15.), though it should be noted that there is considerable scatter in the profiles.

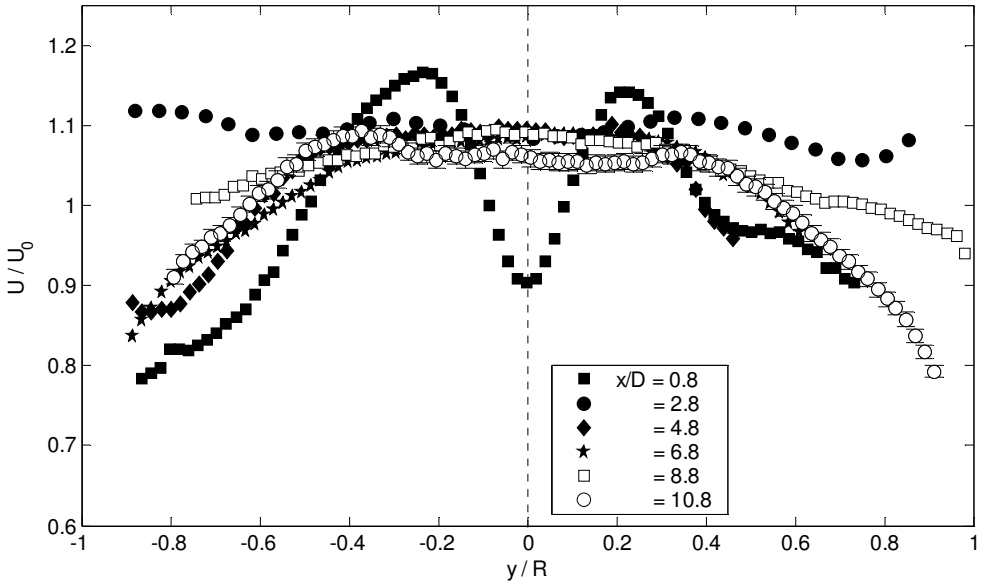

Figure III.9. Axial mean velocity profiles for the twisted single fin.

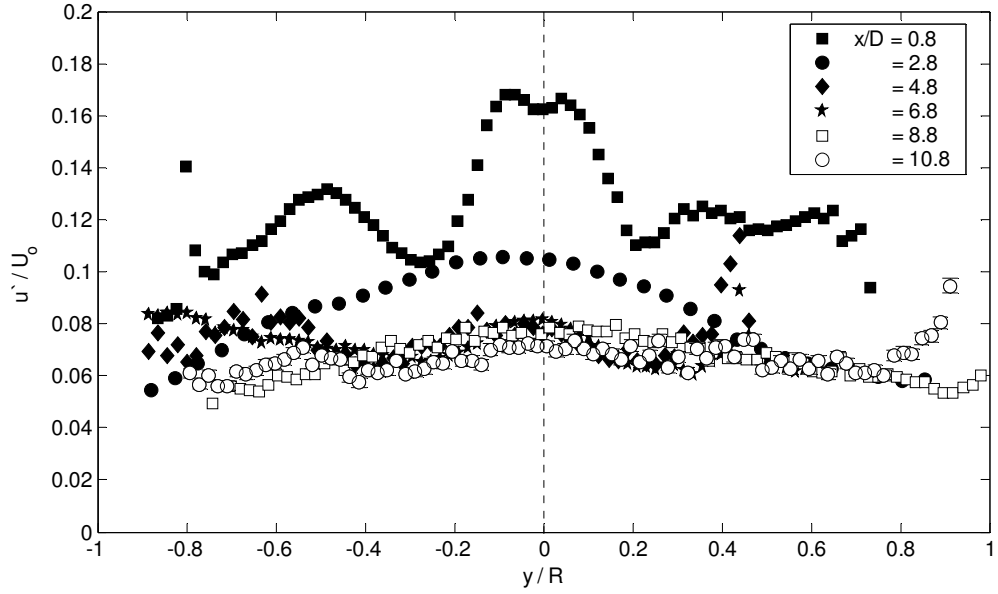

Figure III.10. Axial rms fluctuation profiles for the twisted single fin.

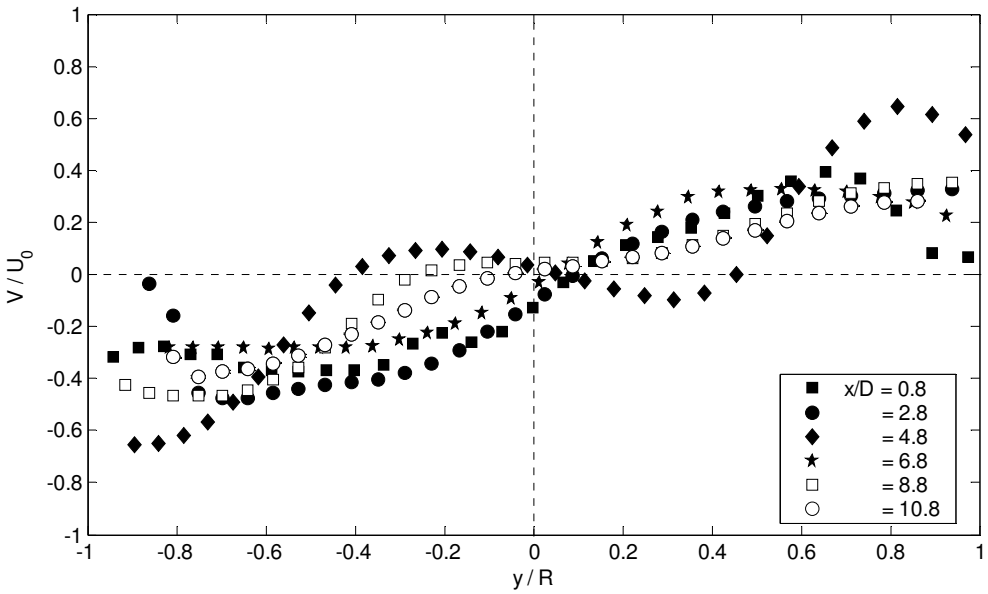

Figure III.11. Azimuthal mean velocity profiles for the twisted single fin.

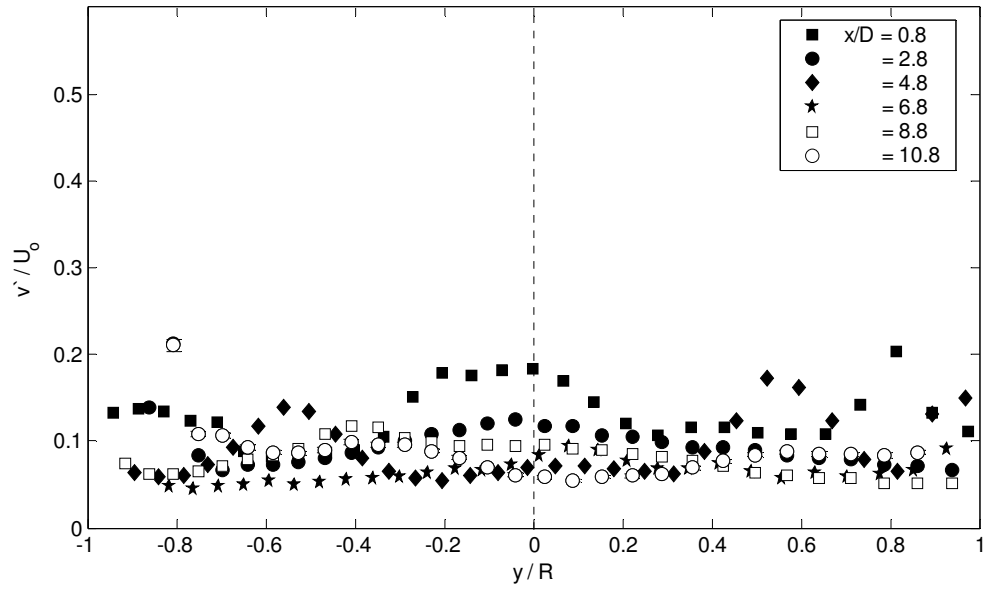

Figure III.12. Azimuthal rms fluctuation profiles for the twisted single fin.

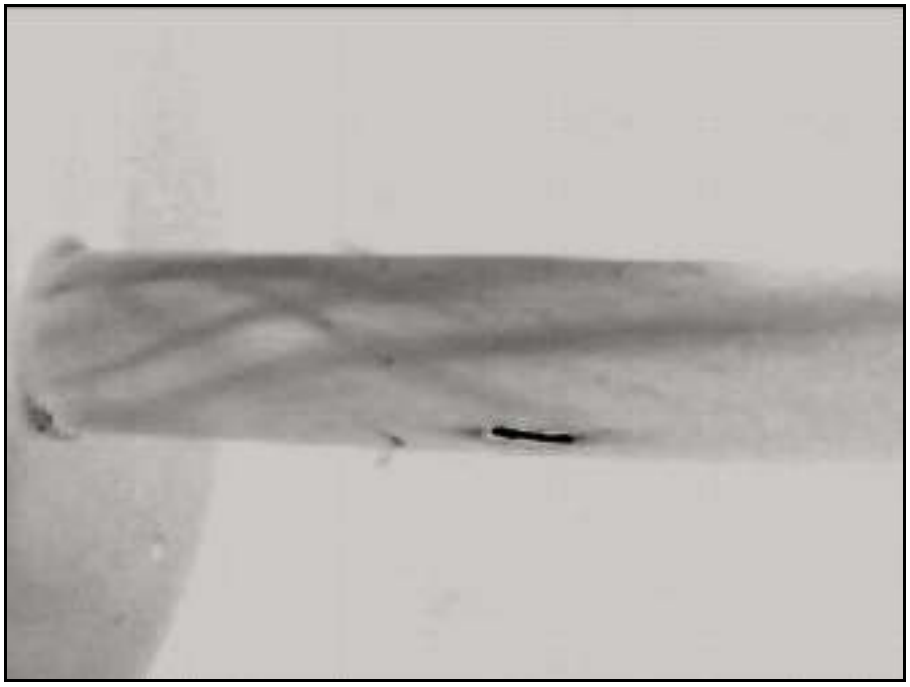

Figure III.13. Visualization of the flow downstream of the four twisted fins. This image spans 0.4 < *x/D* < 5.

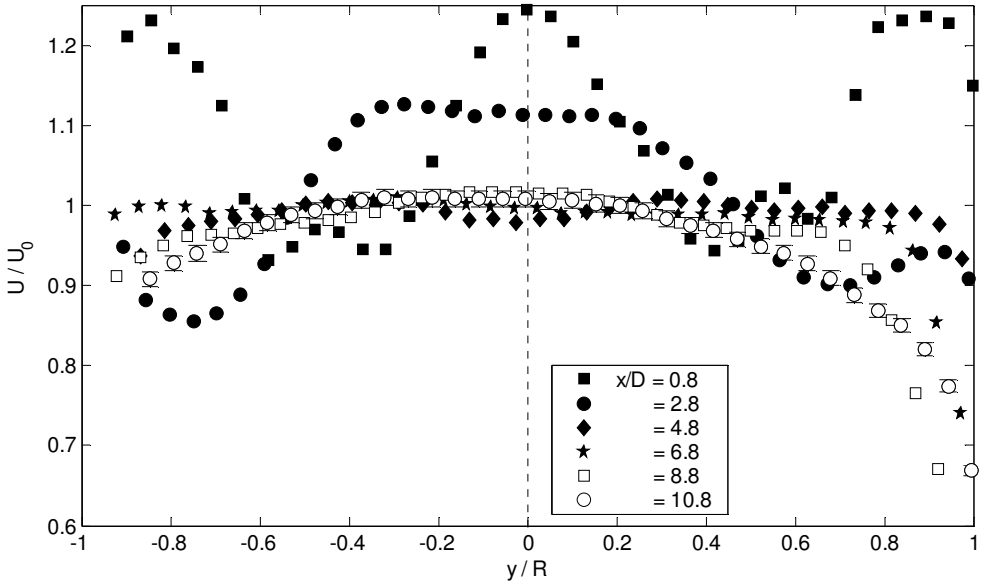

Figure III.14. Axial mean velocity profiles for the four twisted fins.

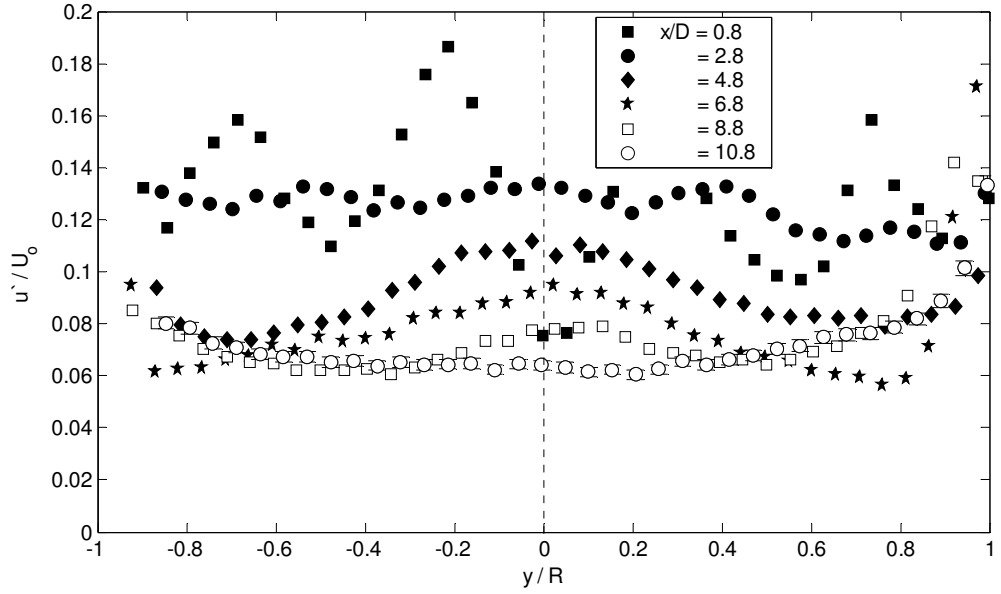

Figure III.15. Axial rms fluctuation profiles for the four twisted fins.

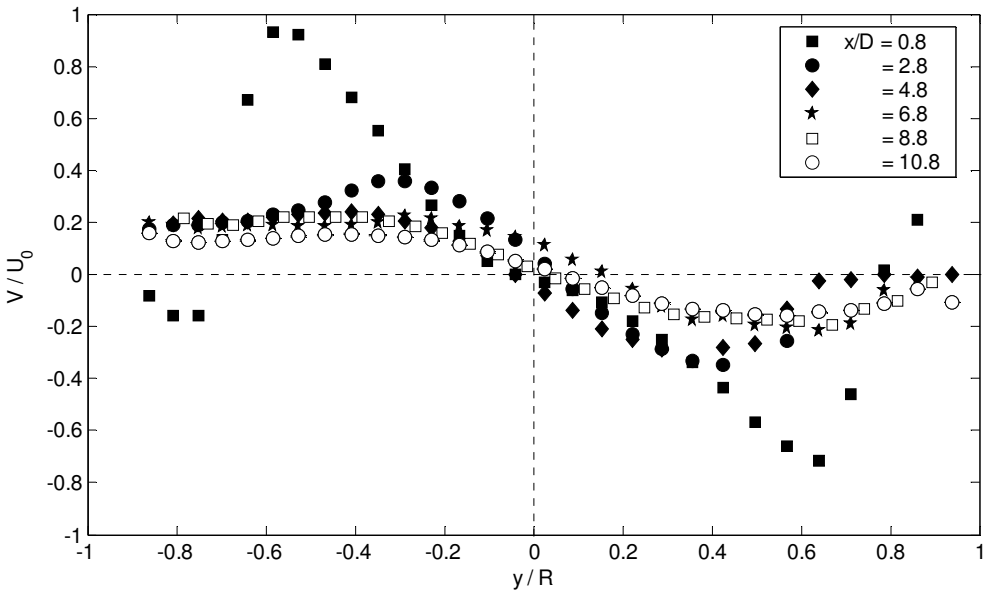

Figure III.16. Azimuthal mean velocity profiles for the four twisted fins.

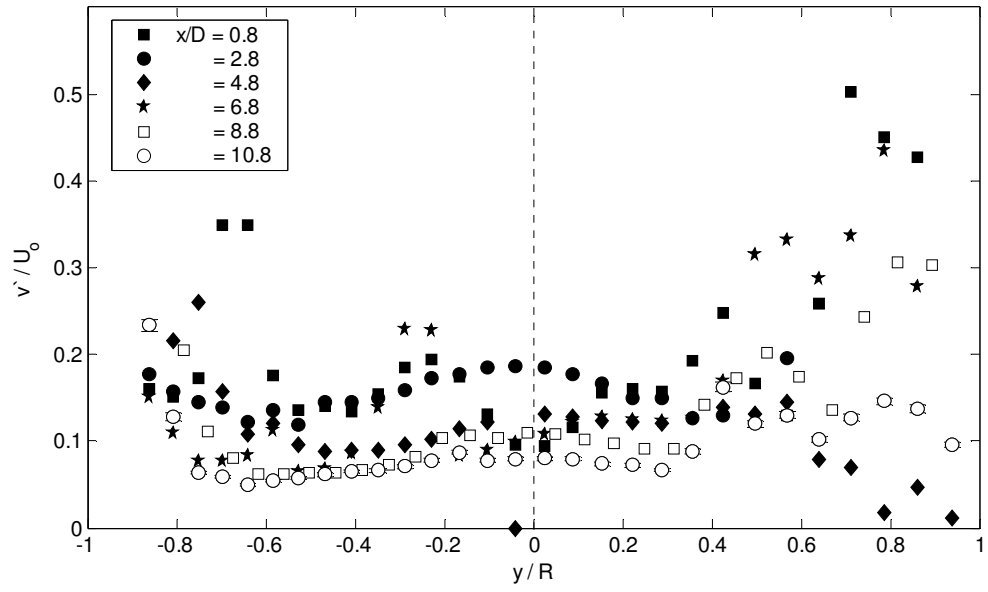

Figure III.17. Azimuthal rms fluctuation profiles for the four twisted fins.

III.2. Effects of the Fin Geometry

Three parameters describing straight fin geometry were studied here, namely the shape of the leading edge, the leading edge thickness and the trailing edge thickness, by comparing LDV results for the straight fin geometries Fin II, Fin IIr, Fin III, Fin IIIr and Fin IVr. Figs. III.18 and III.19 show axial mean velocity profiles and axial rms velocity fluctuations profiles, respectively, for all five straight fin geometries at the downstream location closest to the trailing edge, $x/D = 0.8$, where we expect the differences due to geometric variations in the fin to be most evident. Figs. III.20 and III.21 show the same profiles at $x/D = 4.8$

As explained in Chapter II, Fin III has a blunt leading edge, while Fin IIIr has a rounded leading edge; these fins have otherwise identical geometries. The shape of the leading edge affects the downstream development of the boundary layer over the surface of the fin. The wake downstream of a fin with a rounded leading edge was much thinner (*i.e.*, had a smaller y-extent) at a given x-location than that downstream of a fin with a blunt leading edge but otherwise identical geometry. A thinner wake also implies that the interactions with the boundary layers on the pipe walls occurrs farther downstream, as observed in Fig. III.18. and Fig. III.19. With Fin IIIr, mean velocity profiles have constant velocity regions indicating that these regions on the radial profile are not affected by the wake. In the rms fluctuation profiles, at the same radial locations regions of constant rms fluctuations can be observed with Fin IIIr. Farther downstream, the difference in the mean velocity profiles between the wakes of Fin III and Fin IIIr becomes smaller (Fig III.20.), although the axial turbulence intensities still differ between the two geometries (Fig. III.21.). At $y/R = 0$, u' is at a minimum with Fin III but u' attains

its maximum at the same location for the case of Fin IIIr. At both x/D = 0.8 and 4.8, Fin III has higher rms velocity fluctuations.

The effects of leading edge thickness are studied by comparing the development of the flow downstream of fins having different leading edge thicknesses but otherwise identical geometries, namely Fins IIr and IVr with leading edge thicknesses of 1.34 mm and 3.05 mm, respectively. A comparison of Figs. III.18. and III.19 shows that neither the mean velocity nor its rms fluctuations differ significantly at the axial location x/D = 0.8. Farther downstream, at x/D = 4.8, profiles of the mean velocity and its rms fluctuations are identical within experimental error, as seen in Figs. III.20. and III.21.

The impact of different trailing edge thicknesses are studied by comparing the development of the flow behind fins having different trailing edge thicknesses but otherwise identical geometries, namely Fins II and III, where III has a 50 % thicker leading edge than II. A comparison of the mean velocity profiles shown in Figs. III.18. and III.19 for these fins shows that the flow is not affected by the leading edge thickness. As expected, the profiles are identical within experimental error.

III.3. Self –Similarity of the Velocity Profiles

Axial mean velocity profiles in self-similar coordinates are given in Fig. III.22. for six downstream positions (x/D = 0.8 to 10.8) for Fin III. It can be seen that velocity profiles collapse on a single curve. As the boundary layers on the pipe walls develop, their interference with the wake increases. As a result of this, the portion of the radial axis where self-similiarity can be observed gets smaller with increasing x. At $x/D > 6.8$, the distortion in the self-similarity is more obvious. The experimental data for the straight fin

is in good agreement with Eq. I-8, suggesting that the wake is self-similar in terms of U for $x/D \leq 6.8$.

Figs. III.23. shows the mean profiles of the axial velocity downstream of Fin IIIr in self-similar coordinates. Overall it can be seen that profiles with Fin III are closer to self-similarity than the profiles with Fin IIIr. However, self-similarity appears to persist farther downstream for Fin IIIr; this may be due to the "thinner" wake associated with its rounded leading edge.

III.4. The Impact of Swirl

Swirl creates profound changes in the flow. A comparison of the flow behind the single twisted fin and Fin IIIr, which is essentially the straight fin geometry used to create the swirl generator fin will be helpful to examine the impact of swirl. In Fig. III.24. mean velocity profiles for Fin IIIr and the twisted fin are plotted for $x/D = 0.8$ and $x/D = 4.8$. Just downstream of the trailing edge, the velocity defect due to the presence of the vane is essentially identical for both cases, but the twisted fin case shows that the boundary layers on the pipe walls have already essentially eliminated most of the uniform freestream flow. Farther downstream (*i.e.* $x/D = 4.8$) the velocity defect has already dissipated, as seen in Fig. III.24, resulting in a more uniform velocity profile for the twisted fin. The straight fin case still has a noticeable defect and two symmetric peaks at $y/R = \pm 0.5$.

Fig. III.25. compares the velocity fluctuations for the straight and twisted vanes at an upstream and a downstream location. Note that the absolute values of the fluctuations are much higher for the twisted fin, at $x/D = 0.8$. As x increases, effects of the swirl on

rms fluctuations get weaker. As expected, the fluctuations increase in the boundary layer on the pipe walls for the straight fin. This is not observed for the twisted fin.

Swirl numbers which are calculated using Eq. I-9, are listed in Table III.1. for the twisted single fin and the four twisted fins at two downstream locations which are chosen at sufficient axial distance from the trailing edge so that the effects of the secondary flows are relatively unimportant. The integrals in the equation are calculated numerically using the axial and azimuthal mean velocity data. As stated before, there are regions close to the pipe walls which are not accessible for the LDV measurements. This creates an error in the calculation of the integrals in Eq. I-9. Nonetheless, these figures can still give an idea about the strength of the swirl. From Table III.1 it can be seen that swirl number for the single twisted fin is about two times higher than that of the four twisted fins at x/D = 6.8 and x/D =8.8.

Table III.3. S_f calculated at two downstream positions for the twisted single fin and the four twisted fins.

	x/D = 6.8	x/D = 8.8
Twisted Single Fin	0.19	0.16
Four Twisted Fins	0.095	0.083

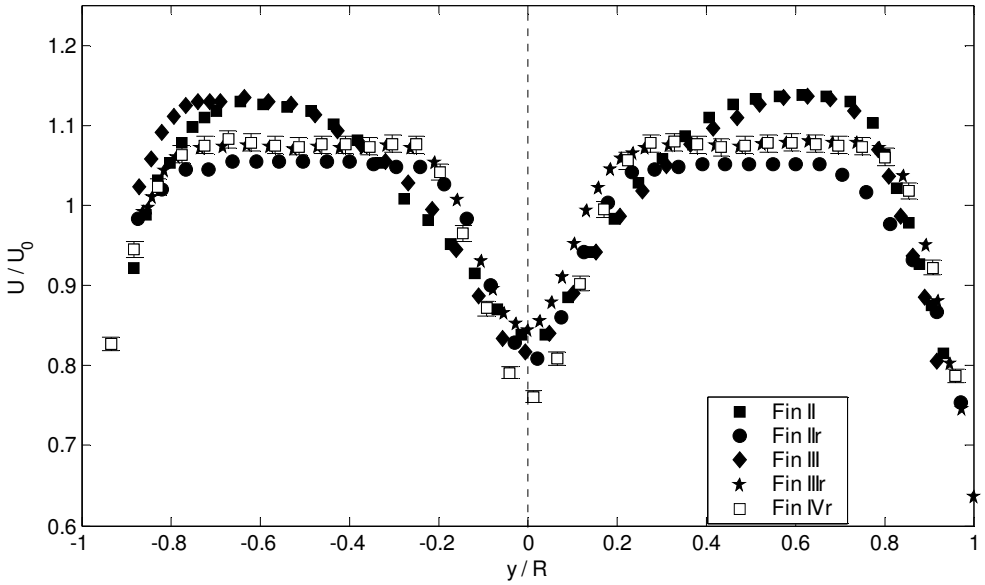

Figure III.18. Axial mean velocity profiles for five straight fins at *x/D* = 0.8.

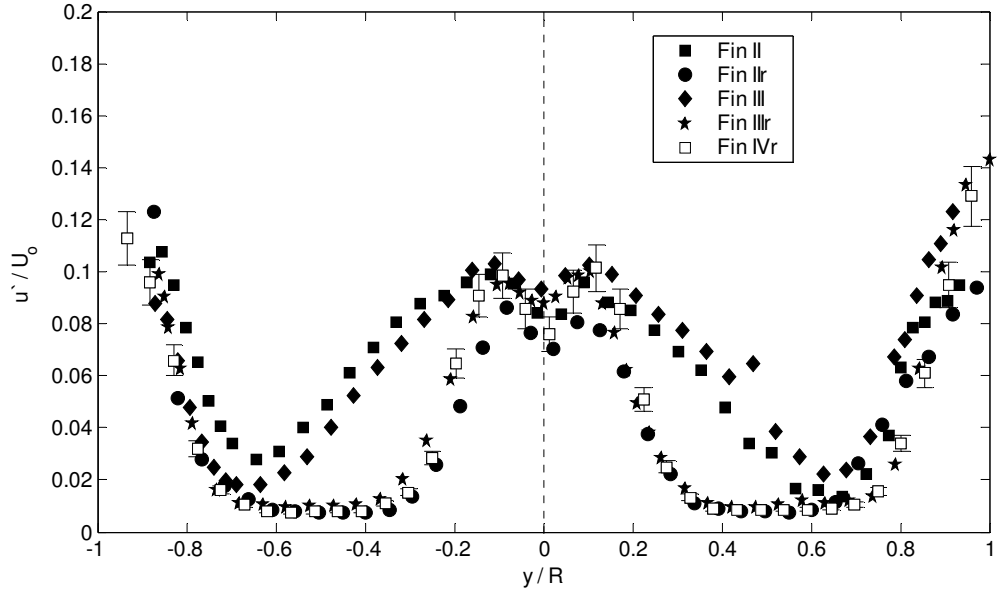

Figure III.19. Axial rms fluctuation profiles for five straight fins at *x/D* = 0.8 (Standard error: ± 9 %).

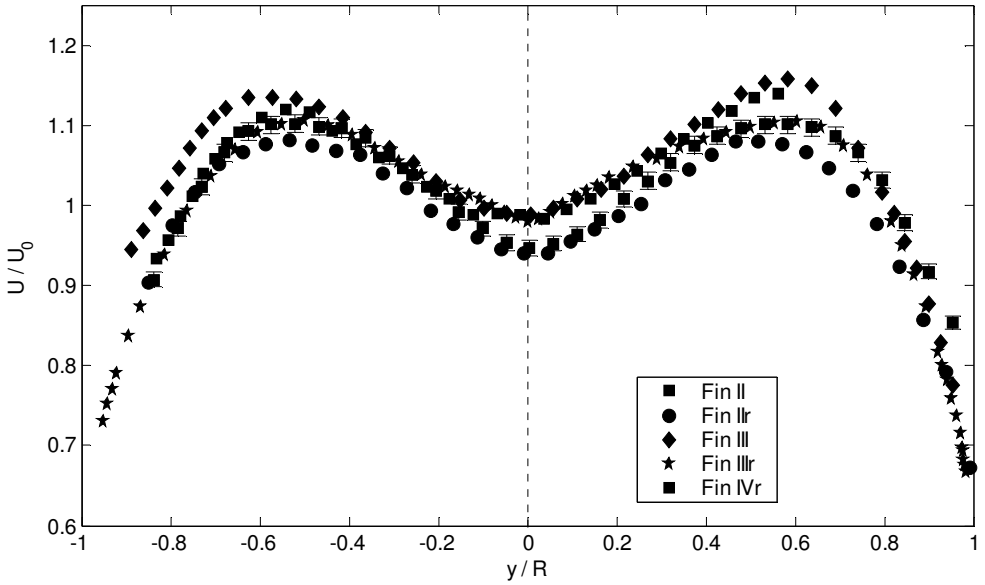

Figure III.20. Axial mean velocity profiles for five straight fins at *x/D* = 4.8.

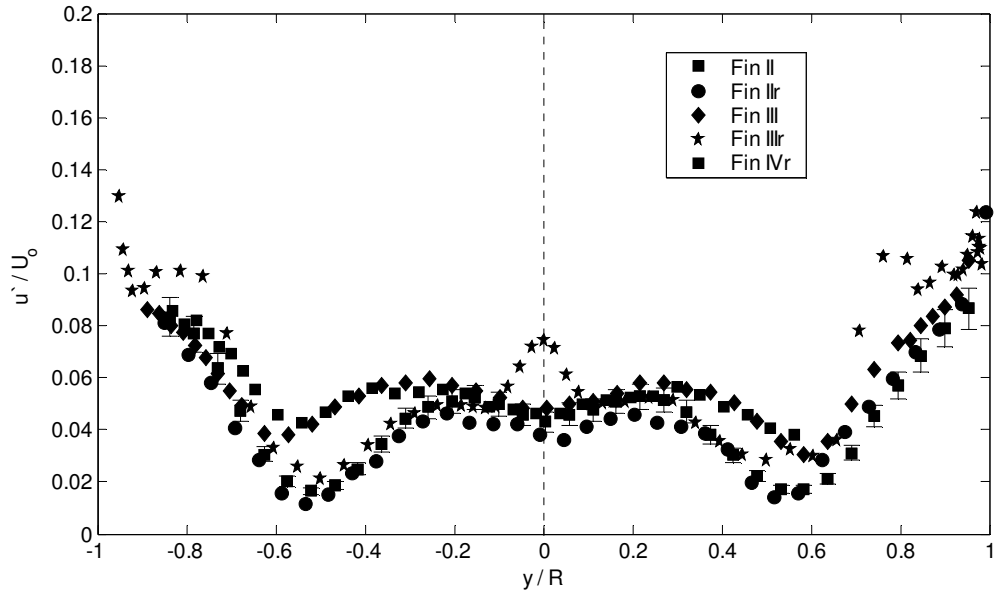

Figure III.21. Axial rms fluctuation profiles for five straight fins at *x/D* = 4.8 (Standard error: ± 9 %).

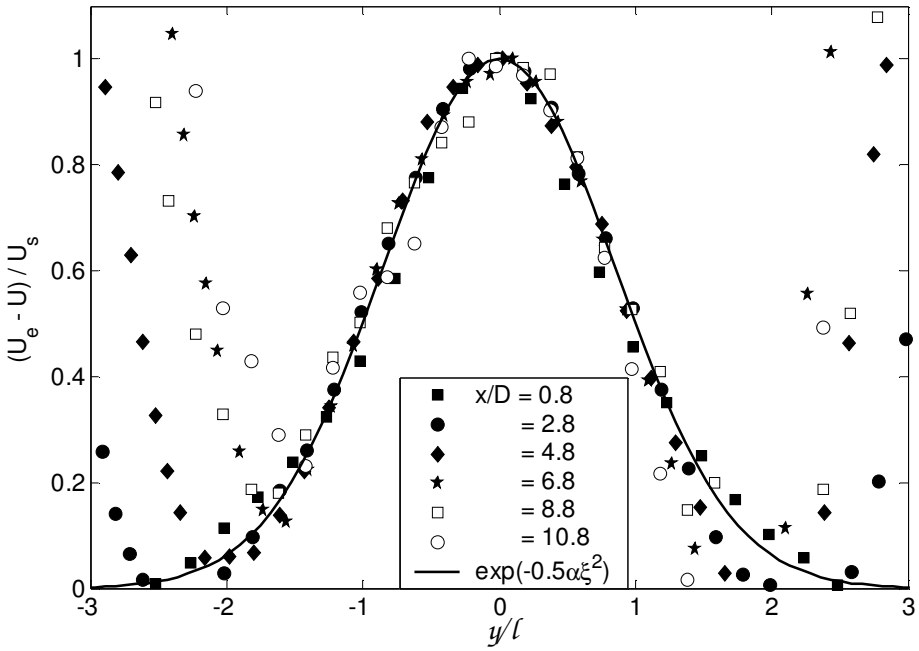

Figure III.22. Axial mean velocity profiles in self-similar coordinates for Fin III. Solid line is the analytical solution given in Eq. I-8 for the turbulent wake flow (plane).

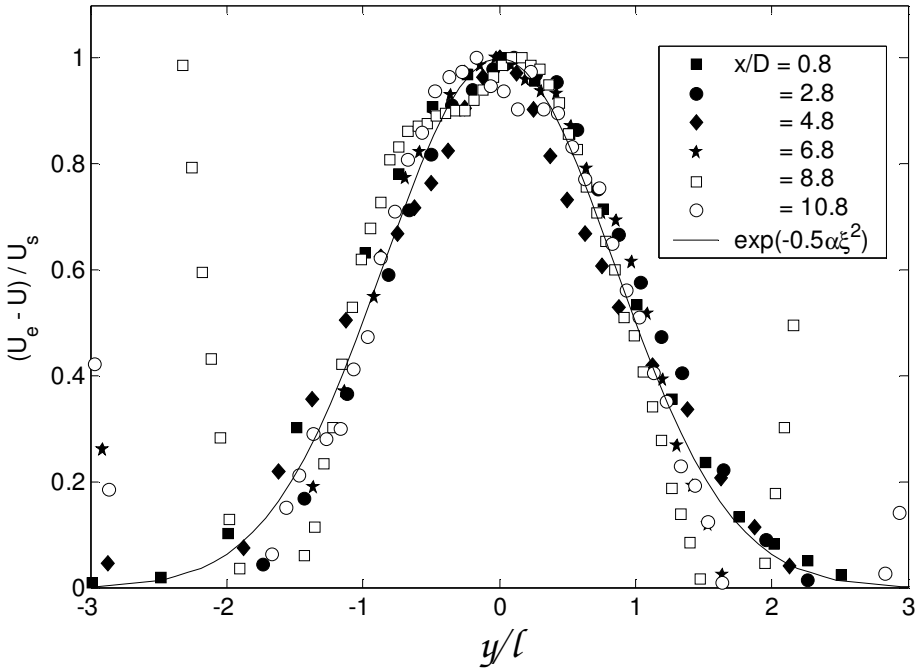

Figure III.23. Axial mean velocity profiles in self-similar coordinates for Fin IIIr. Solid line is the analytical solution given in Eq. I-8 for the turbulent wake flow (plane).

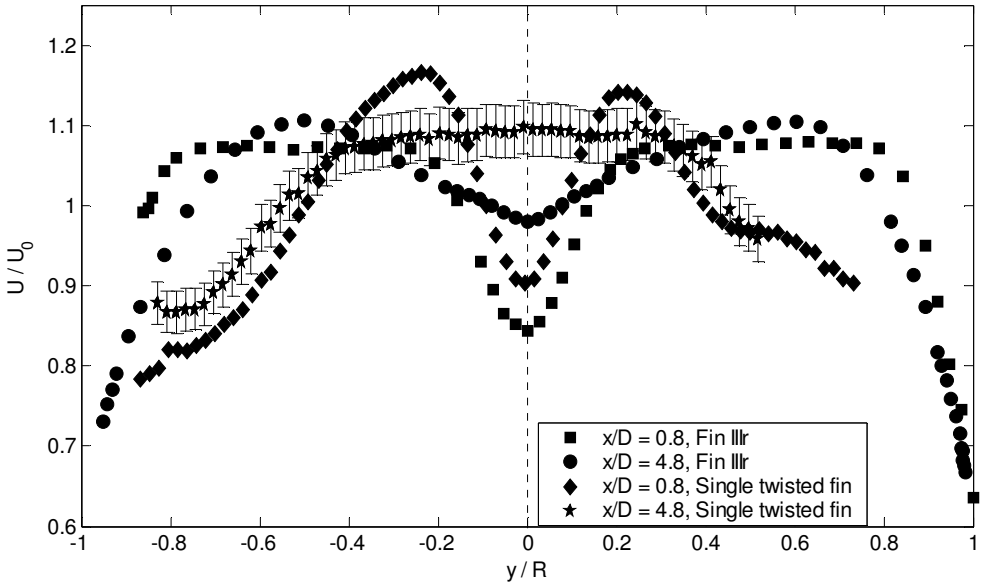

Figure III.24. Axial mean velocity profiles for Fin IIIr and the twisted single fin (Standard error: ± 3 %).

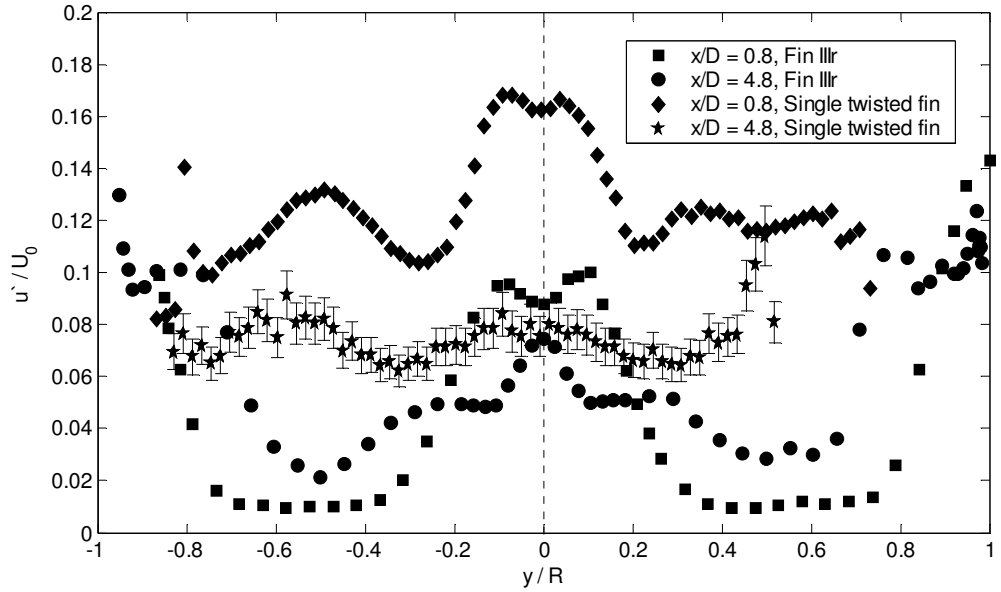

Figure III.25. Axial rms fluctuation profiles for Fin IIIr and the twisted single fin (Standard error: ± 10 %)

CHAPTER IV

CONCLUSIONS AND FUTURE WORK

IV.1. Conclusions

The aim of this thesis is to characterize the flow downstream of a tapered single fin with 0° and 180° twist and an assembly of four twisted fins. This study is motivated by the development of new active and passive flow control technologies for generating swirl in paper mill headboxes to improve fiber isotropy. Radial profiles of the mean and rms fluctuations of the streamwise and azimuthal velocity components downstream of the trailing edge of the fins were measured using two-component LDV at a Reynolds number based on the pipe diameter Re = 80,000. The fins were centered in a test section in a re-circulating water facility consisting of a glass pipe of inner diameter D = 25.4 mm; LDV data were obtained at distances downstream of the fin trailing edge $0.8 \leq x/D \leq 10.8$. The uncertainties in the mean velocity and rms fluctuation values estimated from experimental calibrations were ±1% and ±3%, respectively.

IV.1.1. Straight Single Fin

The wakes downstream of straight fins with tapered leading edges were studied to investigate self-similarity in the wake/velocity defect region and to evaluate the impact of the various leading and trailing edge geometries on the flow. Self-similarity based upon mean axial velocity component profiles persisted for the fin geometry Fin III for $0.8 \leq x/D \leq 6.8$. Self-similarity was not observed farther downstream, however, due to interactions between the fin wake and the boundary layers on the pipe walls.

In terms of trailing and leading edge geometries, comparison of fins with different trailing or leading edge thicknesses but otherwise identical geometries suggests that neither trailing nor leading edge thickness have a significant impact on the axial mean velocity component and its rms fluctuations. The shape (*vs.* thickness) of the leading edge, however, did have a significant impact. The wake downstream of a fin with a rounded leading edge was much thinner (*i.e.*, had a smaller y-extent) at a given x-location than that downstream of a fin with a blunt leading edge but otherwise identical geometry. A thinner wake also meant that the interactions with the boundary layers on the pipe walls occurred farther downstream. As a matter of fact, self-similarity appears to persist farther downstream for Fin IIIr which has a "thinner" wake associated with its rounded leading edge.

IV.1.2. Twisted Single Fin

The effect of swirl on the flow was studied using fins with a twist of 180° with a geometry that was otherwise identical to Fin IIIr. The swirl and secondary flows induced by the twisted-fin geometry significantly increased the axial and azimuthal velocity

fluctuations compared with those for the straight fin. Following previous studies, a forced vortex region, a free vortex region and a wall layer were identified based upon radial profiles of the mean azimuthal velocity component. The axial velocity component was always positive, and no reverse flow was observed. At a distance of 4.8*D* downstream of the trailing edge, the azimuthal mean velocity data suggest the existence of a counter-rotating vortex core with a radial extent of about 40% of the pipe diameter. The swirl intensity quantified by the swirl number was calculated as $S_f = 0.19$ at $x/D = 6.8$.

IV.1.3. Four Twisted Fins

Although the single-fin studies were valuable in calibrating and understanding how fin geometry and twist affect mixing and hence fiber isotropy, these geometries are not appropriate for implementation in an industrial headbox. A more robust "swirler" was therefore designed for online control of swirl flow. This design had four twisted vanes that will ultimately be fabricated from NiTi shape memory alloys with a two-way effect, where each fin will assume a twisted shape above the alloy austenite finish temperature to generate swirl and a straight shape below the alloy martensite finish temperature Transformation temperatures are typically between -200 and + 110 °C for NiTi alloys. These fins will therefore remain straight at typical headbox temperatures, and can then be actuated (*i.e.*, generate swirl) by using electrical current to heat the fins.

Because of difficulties in acquiring shape memory alloys with a two-way effect, studies were carried out of a model of the four-fin geometry in its twisted (*i.e.*, higher temperature) configuration. The LDV data demonstrate that swirl generated by this configuration is somehow weaker than the single twisted fin (quantified again by S_f=

0.095 at x/D = 6.8). Unlike the single twisted fin, however, no counter-rotating vortex core was observed downstream of the fins, and the mean azimuthal velocity component was consistently along the same anti-clockwise direction.

IV.2. Future Work

The first phase of this project entailed laboratory tests of "swirlers" for generating and controlling axial vorticity that can be implemented in the tube bank of an actual paper mill headbox using "smart materials". The next phase of this project will focus on pilot trials of this "Online Vortigen" concept and commercial implementation on a small hydraulic headbox. Before commercial implementation of the four-fin configuration and the Online Vortigen concept, however, the following issues will have to be evaluated:

- Are there materials issues associated with implementing the four-fin configuration using shape memory alloys with the two way effect (*cf.* Appendix A)?
- Are other shape memory alloy-based swirl generator designs superior in terms of swirl generation or materials compatibility for the Online Vortigen Concept?
- What are the flow issues associated with using these designs with multiphase fiber suspensions (*vs.* the single-phase water flows studied here)?

The next phase of this project will involve pilot machine implementation/trials of this Vortigen concept and commercial implementation on a small hydraulic headbox. Although the Vortigen technology is applicable to a wide range of paper products—from lightweight tissue to heavyweight grades—the initial commercialization effort will

emphasize the packaging industry since it is the largest segment of the American paper industry in terms of production volume.

REFERENCES

Absil L. H. J., Steenbergen W., Passchier D. M. (1990). "Time and spatial correlation measurements in the turbulent wake of a circular cylinder using Laser Doppler Anemometry", Applied Scientific Research, **47:** 247-271

Aidun C. K. (1997). "Hydrodynamics of Streaks on the Forming Table", TAPPI Journal, **80(8):** 155-162

Aidun C. K. (2001). "Headbox Retrofit Technology Shows Promise of Better Formation", AF&PA Hydrodynamics Program. Retrieved February 29, 2004, from http://www.paperloop.com/db_area/archive/extra/vortigen.shtml

Alber I. E. (1979). "Turbulent Wake of a Thin, Flat Plate", AIAA Journal., **18(9):** 1044-1051

Algifri A. H., Bhadwaj R. K., and Rao, Y. V. N. (1988). "Turbulence Measurements in Decaying Swirl Flow in a Pipe", Applied Scientific Research, **45:** 233-250

Andrepoulos J., Bradshaw P. (1980). "Measurement of interacting turbulent layers in the near wake of a flat plate", **100(3):** 639-668

Backshall R.G. and Landis F. (1969). "The Boundary-Layer Velocity Distribution in Turbulent Swirling Pipe Flow", Journal of Basic Engineering, 728-733

Baker D. W., Sayre Jr. C. L. (1974). "Decay of Swirling Turbulent Flow of Incompressible Fluids in Long Pipes" Flow: its measurement and control in science and industry. **1:** 301-12

Balachandar R., Tachie M. F. (2001). "A study of boundary layer-wake interaction in shallow open channel flows", Experiments in Fluids, **30:** 511-521

Boadway J. D. and Karahan E. (1979). "Correction of Laser Doppler Anemometer Readings for Refraction at Cylindrical Interfaces", DISA Information, **26:** 4-6

Chang F. and Dhir V. K. (1994). "Turbulent flow field in tangentially injected swirl flows in tubes", International Journal of Heat and Fluid Flow, **15(5):** 346-356

Chevray R. and Kovvasznay L. S. G. (1969). "Turbulence Measurement in the Wake of a thin Flat Plate", AIAA Journal, **7(8):** 1641-1643

Durst F, Muller R., Jovanovic, (1998). “Determination of the measuring position in laser-Doppler anemometry”, Experiments in Fluids, **6:** 105-110

Durst F., Melling A. and Whitelaw J. H., (1981). *Principles and Practice of Laser Doppler Anemometry*, Academic Press, London.

Farell C. and Youssef S. (1996). “Experiments on Turbulence Management Using Screens and Honeycombs”, Journal of Fluids Engineering, **118:** 26-32

Find for Windows Instruction Manual (1998). TSI Inc.

Glover J., Bullen P.R. and Cheesman D.J. (1985), “The effects of refraction on the measurement of velocity of water flow in a circular pipe using a three beam laser doppler anemometer system”, Proceedings of the Developments in Measurements and Instrumentation in Engineering, Durham, England, 59-72.

Goldstein R. J. (Editor), (1983). *Fluid Mechanics Measurements*, Hemisphere Publishing Corporation.

Gumievskii A.G. (1994). “Similarity and Decay Laws of Wakes with Zero Momentum and Angular Momentum”, Fluid Dynamics (English translation of Izvestiya Akademii Nauk SSSR, Mekhanika Zhidkosti i Gaza), **29(1):** 619-623

Gupte and Date (1989). “Friction and heat transfer characteristics of helical turbulent air flow in annuli”, Journal of Heat Transfer, **111(2):** 337-344

Haji-Haidari and Smith (1988). “Development of the turbulent near wake of a tapered thick flat plate”, Journal of Fluid Mechanics, **189:** 135-163

Hodgson D. E. (1988). *Using Shape Memory Alloys*, Report, Shape Memory Applications Inc.

Imao S., Itoh M. and Harada T. (1996). “Turbulent characteristics of the flow in an axially rotating pipe”, International Journal of Heat and Fluid Flow, **17:** 444-451

Kehoe A. B. (1984), *Flow Measurements by Laser Doppler Anemometry in a Nuclear Fuel Assembly*, PhD thesis, Georgia Institute of Technology, Atlanta.

Kehoe A. B. and Desai P. V. (1987), “Compensation for refractive-index variations in laser Doppler anemometry”, Applied Optics, **26(13):** 2582-2590

King M.K., Rothfus R. R. and Kermode R. I. (1969). “Static Pressure and Velocity Profiles in Swirling Incompressible Tube Flow”, AIChE Journal, **15(6):** 837-842

Kitoh O. (1991). “Experimental Study of Turbulent Swirling Flow in a Straight Pipe”, Journal of Fluid Mechanics, **225:** 445-479

Kobayashi T. and Yoda M. (1987). “Modified $k-\varepsilon$ Model for Turbulent Swirling Flow in a Straight Pipe”, JSME International Journal, **30(259):** 66-71

Kocherscheidt H., Schmidts M. and Ram V. I. V. (2002). “LDV Measurements of the Response of the Swirling Turbulent Flow in a Pipe to a Rapid Temporal Change in Swirl”, Flow Turbulence and Combustion **69:** 79-94

Koehler (2004), *Quantification of Initial Conditions in Turbulent Liquid Sheets using Laser-Doppler Velocimetry,* Master’s thesis, Georgia Institute of Technology, Atlanta.

Kreith F. and Sonju O.K. (1965). “The decay of Turbulent Swirl in a Pipe”, Journal of Fluid Mechanics, 2**2(2):** 257-271

Lasheras J.C. and Meiburg E. (1990). “Three-dimensional vorticity modes in the wake of a flat plate”, Physics of Fluids A, **2(3):** 371-380

Loiseleux T., Chomez J. M. and Huerre P. (1997). “The effect of swirl on jets and wakes: Linear instability of the Rankine vortex with axial flow”, Physics of Fluids, **10(5):** 1120-1134

Lowe M. L. and Kutt P. H. (1992). “Refraction through cylindrical tubes”, Experiments in Fluids, **13:** 315-320

Mattingly G. E., Criminale W. O. (1972). “The Stability of an incompressible two-dimensional wake”, Journal of Fluid Mechanics, **51(2):** 233-272

Nejad A.S., Vanka S.P., Favaloro S.C., Samimy M. and Langenfeld C. (1989). “ Applcation of Laser Velocimetry for Characterization of Confined Swirling Flow”, Journal of Engineering for Gas Turbines and Power, **111:** 36-45

Oertel H. Jr. (1990). “Wakes Behind Blunt Bodies”, Annual Review of Fluid Mechanics, **22:** 539-564

Otuska K. and Wayman C. M. (Editors), (1998). *Shape Memory Materials*, Cambridge University Press, Cambridge.

Padmanabhan N. (1984). "Swirling Flow of a Fluid in a Straight Tube", Indian Journal of Pure Applied Mathematics, **15(8):** 943-950

Pal S. (1985). "Freestream Turbulence Effects on Wake Properties of a Flat Plate at an Incidence", AIAA Journal, **23(12):** 1868-1871

Parchen R. R., Steenbergen W. (1998). "An Experimental and Numerical Study of Turbulent Swirling Pipe Flows", Journal of Fluids Engineering, **120:** 54-61

Park C. (2001). "Swirling Pipe Flows", Unpublished report, Institute of Paper Science and Technology.

Parsheh M. (2001). *Flow in Contractions with Application to Headboxes*, Doctoral Thesis, Royal Institute of Technology, Department of Mechanics, Faxen Laboratory, Stockholm.

Pope S. B. (2003). *Turbulent Flows,* Cambridge University Press, Cambridge.

Ramaprian B.R. and Patel V.C. (1982). "The Symmetric Turbulent Wake of a Flat Plate", AIAA Journal, **20(9)**: 1228-1235

Rocklage-Marliani G., Schmidts M. and Ram V.I.V. (2003), "Three-dimensional Laser-Doppler Velocimeter Measurements in Swirling Turbulent Pipe Flow", Flow Turbulence and Combustion, **70:** 43-67

Rusak Z., Whiting C.H. and Wang S. (1998). "Axisymmetric Breakdown of a Q-Vortex in a Pipe", AIAA Journal, **36:** 1848-1853

Sato H. and Kuriki K. (1961). "The mechanism of transition in the wake of a thin flat plate placed parallel to a uniform flow", Journal of Fluid Mechanics, **11:** 321-352

Selected Properties of NiTi-based Alloys, Memory-Metalle GmbH, Retrieved February 29, 2004, from http://www.memorymetalle.de/html/03_knowhow/PDF/MM_04_properties_e.pdf

Smook G. (2004). "Headbox Fundamentals", Retrieved October 25, 2004, from http://industrialexhange.com/tpmc/smook/v9_hb.htm

Steenbergen W. (1996). “Reduction of beam refraction in optical pipe flow experiments by use of sheet-fabricated pipe walls”, **22:** 165-173

Stockel D. (2000). “The Shape Memory Effect: Phenomenon, Alloys, Applications”, Report, NDC, Nitinol Devices and & Components, Inc., Fremont, CA.

Swean T. F. Jr. and Keramidas G. A. (1984). “The Turbulent Wake of a Flat Plate near a surface”, Proceedings of the Computational Methods and Experimental Measurements (2nd International Conference), **1:** 3-17

Tennekes H. and Lumley J. L. (1972). *A First Course in Turbulence*, MIT Press.

Timofeev A. S. (1982). “Peculiarities in Measuring the Velocity Vector using a Laser Anemometer in Flow Through Axisymmetric Models”, High Temperature (English translation of Teplofizika Vysokikh Temperatur), **20(5):** 951-957

Townsend (1956), *The Structure of Turbulent Shear Flow*, Cambridge University Press, Cambridge.

Ullmar M. and Norman B. (2004). “Observation of Fiber Orientation in a Headbox Nozzle at Low Consistency”, Report, Faxen Laboratory, Stockholm.

Velidandla V., Putta S and Roy R. P. (1994). “LDV Measurement of Turbulent Liquid Velocity Field in Channels with Curved Wall”, International Communications in Heat and Mass Transfer, **21(6):** 765-773

Wang X. and Nishi M. (1998). “Analysis of Swirling Flow with Spiral Vortex Core in a Pipe”, JSME International Journal B, **41(2):** 254-261

Weske D. R. and Sturov G.YE. (1974). “Experimental Study of Turbulent Swirled Flows in a Cylindrical Tube”, Fluid Mechanics, Soviet Research, **3(1):** 77-82

Williamson C. H. K. (1996). “Vortex dynamics in the cylinder wake”, Annual Reviews of Fluid Mechanics, **28:** 477-539.

Young A. D. and Rao K. N. (1978). “Some Low Speed Experimental Results on the Effects of Swirl and Velocity Distribution on an Axi-symmetric Jet”, Aeronautical Quarterly, **29(4):** 370-384

APPENDIX A

ONLINE CONTROL

A.1. Shape Memory Alloys

Certain materials can "remember" their initial (pre-deformed) shape and return to it after they are plastically deformed. This so-called "shape memory effect" (SME) is a material property, and the metallic alloys exhibiting this property are called "shape memory alloys" (SMAs). The SME, due to a reversible phase transformation affecting the crystalline form of the metal can be classified into two types:

1) the thermal shape memory effect, where the crystal structure changes with the application of heat; and

2) superelasticity, where the materials have a rubber-like behavior, returning to their initial shape after the load causing the deformation is removed. In superelasticity, strain levels can be as great as 10% (Stockel, 2000).

The SME was discovered by Chang and Read in an AuCd alloy in 1951 (Otuska and Wayman 1998). In 1963 another SMA, NiTi, was found by Buehler (Hodgson 1988). NiTi is still the most common shape memory material, although various alloys (*e.g.*, CuZnAl, CuAlNi, CuSn, FePt, FeMnSi) have subsequently been found to exhibit the shape memory effect.

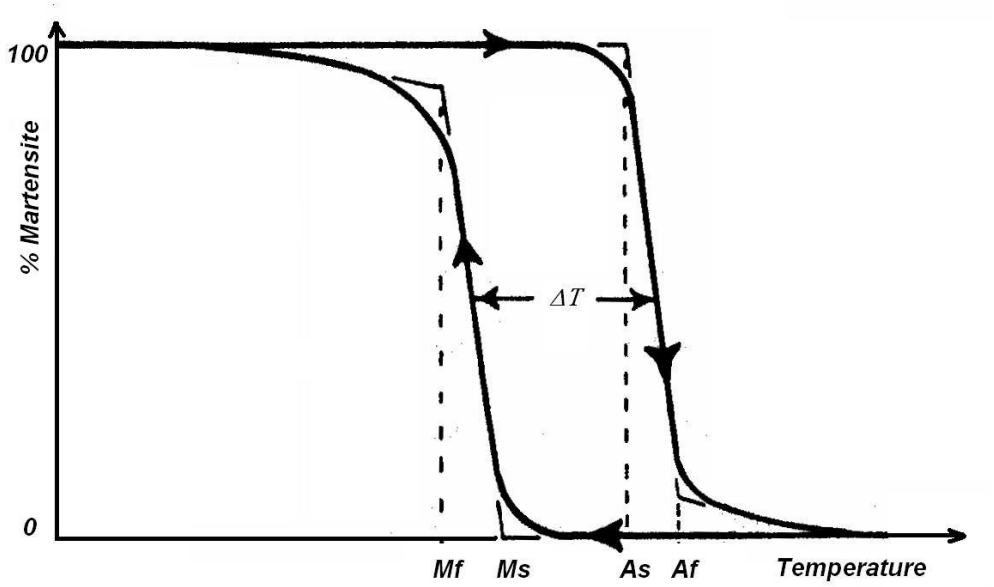

Figure A.1. Typical transformation curve for SMAs (heating and cooling). Vertical axis shows the amount of martensite in the structure. *ΔT* is the amount of hysteresis (After Hodgson, 1988).

Materials possessing the thermal SME (which will be referred to as the "shape memory effect" hereafter) have two distinct forms, martensitic and austenitic, in their crystal structure. In the martensitic phase, the material is soft and can be easily deformed (for NiTi, the martensitic modulus of elasticity, $\sigma_m \approx 30$ GPa). However, once the material transforms into its austentic phase, the stiffness of the material increases drastically ($\sigma_a \approx 75$ GPa for NiTi). The phase transformation is achieved by altering the temperature of the material. Fig. A.1. shows transformation curves for a typical SMA. Transformation between the martensitic and austenitic phases is hysteretic; in other words, at a given temperature, the material can have two different martensite to austenite compositions (or ratios), depending upon the last pure phase (*i.e.*, 100% martensite or austenite) that it experienced.

Table A.4 Selected thermal, physical and mechanical properties of NiTi shape memory alloys (Adapted from *Selected Properties of NiTi-based Alloys,* Memory-Metalle GmbH, 2004).

	Property		***Value***
1	Transformation temperature range		-200 to + 110 °C
2	Transformation strains	1 cycle	up to 8 %
		up to 100.000 cycles	up to 3 %
3	Thermal hysteresis		30 - 80 °C
4	Melting point		1310 °C
5	Density		6.45 kg/dm^3
6	Thermal conductivity	of the Martensite	9 W/m K
		of the Austensite	18 W/m K
7	Electrical resistivity		50-110 µ.cm
8	Young's modulus	of the Austenite	70 - 80 GPa
		of the Martensite	23 - 41 GPa
9	Ultimate tensile strength (fully annealed condition)		~ 900 MPa

In all cases, the SMA has its original shape in the austenite phase. As the temperature is decreased, martensite phase begins to form below the martensite start temperature, M_s, becoming 100% martensite when the temperature falls below the martensite finish temperature, M_f. In this phase, the material can be deformed to a shape different from its original configuration. The material can then be subsequently heated to return it to its original ("remembered") form. Upon heating, the austenite phase starts to form at the austenite start temperature (A_s) and the phase change is complete, with 100% of the metal in the austentite phase, above the austenite finish temperature (A_f). Once the material is pure austentite, it returns to its original shape no matter what its previous

"deformed" shape during the martensite phase. The temperature difference between the cooling and heating curves of a shape memory alloy determines the amount of thermal hystereis the material has. The transformation temperatures of various SMAs are mainly determined by the composition of the material. For a NiTi alloy, the transformation temperatures can be set between –200°C and 110°C. (Memory-Metalle GmbH), with a transformation hysteresis varying from 30°C to 80°C.

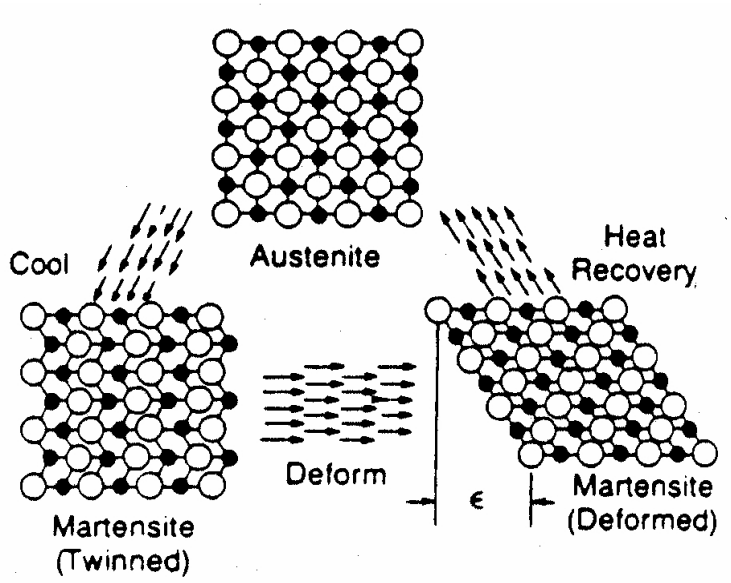

Figure A.2. Crystal structure of shape memory alloys in austenite and martensite ("twinned" and deformed) phases. ε is the amount of deformation (After Hodgson 1988).

NiTi alloys are the most commonly used SMAs because they have the most pronounced superelasticity with transformation strains up to 8% and because of their corrosion resistance, biocompatibility and superior engineering properties compared to

other types of SMAs (Stockel, 2000). Some properties of NiTi alloys are listed in Table A.1.

The mechanism of SME can be explained as follows. In the austenite phase, the SMA has an ordered cubic crystal form which can transform into a monoclinic martensite phase by cooling. At a certain temperature one of the two phases is more stable than the other. This causes the transformation to take place (Hodgson, 1988). In the transformation from austenite to martensite, bands, which are called “twins”, with alternating tilt directions are formed (Fig. A.2.). Traditional metals deform by means of atomic slip which damages the crystalline lattice and therefore deformation is not recoverable. In shape memory alloys, unlike traditional metals, deformation occurs with the tilting of the crystalline orientation rather than a dislocation motion. While returning to the austenite phase, (by heating) material having the martensite phase “remembers” its original shape because only with this shape the austenite structure can be maintained (Hodgson, 1988).

With the SME, only the high temperature (austenite) phase is remembered; this is referred to as the “one way shape memory effect” (OWSME). Shape memory alloys can however also be made to remember the shape of the low temperature (martensite) phase while retaining the memory of the austenite phase using the so-called “two way shape memory effect” (TWSME). The shape of a material having the TWSME can switch between two remembered configurations by changing the temperature. The origin of the TWSME is quite complicated, depending on dislocation arrays created in the martensite phase. Certain SMAs can be made to remember their shape in the martensite phase by a thermo-mechanical treatment called “training”. Otuska and Wayman (1998) describe four

types of training processes: introduction of plastic deformation, constraint aging, thermal cycling and utilization of precipitates. With thermal cycling, for example, a complete thermal cycle of the one way effect is repeated about 10–20 times while the material is physically constrained in its low temperature shape.

TWSME has some limitations compared with the OWSME. The cooling transformation force, which is responsible of the change in the material's phase from the austenite phase to the martensite phase, can be very low; meaning that the transformation form the austenite phase to the martensite phase will not happen instantly with the change in temperature. Another limitation is that the recoverable strains with the TWSME are lower compared to the OWSME. These limitations can be eliminated if the shape memory alloys with the OWSME is designed to show the two-way effect extrinsically rather than the "intrinsic" TWSME where a thermo-mechanical training is required. To achieve this, a spring can be coupled with the SMA. Upon cooling, in the martensite phase, the spring can force the material to have the desired low temperature shape as the material is relatively soft. When the SMA is heated, it will become much stiffer and assume its high temperature shape pulling the spring along.

Although SME has been proposed as "the solution" to many engineering problems since its discovery, commercially successful applications are not abundant. Material cost is an important disadvantage of shape memory materials. Moreover, there are competing technologies like bi-metals. Generally, SMAs are used as sensors and actuators, valves; in triggering mechanisms and in medical applications.

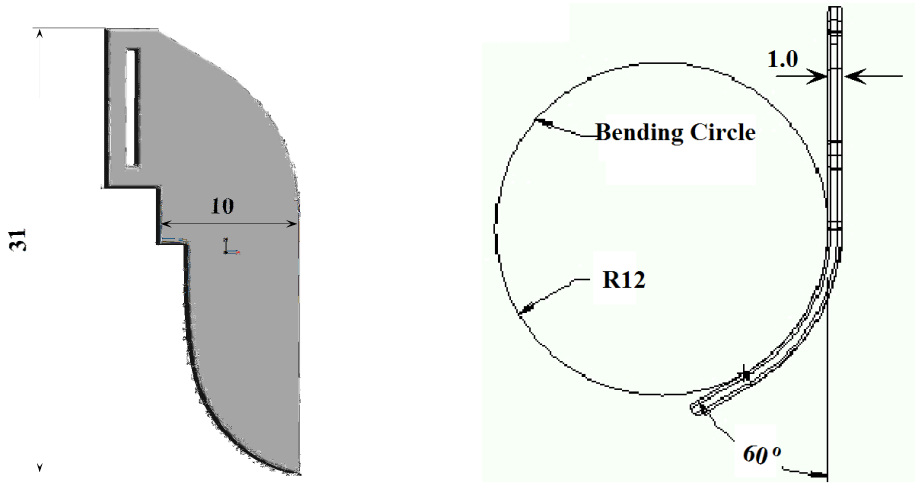

Figure A.3. CAD drawings (*Pro-E*) of one of the SMA fins when it is straight (left) and when it twists by 60^o (right). Dimensions are in mm.

Figure A.4. Photograph of the assembly of four SMA vanes in the Vortigen tube in their swirl generating configuration (austenite phase). Direction of the flow is out of the paper.

A.2. Application of the Shape Memory Alloys with the Vortigen Technology

A robust system has been designed for pilot trials and final commercial implementation for the on line actuation of the Vortigen system in the forming section of a paper machine. The current design has four twisted vanes which have a thickness of 1.0 mm and are spaced evenly around the circumference of the Vortigen tube. Each of the vanes, when fabricated from a NiTi SMA with the TWSME, should bend about 60° (Fig. A.3.) when heated above their austenite finish temperature, A_f, to the relatively stiff austentite phase and return to an untwisted, or straight, configuration at temperatures below martensite finish temperature, M_f, in their relatively soft martensite phase in this application. Fig. A.4. shows a photograph of an assembly of four SMA fins in their austentite geometry in the Vortigen tube.

The current Vortigen design has SMA fins with the OWSME. The fins easily assume their "twisted" configuration when heated above their transition temperatures. Returning the SMA fins to their straight configuration below this temperature, however, requires an external restoring force. In the actual industrial application, using springs to impose this external restoring, or "bias", force is impractical because the springs will affect the flow and probably cause fiber flocculation. Employing springs outside the individual tubes in the tube bank is also difficult because of space limitations, with less than 1 cm gap between adjacent tubes in the tube bank.

One solution to this problem is to use shape memory alloys with the TWSME; we are currently working with a company, *Nimesis*, to fabricate fins with this capability. It may also be possible to exploit the inherent hydrodynamic force generated by the flow to restore the "twisted" fins (after heating) to their original straight configuration. This

would most likely require much thinner fins; crude initial estimates suggest that the fins should be about 150 μm thick—such thin fins may of course be too fragile for industrial use.

In this study, it has been shown that four SMA vanes in their heated configuration or geometry generate the axial vorticity levels required for microforming. To maintain their twisted shape, the temperature of the SMA vanes should be higher than their transformation temperature. As the SMA fins will be continually cooled by the fiber suspension flow, which is at about 50°C, in the tubes, they should be heated constantly—by a current to generate Joule heating, for example—to keep them in their swirl-generating martensitic shapes. Initial estimates suggest that the power required to maintain a single Ni-Ti alloy fin above its transformation temperature will be 120 W assuming that a 30°C temperature difference between the transformation temperature of the SMA and the mean temperature of the flow.

APPENDIX B

EXPERIMENTAL UNCERTAINITY AND SOURCES OF ERROR

B.1. Sources of Error

Errors in the experimental results can be attributed to a wide variety of factors, which can be classified into four groups: 1) errors due to factors upstream of the fin (referred to as "upstream errors"; 2) errors due to factors downstream of the fin ("downstream errors"); 3) errors in fin alignment ("alignment errors"), and 4) errors due to variations in LDV sampling ("sampling errors").

The first three types of errors are dominated by misalignments in the various components in the flow loop and the experimental apparatus. "Upstream error" is essentially the experimental error due to the misalignment of the flow loop components upstream of the Vortigen tube, namely the nozzle and the calming section components (*i.e.*, the coarse and fine screens and the honeycomb). Such errors can be quantified by the intensity of the free stream turbulence and the uniformity of the mean flow. LDV measurements were therefore carried out just downstream of the *empty* Vortigen tube (*i.e.* without a swirler or a fin) at $x/D = 0.8$. Figs. A.5 and A.6 show the axial mean velocity and the axial turbulence intensity, defined as:

$$TI_x = u' / U \tag{A-1}$$

respectively. These Figures show that the axial turbulence intensity is uniform and about 0.9% and that U is also uniform over the central 80% of the pipe, or $|y/R| \leq 0.8$. However, it should be noted that this evaluation of the upstream error is not completely independent of the downstream error, since the alignment of the test section with respect to the probe head could also significantly affect these results.

The second group of experimental errors, the "downstream error", includes the errors due to the alignment of the test section (and the experimental location) with respect to the laser probe head. These errors are explained in Chapter II.

The third group of errors are due to slight misalignment of the fin from the vertical inside the Vortigen tube. In all cases, the velocity profiles are measured for the case where the leading edge of the straight and the twisted single fin are vertical, *i.e.*, normal to the horizontal pipe axis. For the prototype of the next generation Vortigen concept, the fins should be symmetric about the y- and z-axes. It is very difficult, practically speaking, to distinguish among these three types of errors; the combined effect of these error sources, which is assumed to be the overall uncertainty in the LDV measurement, is however examined in Sec. B.3.

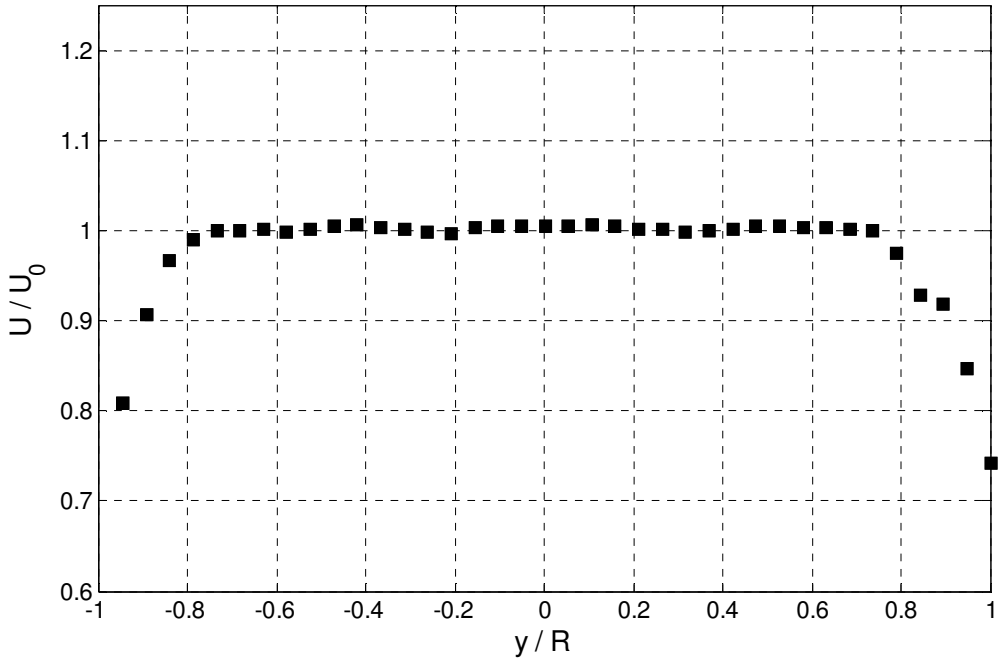

Figure A.5. Axial mean velocity profile downstream of the "empty" Vortigen tube at *x/D* = 0.8.

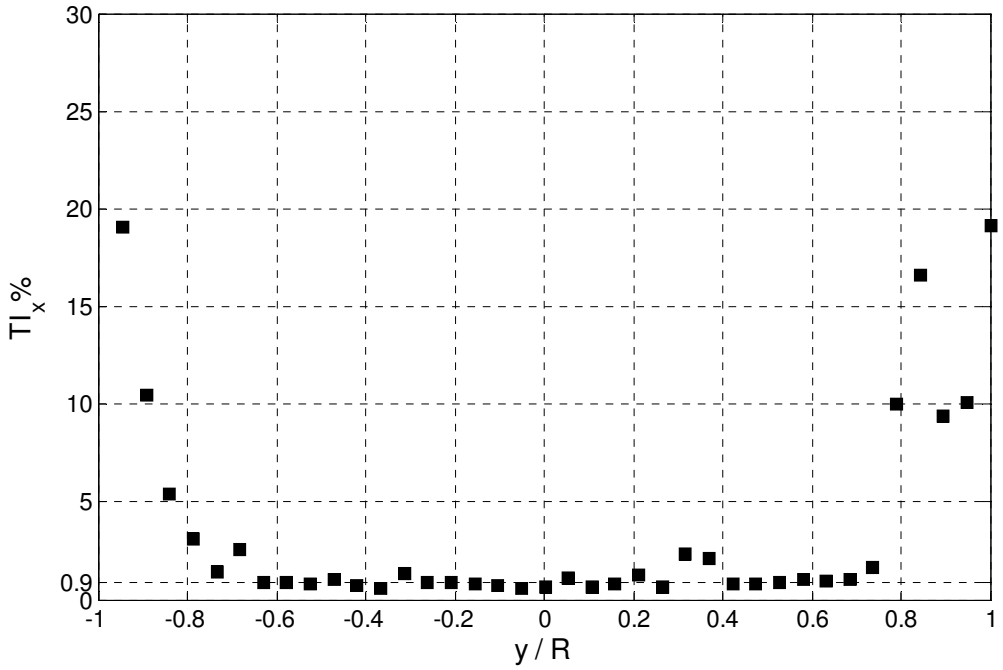

Figure A.6. Axial turbulence intensity profile downstream of the "empty" Vortigen tube at *x/D* = 0.8.

The last group of errors are the so-called "sampling errors," due to the LDV system and its operation. The most important of these errors, is due to the finite number of instantaneous velocity measurements (or the number of samples) at each location used to calculate the mean velocity and the turbulence intensity. The dependence of the mean velocity and rms velocity fluctuations on the number of samples is discussed in the next section.

The variation in the results presented in this Appendix and in Chapter III is expressed in terms of standard error (SE) which is given by

$$SE = t_{N-1} \frac{\sigma}{\sqrt{N}} \tag{A-2}$$

where N is the number of samples (or tests), t_{N-1} is the t value obtained from the t table for N-1 degrees of freedom and σ is the standard deviation. The level of confidence is selected to be 90% or 95%.

B.2. Sample Number Dependence

The number of velocity measurements taken at each measurement point has an effect on the velocity statistics (*i.e.*, the mean velocity and its rms fluctuation). To examine the dependence of the velocity measurements to the number of samples, *i.e.* instantaneous velocity measurements, tests were performed downstream of the twisted single fin with different number of samples under the same experimental condition at the same (x,y,z) location of (0.8D, 0, 0). The sampling rate varied from 250 to 400 Hz during these tests, which were carried out for 10, 100, 200, 500, 1000, 2000, 5000 and 10000 samples, with

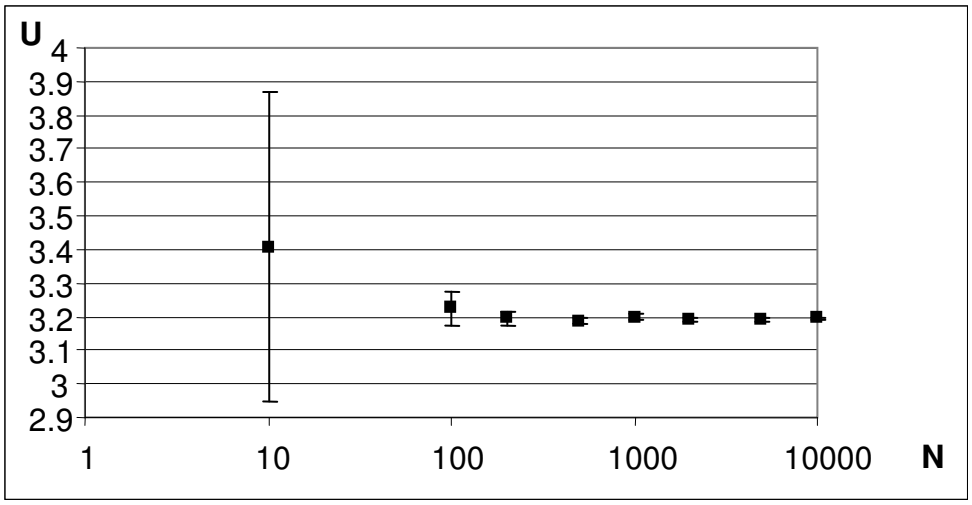

Figure A.7. Convergence of the the axial mean velocity, *U*, with the number of samples, *N*, in a semi-log scale.

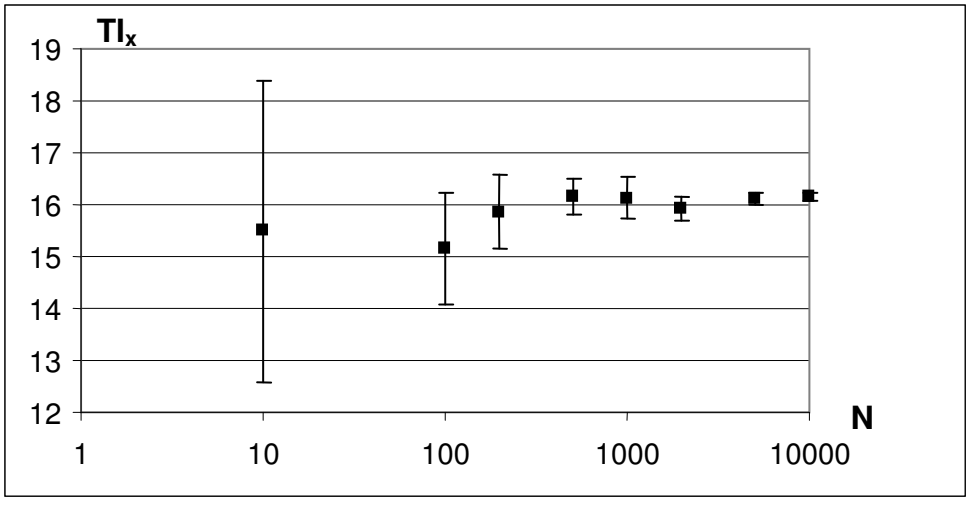

Figure A.8. Convergence of the axial turbulence intensity, TI_x, with the number of samples, *N*, in a semi-log scale.

each test at a given number of samples repeated 10 times. Fig. A.7. depicts the variation in the axial mean velocity with the number of samples, N. The error bars represent 95% confidence levels about the mean value. As expected, the variation in the mean velocity decreases as N increases, and the mean velocity appears to converge to 3.20 m/s for $N \geq 200$. Fig. A.8 shows the axial turbulence intensity; again, variations in TI_x decrease as N increases, although the convergence is slower for the fluctuations than for the mean, as expected. The axial turbulence intensity converges to 16.2% for $N \geq 1000$. We can therefore conclude that an increase in the number of samples above 1000 does not significantly improve the accuracy of the results. The lower limit for the number of measurements at each location was therefore set at 1000, with N varying between 1000 and 10000 in the actual experiments. For $N = 1000$, the standard sampling errors are 0.32% and 2.52% in the mean velocity and the turbulence intensity, respectively.

Based on the convective time scale-based arguments given in Chapter II, the total sampling time should be at least 10 s. Although the sampling time on the tests presented in this section varied, in all cases, the sampling time was less than 10 s for $N < 5000$. The variations in the mean velocity and the turbulence intensity for $N \leq 2000$ could therefore also be due to inadequate sampling time as well too few samples.

B.3. Overall Uncertainty in the LDV Measurements

An initial estimate of the accuracy of the mean velocity measurements was obtained by comparing the average velocity calculated using the integral of the axial velocity profiles and the average velocity calculated using the measured flowrate. The average axial velocity was calculated for all the straight fins at all axial locations measured. In these

calculations, the no-slip boundary condition was applied at $y/R = \pm 1$ and the axial mean flow is assumed to be axisymmetric. The results of these calculations were compared with the mean velocity obtained from the measured flowrate ($U_o = 3.09$ m/s). The average discrepancy between these two estimates of the mean velocity is 2.95% (± 0.93%). It should be noted, however, that the lack of data near the wall contributes to this error.

Two other tests were therefore performed to quantify the overall uncertainty in the mean velocity and its rms fluctuation. For the first test, a set of LDV measurements were obtained in the wake downstream of Fin IIIr at $x/D = 4.8$. After the initial set of measurements, the recirculation pump was stopped; the pump was then restarted and the measurements were repeated at the same axial location. The alignment of the probe head, the flow loop components and the fin remain identical between these two tests. Fig A.9. shows the average of the two measured axial mean velocity profiles and Fig. A.10. shows the average of the corresponding rms fluctuating velocity component. The standard error for the mean and the rms fluctuation velocities are at about 1% and 3% respectively; note that these are estimates over the entire radial span of the pipe. This standard error, shown by the error bars on the figures, was calculated by comparing the two sets of profiles and evaluated at 90% confidence level.

These errors are typical of LDV measurements between different experimental runs where the alignment of the system remains unchanged. In all cases, the velocity profiles measured for a given single wake or swirl generator geometry were obtained without changing alignment. The standard errors on the velocity profiles presented in Chapter III for a single geometry are therefore given as 1% for the mean velocity and 3% for the rms fluctuation velocity.

Table A.5. Standard error (SE) in the axial and azimuthal velocity measurements for the straight and twisted fins based on fully independent tests.

	Test case	***Velocity component***	***S.E. in the mean.***	***S.E. in rms fluctuation***
Straight fins	Fin IIIr, $x/D = 4.8$	U	1%	9%
Twisted fins	Single twisted fin, $x/D = 4.8$	U	3%	10%
	Single twisted fin, $x/D = 8.8$	V	7%	14%

When a new fin geometry is installed, however, every component in the setup is realigned. To evaluate the error associated with realignment, the overall uncertainty was estimated by comparing fully independent velocity measurements. Three different cases were considered: the axial velocity component downstream of the straight fin, and the axial and azimuthal velocity components in the wake of the single twisted fin. For each case, measurements are repeated three times, (*i.e.*, three mean velocity and three rms fluctuation profiles are obtained at a given axial location). Before each measurement, the components of the flow loop are disassembled, reassembled and realigned. The probe head is repositioned and the system components (including the fins) are realigned. These measurements should therefore be completely independent. The standard errors for each case are calculated by comparing three profiles for the mean velocities and the rms velocity fluctuations. The results of the tests are given in Table A.2. It can be seen that the standard errors (except the standard error in the mean for the test case with Fin IIIr)

are significantly higher than the 1% and 3% obtained from the first test, which did not involve any system realignment. The main source of error in the measurements therefore appears to be misalignment of the flow loop components and the probe head. The Figures presented in Chapter III (Figs. III.18, 19, 20, 21, 24 and 25) that compare results from different swirl or wake generators are therefore plotted with error bars in corresponding to the standard errors from this Table.

Figs. A.11. through A.16 show the results of the tests for the mean and rms velocity components. Each profile is the average of three independent measurements. Not surprisingly, the errors tend to increase close to the pipe walls (*i.e.* $y/R \rightarrow \pm 1$) in most cases.

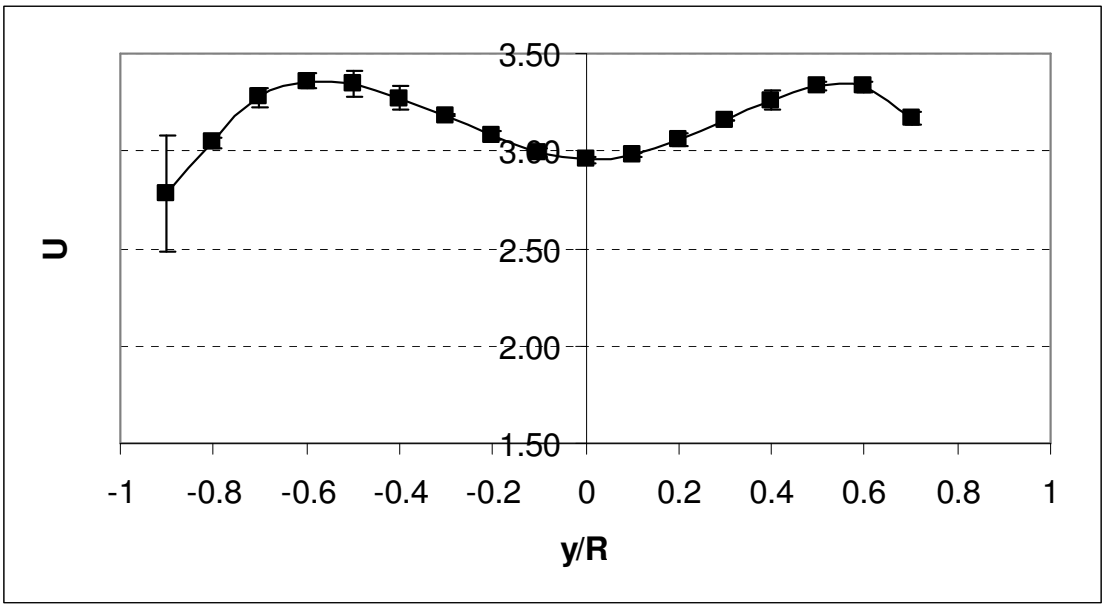

Figure A.9. Axial mean velocity profile for Fin IIIr at *x/D* = 4.8. Results are the average of two tests with the same alignment.

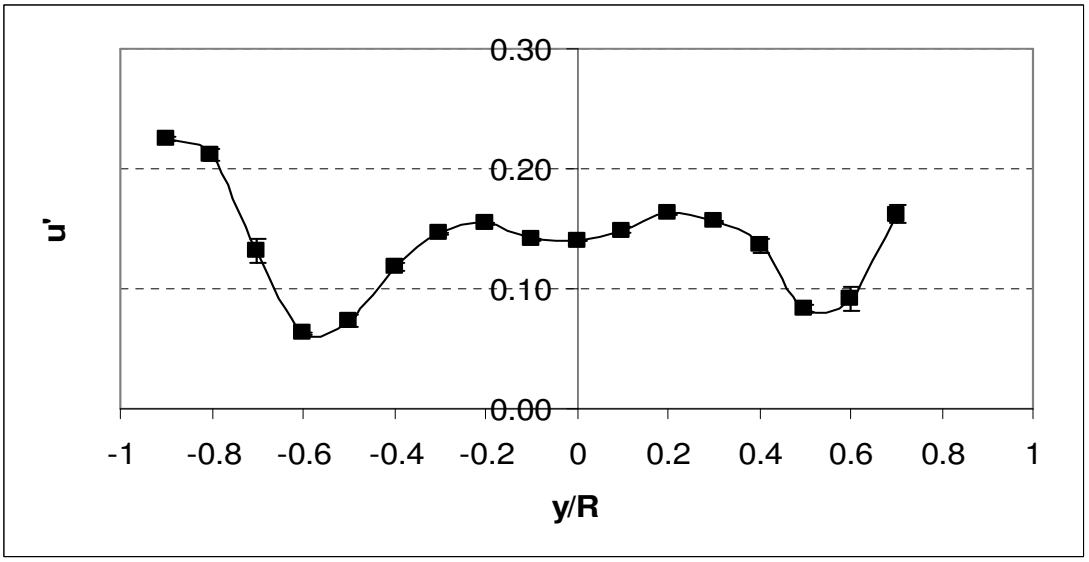

Figure A.10. Axial rms fluctuation velocity profile for Fin IIIr at *x/D* = 4.8. Results are the average of two tests with the same alignment.

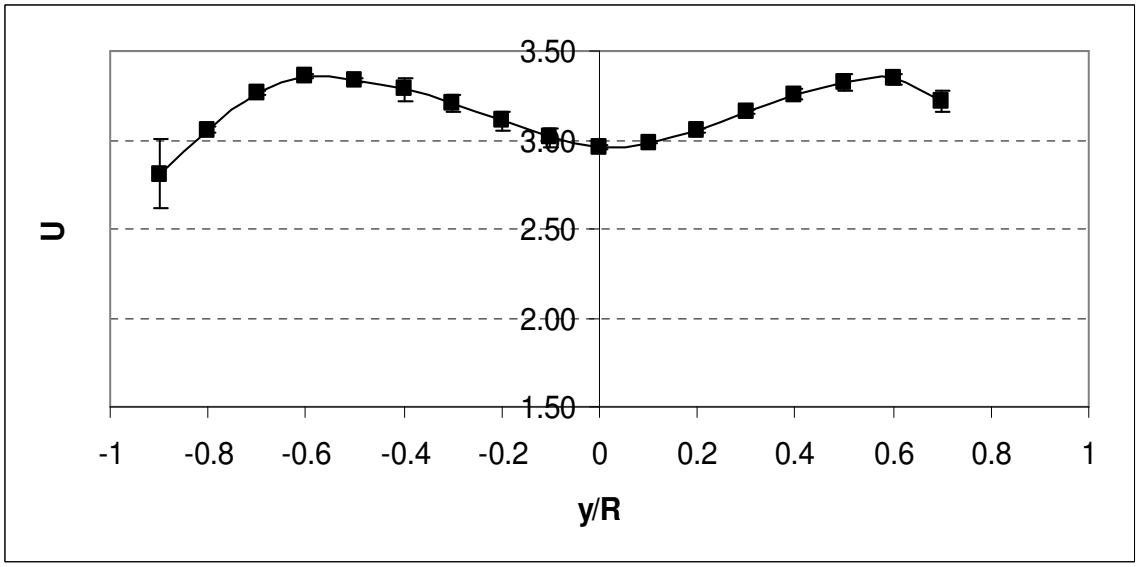

Figure A.11. Axial mean velocity profile for Fin IIIr at *x/D* = 4.8. Results are the average of three fully independent tests.

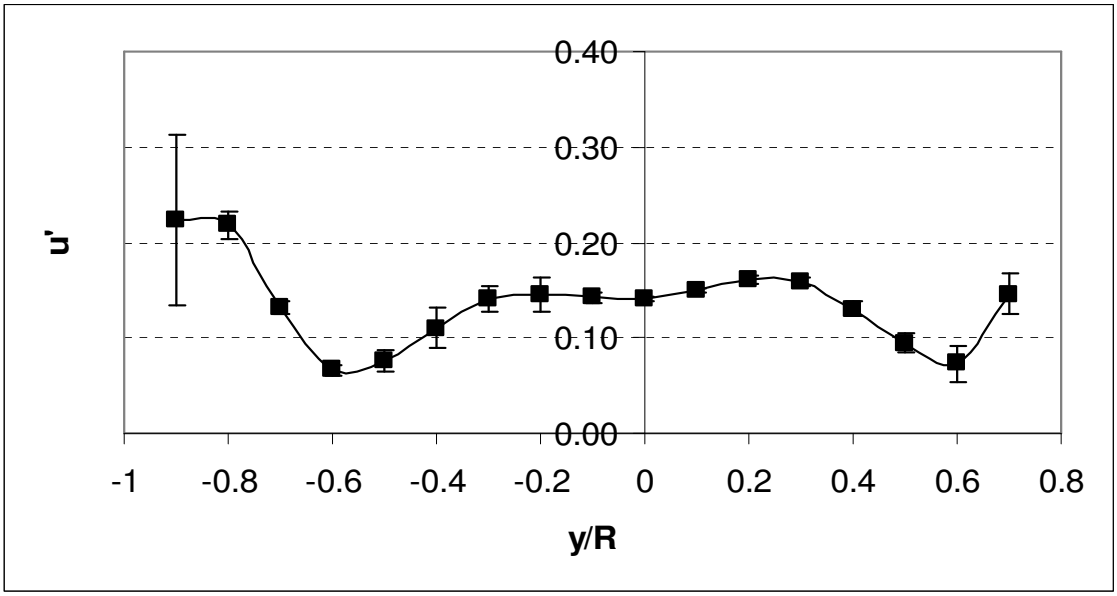

Figure A.12. Axial rms fluctuation velocity profile for Fin IIIr at *x/D* = 4.8. Results are the average of three fully independent tests.

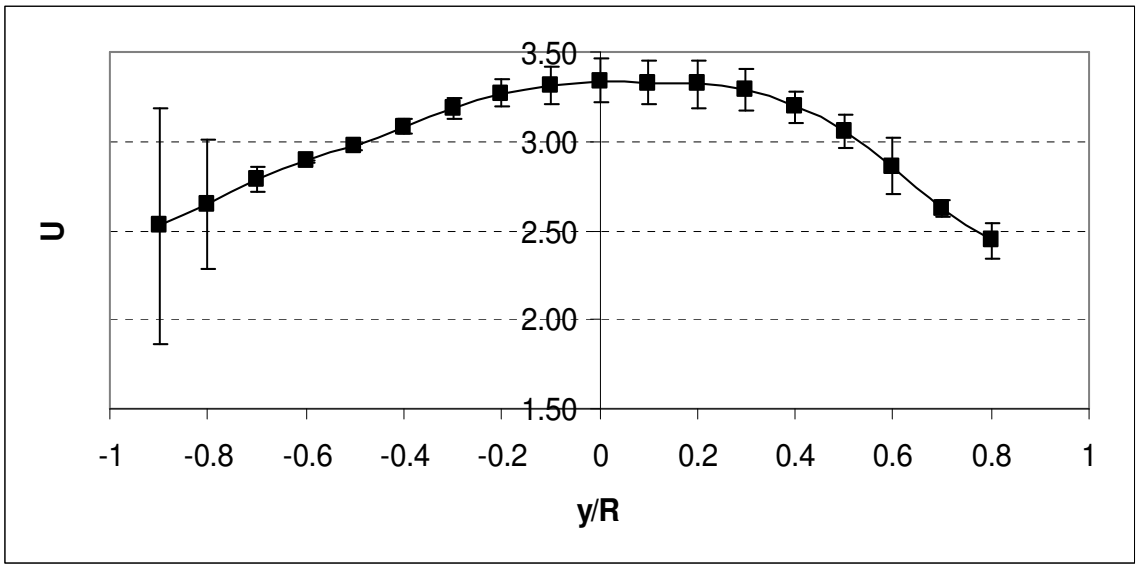

Figure A.13. Axial mean velocity profile for the twisted single fin at *x/D* = 4.8. Results are the average of three fully independent tests.

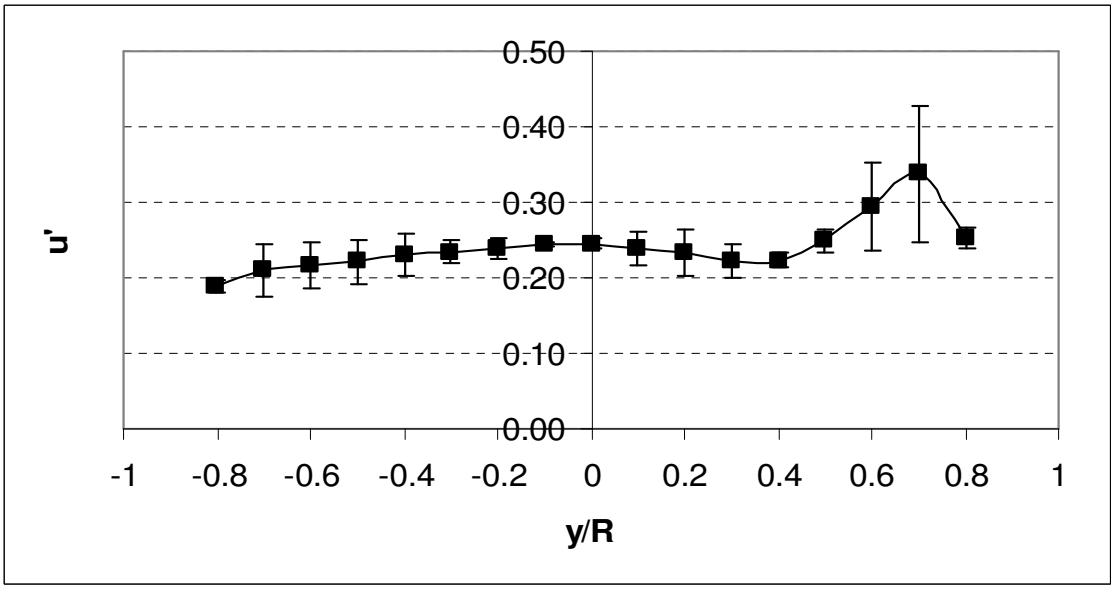

Figure A.14. Axial rms fluctuation velocity profile for the twisted single fin at *x/D* = 4.8. Results are the average of three fully independent tests.

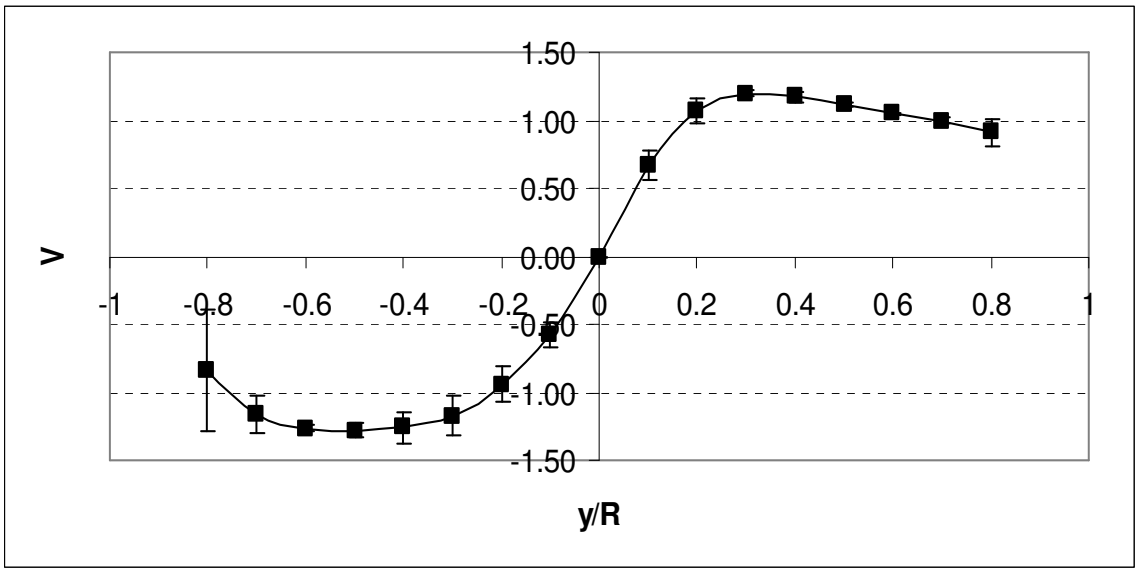

Figure A.15. Azimuthal mean velocity profile for the twisted single fin at *x/D* = 8.8. Results are the average of three fully independent tests.

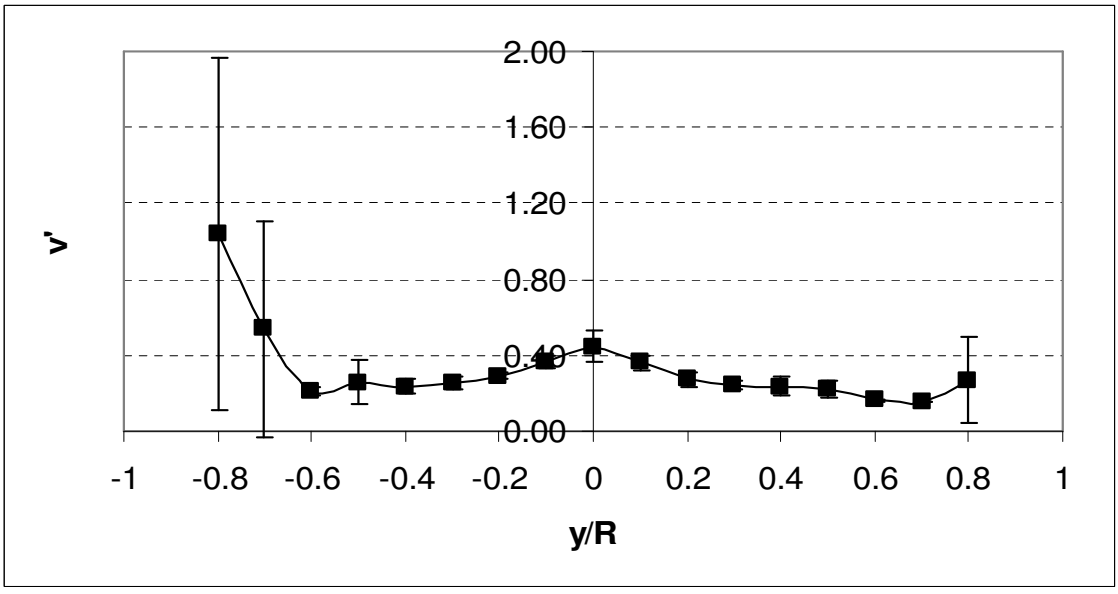

Figure A.16. Azimuthal rms fluctuation velocity profile for the twisted single fin at *x/D* = 8.8. Results are the average of three fully independent tests.